國立交通大學

應用數學系

博士論文

模擬可溶性介面活性劑問題之沉浸邊界法

An immersed boundary method for simulating the interfacial flows with soluble surfactant

研究生：陳冠羽

指導教授：賴明治　教授

中華民國一百零二年十一月

模擬可溶性界面活性劑問題之沉浸邊界法
An immersed boundary method for simulating the interfacial flows with soluble surfactant

研 究 生：陳冠羽
指導教授：賴明治 教授

Student：Kuan-Yu Chen
Advisor：Dr. Ming-Chih Lai

國 立 交 通 大 學
應 用 數 學 系
博 士 論 文

A Thesis
Submitted to Department of Applied Mathematics
College of Science
National Chiao Tung University
in partial Fulfillment of the Requirements
for the Degree of
Doctor of Philosophy
in

Applied Mathematics

November 2013

Hsinchu, Taiwan, Republic of China

中華民國一百零二年十一月

模擬可溶性界面活性劑問題之沉浸邊界法

研究生：陳冠羽　　　　指導教授：賴明治 教授

國立交通大學
應用數學系 博士班

摘要

本論文之第一部分在探討沉浸邊界法中求解壓力項或是指示函數之精度，我們提供一維的理論證明與二維的數值結果來說明 L^1 範數為一階收斂，L^2 範數為半階收斂，而 L^∞ 範數則存在 $O(1)$ 的誤差。我們也將討論帶有其他種類界面奇異項的帕松方程式(Poisson Equation)，求解時的精度預測。

第二部份我們探討兩項流中分子兩端極性不同的界面活性劑，這些分子通常喜好駐於兩種液體的界面上，而且能透過吸收與釋放等過程跟可溶於液體中之界面活性劑交流。這類問題牽涉到在可變形界面上或是複雜區域內求解偏微分方程，因此在界面變動時如何精確計算界面與外在區域耦合之對流擴散方程實為本問題重點所在。我們首先改寫可溶的複雜區域內界面活性劑濃度方程，透過前述指示函數讓該方程鑲嵌於規則空間以方便計算，此外界面與外在區域之間的界面活性劑交流，例如吸收與釋放等過程，則可視為界面的奇異項導入外在區域之濃度方程中。在沉浸邊界法的模型之下，我們發展守衡數值格式求解界面與外在區域耦合之濃度方程，在數值計算下依舊保持界面活性劑之總質量守衡。我們做了一系列的數值測試來驗證我們提出的數值方法的正確性。我們也將過去針對不可溶性界面活性劑的研究工作拓展到可溶性界面活性劑，並且將探討界面活性劑的可溶性對於液體界面的形變造成的影響。

An immersed boundary method for simulating the interfacial flows with soluble surfactant

Student：Kuan-Yu Chen Advisors：Dr. Ming-Chih Lai

Department of Applied Mathematics
National Chiao Tung University

ABSTRACT

In the first part of this thesis, we provide a simplified one-dimensional analysis and two-dimensional numerical experiments to predict that the overall accuracy for the pressure problem or indicator function in immersed boundary calculations is first-order accurate in L^1 norm, half-order accurate in L^2 norm, but has O(1) error in L^∞ norm. We also discuss the accuracy for another type of source terms for solving Poisson problems with singular conditions on the interface.

In the second part, we consider the surfactant, which is an amphiphilic molecular, under multi-phase fluids. These particles usually favor the presence in the fluid interface, and they may couple with the surfactant soluble in one of bulk domains through adsorption and desorption processes. This type of problem needs to solve partial differential equations in deformable interfaces or complex domains. Thus, it is important to accurately solve coupled surface-bulk convection-diffusion equations especially when the interface is moving. We first rewrite the original bulk concentration equation in an irregular domain (soluble region) into a regular computational domain via the usage of the indicator function, which is described in previous part, so that the concentration flux across the interface due to adsorption and desorption processes can be termed as a singular source in the modified equation. Based on the immersed boundary formulation, we then develop a new conservative scheme for solving this coupled surface-bulk concentration equations which the total surfactant mass is conserved in discrete sense. A series of numerical tests has been conducted to validate the present scheme. As an application, we extend our previous work to the soluble case and investigate the effect of solubility on drop deformations.

誌　　謝

本論文得以完成，首先要特別感謝本人的指導教授　賴明治老師在六年多的博士班生涯(以及之前兩年的碩士班學業)之中，不管是在學業上、研究上或是生活上，都不斷給予在下各種幫助與指點。感謝老師多次安排到國外（美國、香港等）參與研討會的機會，讓我能夠接觸到國外最新的研究發展，並且跟國外的學者溝通交流，對研究工作與自身的語言能力都有不小的助益。另外也感謝老師經常帶領（或指派）我與其他師門學生參加國內舉辦之各種不同的研討會，尤其是不少國際性的大型研討會，如東亞區工業與應用數學學會年會(EASIAM)等等，其他像是國家理論科學中心的演講，以及物理、化學、機械、大氣等領域的活動，透過大量與不同學門的學者交流，除了增廣見聞外，也能開拓研究工作在不同領域的應用。另外要感謝口試委員林文偉講座教授、楊肅煜教授、吳金典教授與黃聰明教授的指點，使本論文更臻完善。

在博士班求學生涯中，感謝許多交大應數教授的指導與助理們的幫忙，如林琦焜教授對於偏微分方程理論的指導，讓我對於流體力學的數學有更深的了解；感謝鄧君豪老師在數值方法分析上的指導，讓我在處理兩項流問題得以找到盲點；其他還有葉立明教授、吳金典教授、白啟光教授、許元春教授、吳培元教授等等，在課業與其他方面給我的提點。另外要感謝台大郭鴻基教授與中央(目前已轉往台大)蔡武廷教授對於流體力學在其他領域的介紹與應用給我不同的體驗。由於在研究過程中需要大量運用電腦計算，感謝系上的資訊助理詹宗智先生，幫助我處理電腦設備更新維護與其他軟硬體資源的採買，並且在各類設施操作與軟體使用上給予建議。感謝謝天長博士在研究後期對於理論上的問題給予的協助。

沒有師門學生們互相幫忙，很難度過這漫長的博士生涯，感謝以下同門師兄與師弟妹：曾昱豪、曾孝捷、黃仲尹、謝先皓、蔡修齊、郭乂維、胡偉帆、曾鈺傑、陳建明、張永潔、許哲維、陳昱丞、黃義閔、楊承翰、吳聲華、林詩婷、成澤仕軒、關湘源、張毓倫、郭柏均等等。另外要感謝其他系上的學長姐、同學與學弟妹們，包括吳恭儉、呂明杰、廖康伶、李信儀、郭君逸、黃韋強、方怡中、陳德軒、龔柏任、賴建綸、黃俊銘、蘇偉碩、邱鈺傑等等，感謝他們在課業上與生活上的幫助。其他還有大學認識的同學與朋友們，包括黃致維、李仁喆、劉名謙、胡仲軒、陳華軒、黃晟志、陳奕光、吳明道，還有其他透過網路認識的朋友們（族繁不及備載）。還要感謝從小一起長大的死黨賴運辰，是到處遊山玩水的好伙伴。

最後要特別感謝我的家人，包括我的父親、母親、弟弟、祖母、姑姑與姑丈、大伯父、叔叔、姨媽、舅舅等等，感謝他們始終不斷給我支持與鼓勵，以及無私的付出與關懷，讓我能夠專心在研究工作上持續邁進，不必為了生活瑣事煩心。

目 錄

表目錄

圖目錄

符號說明

Ω ：computational domain

Σ ：interface immersed in Ω

Ω_0 ：inner region enclosed by Σ in Ω

Ω_1 ：outer region of Ω

Δx ：discrete mesh width in x-direction

Δy ：discrete mesh width in y-direction

Δt ：discrete time step size

h ：unit mesh width

α ：surface parameterization

$d\alpha$ ：surface element under parameterization

$\Delta\alpha$ ：discrete surface mesh width

$\mathbf{X}(\alpha)$ ：parameterized position of the interface

$\left|\frac{\partial \mathbf{X}}{\partial \alpha}\right|$ ：stretching factor

τ ：unit tangent vector of interface

$\mathbf{n}$ ：unit outward normal vector of interface

C ：bulk surfactant concentration

Γ ：surface surfactant concentration

p ：pressure

$\mathbf{u}$ ：velocity field

u ：velocity component in x-direction

v ：velocity component in y-direction

$\mathbf{U}$ ：velocity field on the interface

$\mathbf{f}$ ：external force

$\mathbf{F}$ ：interfacial force

$G(x;y)$ ：1D Green function

$I(\mathbf{x})$ ：indicator function which indicates inner region

$H(\mathbf{x})$ ：indicator function which indicates outer region

∇ ：gradient

$\nabla\cdot$ ：divergence

∇^2 ：Laplacian (or Δ)
∇_s ：surface gradient
$\nabla_s \cdot$ ：surface divergence
∇_s^2 ：surface Laplacian (or Δ_s)
$\delta(x)$ ：1D delta function
$\delta^2(\mathbf{x})$ ：2D delta function
$\delta_h(x)$ ：1D discrete delta function
$\delta_h^2(\mathbf{x})$ ：2D discrete delta function
$\delta_h^{\cos}$ ：discrete delta function with cosine type
$\delta_h^{\surd}$ ：discrete delta function with square root type
D_α ：surface first derivative difference operator
D_h ：1D first derivative centered difference operator
D_h^2 ：1D second derivative centered difference operator
∇_h ：2D gradient difference operator
$\nabla_h \cdot$ ：2D divergence difference operator
∇_h^2 ：2D Laplacian difference operator
$\|\ \|_1$ ：(discrete) one norm
$\|\ \|_2$ ：(discrete) two norm
$\|\ \|_\infty$ ：(discrete) infinity norm
μ ：viscosity
Re ：Reynolds' number
Ca ：Capillary number
Cs ：bulk surfactant concentration adjacent to the interface
Pe ：Peclet number
Pe_s ：surface Peclet number
S_a ：absorption Stanton number
S_d ：desorption Stanton number
λ ：dimensionless absorption depth
σ ：surface tension
El ：Elasticity number

Chapter 1

Preliminaries

This thesis is a combination of our previous works. The first part is based on the article [12] ”K.-Y. Chen, K.-A. Feng, Y. Kim, M.-C. Lai, A note on pressure accuracy in immersed boundary method for Stokes flow, Journal of Computational Physics, 230 (2011), 4377–4383.” We provide a simplified one-dimensional analysis and two-dimensional numerical experiments to predict that the overall accuracy for the pressure problem or indicator function in immersed boundary calculations is first-order accurate in L^1 norm, half-order accurate in L^2 norm, but has $O(1)$ error in L^∞ norm. We also discuss the accuracy for another type of source terms for solving Poisson problems with singular conditions on the interface. In this case, we prove that the convergent rate is second-order accurate in L^1 norm, one and half-order accurate in L^2 norm, and first-order accurate in L^∞ norm. Moreover, we will give some applications to solve second-order elliptic equations with piecewise-constant coefficients by indicator function, and compute the velocity in Stokes equations by using the solution of pressure equations we obtained.

The following part provides the details of the paper [13] ”K.-Y. Chen, M.-C. Lai, A conservative scheme for solving coupled surface-bulk convection-diffusion equations with an application to interfacial flows with soluble surfactant, Journal of Computational Physics, 257(2014), 1–18.” We consider the surfactant, which is an amphiphilic molecular, under multi-phase fluids. These particles usually favor the presence in the fluid interface, and they may couple with the surfactant soluble in one of bulk domains through adsorption and desorption processes. This type of problem needs to solve partial differential equations in deformable interfaces or complex domains. Thus, it is important to accurately solve coupled surface-bulk convection-diffusion equations especially when the interface is moving. We first rewrite the original bulk concentration equation in an irregular domain (soluble region) into a regular computational domain via the usage of the indicator function, which is described in previous part, so that the concentration flux across the interface due to adsorption and desorption processes can be termed as a singular source in the modified equation. Based on the immersed boundary formulation, we then develop a new conservative scheme for solving this coupled surface-bulk concentration equations which the total surfactant mass is conserved in discrete sense. A series of numerical tests has been conducted to validate the present scheme. As an application, we extend our previous work [24] ”M.-C. Lai, Y.-H. Tseng and H. Huang, An immersed boundary method for interfacial flows with insoluble surfactant, Journal of Computational Physics, 227 (2008) 7279-7293” to the soluble case. The effects of solubility of surfactant on drop deformations in a quiescent and shear flow are investigated in detail.

Part I

Numerical research on Poisson problems with interfacial source terms

Chapter 2

Introduction 1

In this part, we consider the problems of solving a Poisson equation in the computational domain Ω (either in one-dimension or in two-dimension) with a source term defined only on a boundary (one point for one-dimensional case, and one-dimensional interface for two-dimensional case, respectively) Σ immersed in Ω. This type of the problems arise from using Immersed Boundary Method to solve the stationary Stokes flow defined on irregular domain or containing interfacial singularities inside the regular domain. The Stokes problem in the immersed boundary formulation is defined as

$$-\nabla p + \mu \Delta \mathbf{u} + \int_{\Sigma} \mathbf{F}(s)\, \delta^2(\mathbf{x} - \mathbf{X}(s))\, ds = 0, \tag{1}$$

$$\nabla \cdot \mathbf{u} = 0. \tag{2}$$

The two-dimensional Dirac delta function is defined as

$$\delta^2(\mathbf{x}) = \delta(x)\, \delta(y), \tag{3}$$

which is the combination of two one-dimensional Dirac delta functions. Since the immersed boundary force $\mathbf{F}$ is only exerted along the interface Σ, we use the integral with the Dirac delta function to keep the formulation is defined along the interface Σ. Therefore, the above immersed boundary formulation is a typical singular problem with a delta function source. To solve this problem, a simple ansatz is by taking the divergence operator on Eq. (1), which means that

$$-\Delta p(\mathbf{x}) + \mu \nabla \cdot \Delta \mathbf{u} + \nabla \cdot \int_{\Sigma} \mathbf{F}(s)\, \delta^2(\mathbf{x} - \mathbf{X}(s))\, ds = 0. \tag{4}$$

Use the incompressibility constraint in Eq. (2) to take out $\mathbf{u}$, we obtain the pressure equation

$$\Delta p(\mathbf{x}) = \nabla \cdot \int_{\Sigma} \boldsymbol{F}(s)\, \delta^2(\mathbf{x} - \mathbf{X}(s))\, ds. \tag{5}$$

Notice that, the above equation is what we mention before, which involves solving Poisson equation with a source term which can be written as the derivatives of Dirac delta function. Furthermore, in the general immersed boundary computations, one often uses periodic or Neumann boundary conditions to solve pressure equation. For simplicity, throughout this work, we just use the Dirichlet boundary condition since we are more concerned about the accuracy caused by the derivatives of Dirac delta function near the interface.

After solving the pressure p, we have to solve the velocity field $\boldsymbol{u}$ by solving the equation (1) with substituting p. In this case, we need to solve another two Poisson equations with source terms on the interface, which can be described as Dirac delta function. Therefore, we deal with two kinds of source terms to the Poisson equations introduced by the Stokes flow problem.

Another example comes from two-phase flow problem. In the former work by Tryggvason et. al. [37], they introduced the indicator function in order to track the regions of two-phase flow. For any quantity q, which could be density, viscosity or others, is valued piecewise constant in the domain, i.e. it is discontinuous across the interface. It can be represented by the following:

$$q(\mathbf{x}) = q_{\text{out}} + (q_{\text{in}} - q_{\text{out}}) I(\mathbf{x}), \tag{6}$$

where q_{in} and q_{out} are the constant quantity inside and outside of the interface, respectively. Note that, the indicator function has the value one ($I = 1$) inside the immersed boundary Γ and the value zero ($I = 0$) outside. Assume we use the immersed boundary Σ to divide the domain Ω into two parts: Ω_0, which is inside Σ; and Ω_1, which is outside Σ. The indicator function can be written as

$$I(\boldsymbol{x}, t) = \begin{cases} 1 & \text{if} \quad \boldsymbol{x} \in \Omega_0 \\ 0 & \text{if} \quad \boldsymbol{x} \in \Omega_1 \end{cases} \tag{7}$$

The indicator function can be calculated as the following procedure [37]. Let $\mathbf{n}$ be the unit outward normal to the interface, then the indicator function can be represented by

$$I(\mathbf{x}) = \int_{\Omega_0} \delta^2(\mathbf{x} - \tilde{\mathbf{x}})\, d\tilde{\mathbf{x}}.$$

By taking the gradient and then the divergence operators, we have

$$\nabla I(\mathbf{x}) = -\int_{\Sigma} \mathbf{n}\, \delta^2(\mathbf{x} - \mathbf{X}(s))\, ds,$$

$$\Delta I(\mathbf{x}) = -\nabla \cdot \int_{\Sigma} \mathbf{n}\, \delta^2(\mathbf{x} - \mathbf{X}(s))\, ds. \tag{8}$$

Thus, the indicator function can be obtained by solving a similar equation as Eq. (5) with the special singular forcing term $\mathbf{F}(s) = -\mathbf{n}(s)$.

In the following of this part, our goal is to use the standard finite difference scheme with smoothing discrete delta function to discretize the equations (5) and (8), and to investigate the numerical accuracy. Moreover, we will also discuss other types of singularity on the interface to the Poisson equations, and do further analysis and validations to these problems.

Chapter 3

One-dimensional analysis

In this chapter, we will discuss the accuracy of numerical solution by using simple finite-difference schemes to our problems.

3.1 One-dimensional analysis for source terms as derivatives of delta functions

We consider the one-dimensional equation as

$$\frac{d^2u}{dx^2} = c\frac{d}{dx}\delta(x-\alpha),\ 0 \le x \le 1 \tag{9}$$

with boundary condition

$$u(0) = u(1) = 0, \tag{10}$$

and the interface is located at $x = \alpha \in (0, 1)$. The exact solution of Eq. (9) can be expressed as

$$u(x) = \int_0^1 G(x; y)\ c\frac{d}{dy}\delta(y-\alpha)\ dy \tag{11}$$

where $G(x; y)$ is the well-known Green's function, which solves

$$\frac{d^2G}{dx^2}(x; y) = \delta(x-y). \tag{12}$$

The Green's function $G(x;y)$ can be explicit written as

$$G(x;y)=\begin{cases} x(y-1), & 0\le x\le y, \\ y(x-1), & y<x\le 1 \end{cases}. \tag{13}$$

Without losing the generality, we set $c=1$. By applying the integration by parts into Eq. (11) , we obtain

$$\begin{aligned} u(x) &= \int_0^1 G(x;y)\ c\frac{d}{dy}\delta(y-\alpha)\ dy \\ &= G(x;y)\delta(y-\alpha)|_0^{y=1} - \int_0^1 \frac{d}{dy}G(x;y)\ \delta(y-\alpha)\ dy \\ &= -\int_0^1 \frac{d}{dy}G(x;y)\ \delta(y-\alpha)\ dy. \end{aligned} \tag{14}$$

The Boundary terms vanish by using the definition of Green's function.

Based on uniform grid with grid points $x_j=jh, j=0,1,...,N$ where $h=1/N$, we use the standard centered difference scheme to discretize Eq. (9) with $c=1$ as following

$$\frac{U_{j-1}-2U_j+U_{j+1}}{h^2}=\frac{\delta_h(x_{j+1}-\alpha)-\delta_h(x_{j-1}-\alpha)}{2h}. \tag{15}$$

The discrete delta function in [31] defined as

$$\delta_h(x)^{\cos}=\begin{cases} \frac{1}{4h}(1+\cos(\frac{\pi x}{2h})), & \text{if } |x|\le 2h, \\ 0, & \text{otherwise} \end{cases}. \tag{16}$$

Although there are more different discrete delta functions can be found in [4, 44] and other papers, the usage of different delta functions cannot lead to different conclusions that will be given in this subsection.

The discrete delta functions above satisfies

$$\sum_{m=0}^{N}\delta_h(x_m-\alpha)h=1, \tag{17}$$

which is the corresponding basic requirement for discrete delta function. For simplicity, we denote the first-order and second-order centered difference operators as D_h and D_h^2, respectively. Analog to analytic solution in (11), the discrete solution U_j of Eq. (15) can also be written as

$$U_j=h\sum_{m=0}^{N}G_{jm}D_h\delta_h(x_m-\alpha) \tag{18}$$

where $G_{jm} = G(x_j; x_m)$ is the discrete version of Green's function defined as

$$G_{jm} = \begin{cases} x_j(x_m - 1), & 0 \le j \le m, \\ x_m(x_j - 1), & m < j \le N \end{cases} . \tag{19}$$

We can immediately check that G satisfies $D_h^2 G_{jm} = \frac{1}{h}\delta_{jm}$ where δ_{jm} is the Kronecker delta function.

Now, by taking summation by parts and the property of discrete delta function, we can rewrite the numerical solution U_j as

$$\begin{aligned} U_j &= h\sum_{m=0}^{N} G_{jm} D_h \delta_h(x_m - \alpha) \\ &= h\sum_{m=1}^{N-1} G_{jm} \frac{\delta_h(x_{m+1} - \alpha) - \delta_h(x_{m-1} - \alpha)}{2h} \\ &= h\sum_{m=2}^{N} G_{j(m-1)} \frac{\delta_h(x_m - \alpha)}{2h} - h\sum_{m=0}^{N-2} G_{j(m+1)} \frac{\delta_h(x_m - \alpha)}{2h} \\ &= -h\sum_{m=1}^{N-1} \frac{G_{j(m+1)} - G_{j(m-1)}}{2h} \delta_h(x_m - \alpha) \\ &= -h\sum_{m=0}^{N} D_h G_{jm} \delta_h(x_m - \alpha) \end{aligned} \tag{20}$$

Hence the point-wise error between U_j and $u(x_j)$ can be expressed as

$$\begin{aligned} |U_j - u(x_j)| &= \left| h\sum_{m=0}^{N} D_h G_{jm} \delta_h(x_m - \alpha) - \int_0^1 \frac{d}{dy} G(x_j; y)\ \delta(y - \alpha)\ dy \right| \\ &\le \left| h\sum_{m=0}^{N} D_h G_{jm} \delta_h(x_m - \alpha) - h\sum_{m=0}^{N} \frac{d}{dy} G(x_j; y)\Big|_{y=x_m} \delta_h(x_m - \alpha) \right| \\ &+ \left| h\sum_{m=0}^{N} \frac{d}{dy} G(x_j; y)\Big|_{y=x_m} \delta_h(x_m - \alpha) - \frac{d}{dy} G(x_j; y)\Big|_{y=\alpha} \right| \\ &= E_1 + E_2 \end{aligned}$$

First, E_1 is the error from discretizing the differentiation of Green's function. Using the fact that the derivative of Greens function is

$$\frac{d}{dy} G(x_j; y)\Big|_{y=x_m} = \begin{cases} x_j, & 0 \le x_j \le x_m \\ x_j - 1, & x_m < x_j \le 1 \end{cases} \tag{21}$$

and that its discrete counterpart is

$$D_h G_{jm} = \begin{cases} x_j, & j < m \\ x_j - \frac{1}{2}, & j = m \\ x_j - 1, & j > m \end{cases}, \tag{22}$$

we obtain

$$D_h G_{jm} - \frac{d}{dy} G(x_j; y)\Big|_{y=x_m} = \begin{cases} \frac{1}{2}, & \text{if } m = j \\ 0, & \text{otherwise} \end{cases} \tag{23}$$

By using (23), we compute

$$\begin{aligned} E_1 &= \left| h \sum_{m=0}^{N} D_h G_{jm} \delta_h(x_m - \alpha) - h \sum_{m=0}^{N} \frac{d}{dy} G(x_j; y)\Big|_{y=x_m} \delta_h(x_m - \alpha) \right| \\ &= \left| h \sum_{m=0}^{N} \left(D_h G_{jm} - \frac{d}{dy} G(x_j; y)\Big|_{y=x_m} \right) \delta_h(x_m - \alpha) \right| \\ &= \left| h \frac{1}{2} \delta_h(x_j - \alpha) \right| \\ &= \begin{cases} O(1), & \text{when } |x_j - \alpha| \le 2h \\ 0, & \text{otherwise} \end{cases} \end{aligned} \tag{24}$$

The second part of the error E_2 is simply an interpolating error for the function $\frac{d}{dy} G(x_j; y)\Big|_{y=x_m}$. Using the formula in Eq. (21) and the first moment condition in (17), since the discrete delta function has finite support $4h$, we can obtain

$$\begin{aligned} E_2 &= \left| h \sum_{m=0}^{N} \frac{d}{dy} G(x_j; y)\Big|_{y=x_m} \delta_h(x_m - \alpha) - \frac{d}{dy} G(x_j; y)\Big|_{y=\alpha} \right| \\ &= \left| h \sum_{m=0}^{j-1} \frac{d}{dy} G(x_j; y)\Big|_{y=x_m} \delta_h(x_m - \alpha) \right. \\ &+ \left. h \sum_{m=j}^{N} \frac{d}{dy} G(x_j; y)\Big|_{y=x_m} \delta_h(x_m - \alpha) - \frac{d}{dy} G(x_j; y)\Big|_{y=\alpha} \right| \\ &= \left| h \sum_{m=0}^{j-1} (x_j - 1) \delta_h(x_m - \alpha) + h \sum_{m=j}^{N} x_j \delta_h(x_m - \alpha) - \frac{d}{dy} G(x_j; y)\Big|_{y=\alpha} \right| \end{aligned}$$

For $x_j \le \alpha$, $\frac{d}{dy}G(x_j;y)\Big|_{y=\alpha} = x_j$, then

$$\begin{aligned}
E_2 &= \left| h\sum_{m=0}^{j-1}(x_j-1)\delta_h(x_m-\alpha) + h\sum_{m=j}^{N} x_j\delta_h(x_m-\alpha) - x_j \right| \\
&= \left| h\sum_{m=0}^{j-1}\delta_h(x_m-\alpha) \right| \\
&= \begin{cases} O(1), & \text{as } \alpha - x_j \le 2h \\ 0, & \text{otherwise} \end{cases}
\end{aligned} \tag{25}$$

Similarly, for $x_j > \alpha$, $\frac{d}{dy}G(x_j;y)\Big|_{y=\alpha} = x_j - 1$, then

$$\begin{aligned}
E_2 &= \left| h\sum_{m=0}^{j-1}(x_j-1)\delta_h(x_m-\alpha) + h\sum_{m=j}^{N} x_j\delta_h(x_m-\alpha) - (x_j-1) \right| \\
&= \left| h\sum_{m=j}^{N}\delta_h(x_m-\alpha) \right| \\
&= \begin{cases} O(1), & \text{as } x_j - \alpha \le 2h \\ 0, & \text{otherwise} \end{cases}
\end{aligned} \tag{26}$$

Therefore, we combine (25) and (26) to get

$$E_2 = \begin{cases} O(1), & \text{as } |x_j - \alpha| \le 2h \\ 0, & \text{otherwise} \end{cases} \tag{27}$$

From the above analysis, one can immediately see that the point-wise error appears only at some points around the singular point α, which means that the maximum error $\|u_h - u\|_\infty$ is of order $O(1)$. For the same reason, we can conclude that $L_1(\|u_h - u\|_1)$ and $L_2(\|u_h - u\|_2)$ errors are of order $O(h)$ and $O(h^{1/2})$, respectively. Our numerical results in final section will confirm this conclusion.

3.2 One-dimensional analysis for source terms as delta functions

We consider the one-dimensional equation as

$$\frac{d^2u}{dx^2} = c\delta(x-\alpha),\ 0 \le x \le 1 \tag{28}$$

with the same boundary condition as Eq. (10), and the interface is located at $x = \alpha \in (0, 1)$. The exact solution of (28) can be expressed as

$$u(x) = \int_0^1 G(x; y)\ c\delta(y - \alpha)\ dy \tag{29}$$

we use the standard centered difference scheme to discretize Eq. (28) with $c = 1$ as following

$$\frac{U_{j-1} - 2U_j + U_{j+1}}{h^2} = \delta_h(x_j - \alpha), \tag{30}$$

Analog to analytic solution in Eq. (29), the discrete solution U_j of Eq. (30) can also be written as

$$U_j = h \sum_{m=0}^{N} G_{jm} \delta_h(x_m - \alpha) \tag{31}$$

Hence the point-wise error between U_j and $u(x_j)$ can be expressed as

$$|U_j - u(x_j)| = \left| h \sum_{m=0}^{N} G_{jm} \delta_h(x_m - \alpha) - \int_0^1 G(x; y) \delta(y - \alpha)\ dy \right| \tag{32}$$

According to [38], [44] and [4], we consider two different discrete delta functions

$$\delta_h^{\cos} = \begin{cases} \frac{1}{4h}(1 + \cos(\frac{\pi x}{2h})), & \text{if } |x| \le 2h, \\ 0, & \text{otherwise} \end{cases}; \tag{33}$$

$$\delta_h^{\sqrt{\ }} = \begin{cases} \frac{1}{8}\left(3 - 2\left|\frac{x}{h}\right| + \sqrt{1 + 4\left|\frac{x}{h}\right| - 4\left|\frac{x}{h}\right|^2}\right) & \text{if } |x| \le h, \\ \frac{1}{8}\left(5 - 2\left|\frac{x}{h}\right| - \sqrt{-7 + 12\left|\frac{x}{h}\right| - 4\left|\frac{x}{h}\right|^2}\right) & \text{if } h < |x| \le 2h, \\ 0, & \text{otherwise} \end{cases}. \tag{34}$$

with the relative moment conditions

$$h \sum_{m=0}^{N} (x_m - \alpha) \delta_h^{\cos}(x_m - \alpha) = O(h) \tag{35}$$

$$h \sum_{m=0}^{N} (x_m - \alpha) \delta_h^{\sqrt{\ }}(x_m - \alpha) = 0 \tag{36}$$

Suppose α lies in some interval (x_i, x_{i+1}). For $x_j < \alpha - h$, we have

$$\begin{aligned}
|U_j - u(x_j)| &= \left| h \sum_{m=i-1}^{i+2} G_{jm}\delta_h(x_m - \alpha) - x_j(\alpha - 1) \right| \\
&= \left| h \sum_{m=i-1}^{i+2} x_j(x_m - 1)\delta_h(x_m - \alpha) - x_j(\alpha - 1) \right| \\
&= \left| h \sum_{m=i-1}^{i+2} x_j(x_m - \alpha + \alpha - 1)\delta_h(x_m - \alpha) - x_j(\alpha - 1) \right| \\
&= \left| h \sum_{m=i-1}^{i+2} x_j(x_m - \alpha)\delta_h(x_m - \alpha) \right| \\
&= \begin{cases} O(h), & \text{for } \delta_h^{\cos} \\ 0, & \text{for } \delta_h^{\sqrt{\ }} \end{cases} \qquad (37)
\end{aligned}$$

For $\alpha - h \le x_j \le \alpha$, we compute

$$\begin{aligned}
|U_j - u(x_j)| &= \left| h \sum_{m=i-1}^{i+2} G_{jm}\delta_h(x_m - \alpha) - x_j(\alpha - 1) \right| \\
&= \left| h \left(x_{i-1}(x_j - 1)\delta_h(x_{i-1} - \alpha) + \sum_{m=i}^{i+2} x_j(x_m - 1)\delta_h(x_m - \alpha) \right) - x_j(\alpha - 1) \right| \\
&= \Bigg| h \Bigg[\left(x_j(x_{i-1} - \alpha + \alpha - 1) + h \right) \delta_h(x_{i-1} - \alpha) \\
&+ \sum_{m=i}^{i+2} x_j(x_m - \alpha + \alpha - 1)\delta_h(x_m - \alpha) \Bigg] - x_j(\alpha - 1) \Bigg| \\
&= \left| h^2 \delta_h(x_{i-1} - \alpha) + h \sum_{m=i-1}^{i+2} x_j(x_m - \alpha)\delta_h(x_m - \alpha) \right| \\
&= O(h). \qquad (38)
\end{aligned}$$

For $\alpha = x_j$, we derive

$$\begin{aligned}
|U_j - u(x_j)| &= \left| h \sum_{m=j-1}^{j+1} G_{jm}\delta_h(x_m - \alpha) - x_j(x_j - 1) \right| \\
&= \left| \frac{x_{j-1}(x_j - 1)}{4} + \frac{x_j(x_j - 1)}{2} + \frac{x_j(x_{j+1} - 1)}{4} - x_j(x_j - 1) \right| \\
&= h \qquad (39)
\end{aligned}$$

For $\alpha < x_j \le \alpha + h$, we calculate

$$\begin{aligned}
|U_j - u(x_j)| &= \left| h \sum_{m=i-1}^{i+2} G_{jm}\delta_h(x_m - \alpha) - \alpha(x_j - 1) \right| \\
&= \left| h \left(x_j(x_{i+2} - 1)\delta_h(x_{i+2} - \alpha) + \sum_{m=i-1}^{i+1} x_m(x_j - 1)\delta_h(x_m - \alpha) \right) - \alpha(x_j - 1) \right| \\
&= \left| h \left[\left((x_{i+2} - \alpha + \alpha)(x_j - 1) + h \right) \delta_h(x_{i+2} - \alpha) \right. \right. \\
&+ \left. \left. \sum_{m=i}^{i+2} (x_m - \alpha + \alpha)(x_j - 1)\delta_h(x_m - \alpha) \right] - \alpha(x_j - 1) \right| \\
&= \left| h^2 \delta_h(x_{i+2} - \alpha) + h \sum_{m=i-1}^{i+2} (x_j - 1)(x_m - \alpha)\delta_h(x_m - \alpha) \right| \\
&= O(h). \qquad (40)
\end{aligned}$$

For $x_j > \alpha + h$, we obtain

$$\begin{aligned}
|U_j - u(x_j)| &= \left| h \sum_{m=i-1}^{i+2} G_{jm}\delta_h(x_m - \alpha) - \alpha(x_j - 1) \right| \\
&= \left| h \sum_{m=i-1}^{i+2} x_m(x_j - 1)\delta_h(x_m - \alpha) - \alpha(x_j - 1) \right| \\
&= \left| h \sum_{m=i-1}^{i+2} (x_m - \alpha + \alpha)(x_j - 1)\delta_h(x_m - \alpha) - \alpha(x_j - 1) \right| \\
&= \left| h \sum_{m=i-1}^{i+2} (x_j - 1)(x_m - \alpha)\delta_h(x_m - \alpha) \right| \\
&= \begin{cases} O(h), & \text{for } \delta_h^{\cos} \\ 0, & \text{for } \delta_h^{\surd} \end{cases} \qquad (41)
\end{aligned}$$

Hence we combine Eq. (37) to Eq. (41) to get

$$\text{for } \delta_h^{\cos},\ |U_j - u(x_j)| = O(h)\ \forall j \qquad (42)$$

$$\text{for } \delta_h^{\surd},\ |U_j - u(x_j)| = \begin{cases} O(h), & \text{as } |x_j - \alpha| \le h \\ 0, & \text{otherwise} \end{cases} \qquad (43)$$

From the above analysis, one can immediately see that, under proper moment conditions satisfied, the point-wise error appears only at some points around the singular point α, which means that the maximum error $\|u_h - u\|_\infty$ is of order $O(h)$. For the same reason, we can conclude that $L_1(\|u_h - u\|_1)$ and $L_2(\|u_h - u\|_2)$ errors are of order $O(h^2)$ and $O(h^{3/2})$, respectively. Our numerical results in final section will confirm this conclusion.

Chapter 4

Numerical results 1

Throughout this chapter, we validate our derivations of convergence analysis via a series of examples. For different kinds of source term, we check one-dimensional cases at first. We also test on two-dimensional examples to see if our analysis is hold numerically.

4.1 Convergent test for source terms as derivatives of delta functions

In this section, we will show the convergent results of solving Poisson problems with source terms as derivatives of delta functions. Since the proof we derived is valid for any kinds of discrete delta functions, we pick up $\delta_h^{\cos}$ and $\delta_h^{\sqrt{}}$ from [4, 44] for comparison. The ratio in all tables of this section means the convergent orders of accuracy, which is computed by

$$\log\left(\frac{\|u-u_N\|}{\|u-u_{2N}\|}\right)/\log\left(\frac{1/N}{1/2N}\right), \tag{44}$$

where u is the exact solution, u_N is the numerical solution with mesh size N.

4.1.1 One-dimensional problem 1

In this subsection, we consider the following one-dimensional problem to verify the proof in section 3.1. The equation is

$$\frac{d^2u}{dx^2} = c\,\frac{d}{dx}\delta(x-\alpha) + g, \qquad 0 < x < 1. \tag{45}$$

Here, the interface is set at the point $\alpha = \pi/6$. The exact solution is given as

$$u(x) = \begin{cases} x^3 + 2\alpha x^2 & \text{if } x \le \alpha \\ \frac{7}{3}(x^3 - 1) & \text{if } x > \alpha \end{cases} \tag{46}$$

where the jump of solution u at the interface c is equal to $-(2\alpha^3 + 7)/3$. The regular source term g can be computed by the analytic solution, which is written as

$$g(x) = \begin{cases} 6x + 4\alpha & \text{if } x \le \alpha \\ 14x & \text{if } x > \alpha \end{cases}. \tag{47}$$

Table 4.1 shows the order of accuracy for our test with using $\delta_h^{\cos}$ which confirms our one-dimensional analysis in previous section. In Table 4.2 we use $\delta_h^{\surd}$ to verify the conclusion we mention. We could observe the same behavior of the errors even if we change the discrete delta function. Figure 4.1 shows the maximum error always occurs across the interface. Even if we refine the mesh, there still exists an $O(1)$ error, which matches our derivations of proof in previous section.

mesh	$\|u-U_h\|_\infty$	ratio	$\|u-U_h\|_2$	ratio	$\|u-U_h\|_1$	ratio
32	8.8827E-01	–	1.7057E-01	–	4.2479E-02	–
64	6.1709E-01	0.5255	1.0736E-01	0.6678	1.9004E-02	1.1604
128	1.1847E-00	-.9409	1.0708E-01	0.0038	1.2980E-02	0.5500
256	1.1579E-00	0.0329	7.4120E-02	0.5307	6.3791E-03	1.0248
512	1.1030E-00	0.0700	5.0171E-02	0.5630	3.0741E-03	1.0531

Table 4.1: Order of accuracy for one-dimensional test with $\delta_h^{\cos}$.

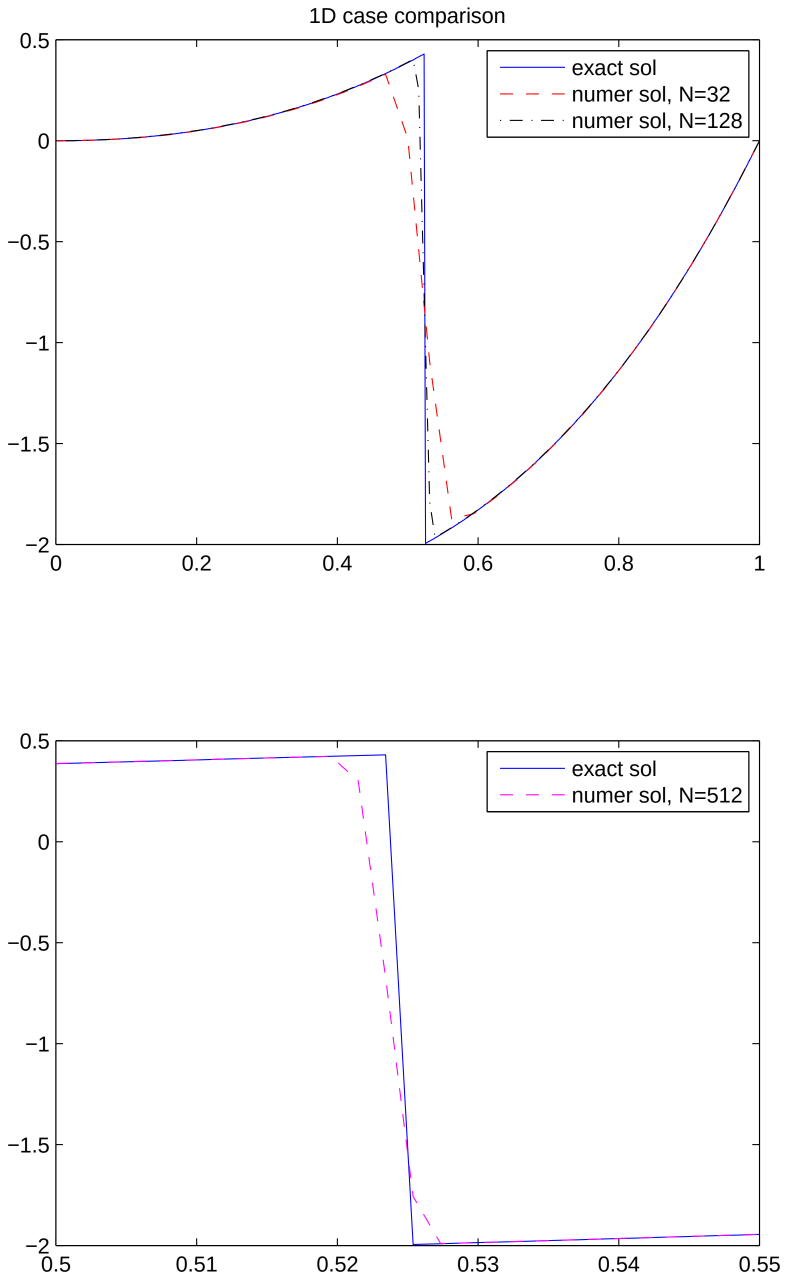

Figure 4.1: Comparison between numerical and analytic solutions for 1D case

mesh	$\|u - U_h\|_\infty$	ratio	$\|u - U_h\|_2$	ratio	$\|u - U_h\|_1$	ratio
32	9.1311E-01	–	1.7356E-01	–	4.2955E-02	–
64	6.1970E-01	0.5592	1.0738E-01	0.6927	1.9005E-02	1.1764
128	1.1875E-00	-.9382	1.0731E-01	0.0008	1.3001E-02	0.5477
256	1.1634E-00	0.0295	7.4446E-02	0.5275	6.3993E-03	1.0226
512	1.1138E-00	0.0628	5.0603E-02	0.5569	3.0926E-03	1.0490

Table 4.2: Order of accuracy for one-dimensional test with $\delta_h^{\surd}$.

4.1.2 Two-dimensional problems 1

For two-dimensional problem, we generally write the equation in the form :

$$\Delta u = \nabla \cdot \int_\Sigma \boldsymbol{F}(s)\, \delta^2(x - \mathbf{X}(s))\, ds + g \tag{48}$$

in a rectangular domain $\Omega = [a, b] \times [c, d]$ with given Dirichlet boundary conditions. We use an $M \times N$ uniform grid with mesh width $\Delta x = \Delta y = h$ to divide the domain Ω. The notation $U_{i,j}$ represents the discrete solution at (x_i, y_j), where $x_i = ih, h = 0, ..., M$ and $y_j = jh, j = 0, ..., N$. We also use a group of marker points $\boldsymbol{X}(s_k) = (X_k, Y_k)$ along the interface Σ with the mesh points $s_k = k\Delta s$. In this case, the mesh width Δs is about a half of h. Then we use regular centered difference scheme to discrete Eq. (48) as

$$\begin{aligned} & \frac{U_{i+1,j} - 2U_{i,j} + U_{i-1,j}}{h^2} + \frac{U_{i,j+1} - 2U_{i,j} + U_{i,j-1}}{h^2} \\ = & \frac{F_{i+1/2,j} - F_{i-1/2,j}}{h} + \frac{F_{i,j+1/2} - F_{i,j-1/2}}{h} + g_{i,j} \end{aligned} \tag{49}$$

where

$$F_{i+1/2,j} = \sum_k F(s_k)\, \delta_h(x_i + h/2 - X(s_k))\delta_h(y_j - Y(s_k))\, \Delta s, \tag{50}$$

$$F_{i-1/2,j} = \sum_k F(s_k)\, \delta_h(x_i - h/2 - X(s_k))\delta_h(y_j - Y(s_k))\, \Delta s, \tag{51}$$

$$F_{i,j+1/2} = \sum_k F(s_k)\, \delta_h(x_i - X(s_k))\delta_h(y_j + 1/2 - Y(s_k))\, \Delta s, \tag{52}$$

and

$$F_{i,j-1/2} = \sum_k F(s_k)\, \delta_h(x_i - X(s_k))\delta_h(y_j - 1/2 - Y(s_k))\, \Delta s. \tag{53}$$

The resultant matrix equation can be solved efficiently by the fast direct solver in Fishpack [3].

Example 4.1.2.1: In the first example, we test the accuracy of the indicator function which is described in Eq. (8). For completeness, we test three different interface Σ in the domain $[-1,1]\times[-1,1]$ as follows.

1. Σ is a circle with the radius 0.3, which is centered at $(0,0)$.
2. Σ is an ellipse with the major radius 0.9 and minor radius 0.1, which is centered at $(0,0)$.
3. Σ is a simple closed curve written in polar coordinates : $r = 0.5 + 0.25\cos(5\theta)$.

Table 4.3-4.5 show the convergence tests for those three different cases with using $\delta_h^{\cos}$, while Table 4.6-4.8 are the correspondent results with using $\delta_h^{\sqrt{\ }}$. The convergent results of the indicator function calculation are strongly supporting our conclusion, which shows first-order convergence in L_1 norm and half-order convergence in L_2 norm, although there is an $O(1)$ error in maximum norm. The results are consistent with one-dimensional analysis. Figure 4.5 shows the cross section of the numerical and analytic solutions along the line $y = 0$. It implies that there exists an $O(1)$ error at the transition area of the indicator function.

$M\times N$	$\|I-I_h\|_\infty$	ratio	$\|I-I_h\|_2$	ratio	$\|I-I_h\|_1$	ratio
32×32	3.6463E-01	–	1.3162E-01	–	6.3848E-02	–
64×64	4.5555E-01	-.3212	9.5529E-02	0.4622	3.2182E-02	0.9883
128×128	4.8736E-01	-.0974	7.2764E-02	0.3926	1.6837E-02	0.9345
256×256	4.8610E-01	0.0037	4.9738E-02	0.5488	8.2361E-03	1.0316
512×512	4.9805E-01	-.0620	3.4744E-02	0.5175	4.0955E-03	1.0078

Table 4.3: Convergent test using $\delta_h^{\cos}$ for indicator function case 1 : a circle.

$M \times N$	$\|I - I_h\|_\infty$	ratio	$\|I - I_h\|_2$	ratio	$\|I - I_h\|_1$	ratio
32×32	6.7302E-01	–	1.9248E-01	–	1.2276E-01	–
64×64	5.0021E-01	0.4280	1.4391E-01	0.4194	6.5139E-02	0.9141
128×128	4.9922E-01	0.0027	9.7919E-02	0.5555	3.1954E-02	1.0275
256×256	4.9834E-01	0.0024	6.8903E-02	0.5070	1.5951E-02	1.0023
512×512	4.9617E-01	0.0061	4.8685E-02	0.5010	7.9510E-03	1.0043

Table 4.4: Convergent test using $\delta_h^{\cos}$ for indicator function case 2 : an ellipse.

$M \times N$	$\|I - I_h\|_\infty$	ratio	$\|I - I_h\|_2$	ratio	$\|I - I_h\|_1$	ratio
32×32	5.9986E-01	–	2.5162E-01	–	2.0860E-01	–
64×64	5.5492E-01	0.1123	1.8259E-01	0.4625	1.0827E-01	0.9460
128×128	5.3029E-01	0.0654	1.2910E-01	0.5000	5.4431E-02	0.9211
256×256	5.1669E-01	0.0374	9.0547E-02	0.5116	2.7064E-02	1.0079
512×512	5.1194E-01	0.0132	6.4251E-02	0.4948	1.3547E-02	0.9983

Table 4.5: Convergent test using $\delta_h^{\cos}$ for indicator function case 3 : a simple closed curve.

$M \times N$	$\|I - I_h\|_\infty$	ratio	$\|I - I_h\|_2$	ratio	$\|I - I_h\|_1$	ratio
32×32	3.6989E-01	–	1.3208E-01	–	6.3755E-02	–
64×64	4.5684E-01	-.3047	9.5640E-02	0.4657	3.2222E-02	0.9844
128×128	4.8714E-01	-.0926	7.2906E-02	0.3915	1.6858E-02	0.9346
256×256	4.8617E-01	0.0028	4.9854E-02	0.5483	8.2307E-03	1.0342
512×512	4.9809E-01	-.0350	3.4826E-02	0.5175	4.0799E-03	1.0124

Table 4.6: Convergent test using $\delta_h^{\surd}$ for indicator function case 1 : a circle.

Example 4.1.2.2: In this example, we solve a pressure equation from Stokes flow problem in [14]. Since the analytic solutions to this problem are available, Lai et el. [23] had use a simplified version of this example to test immersed interface method. The pressure equation to be solved is described in Eq. (5). The computational domain is

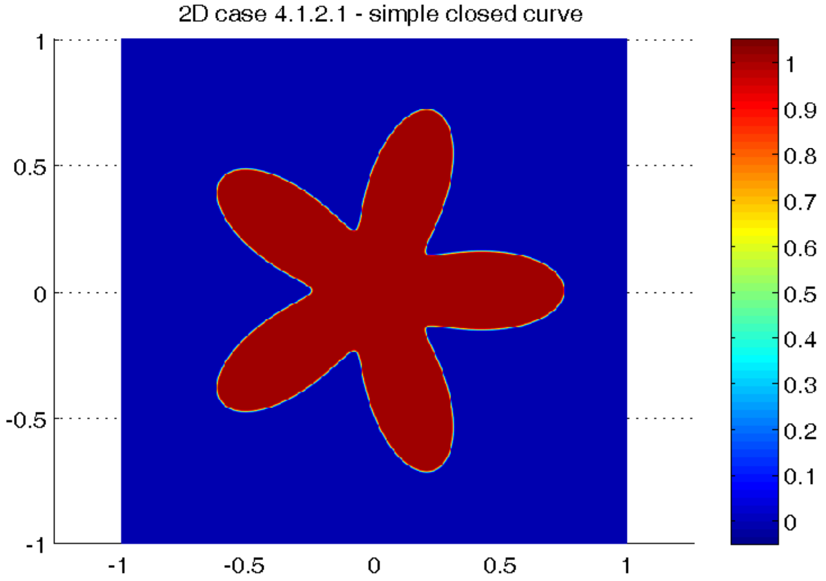

Figure 4.2: Numerical solution for indicator function case 3 : a simple closed curve.

$M \times N$	$\|I - I_h\|_\infty$	ratio	$\|I - I_h\|_2$	ratio	$\|I - I_h\|_1$	ratio
32×32	6.7492E-01	–	1.9304E-01	–	1.2199E-01	–
64×64	5.0036E-01	0.4316	1.4485E-01	0.4142	6.4800E-02	0.9126
128×128	4.9957E-01	0.0021	9.8565E-02	0.5554	3.1684E-02	1.0322
256×256	4.9850E-01	0.0030	6.9379E-02	0.5065	1.5807E-02	1.0031
512×512	4.9660E-01	0.0054	4.8969E-02	0.5025	7.8913E-03	1.0022

Table 4.7: Convergent test using $\delta_h^{\surd}$ for indicator function case 2 : an ellipse.

$\Omega = [-2,2] \times [-2,2]$, and the interface is a unit circle centered at $(0,0)$, i.e. $\mathbf{X}(\theta) = (\cos\theta, \sin\theta)$. The exact solution is written in polar coordinates as

$$p(r,\theta) = \begin{cases} -r^3 \sin(3\theta) & \text{if } r \leq 1 \\ r^{-3} \sin(3\theta) & \text{if } r > 1 \end{cases} \tag{54}$$

and the boundary force $\boldsymbol{F}(\theta) = 2\sin(3\theta)\,\boldsymbol{X}(\theta)$.

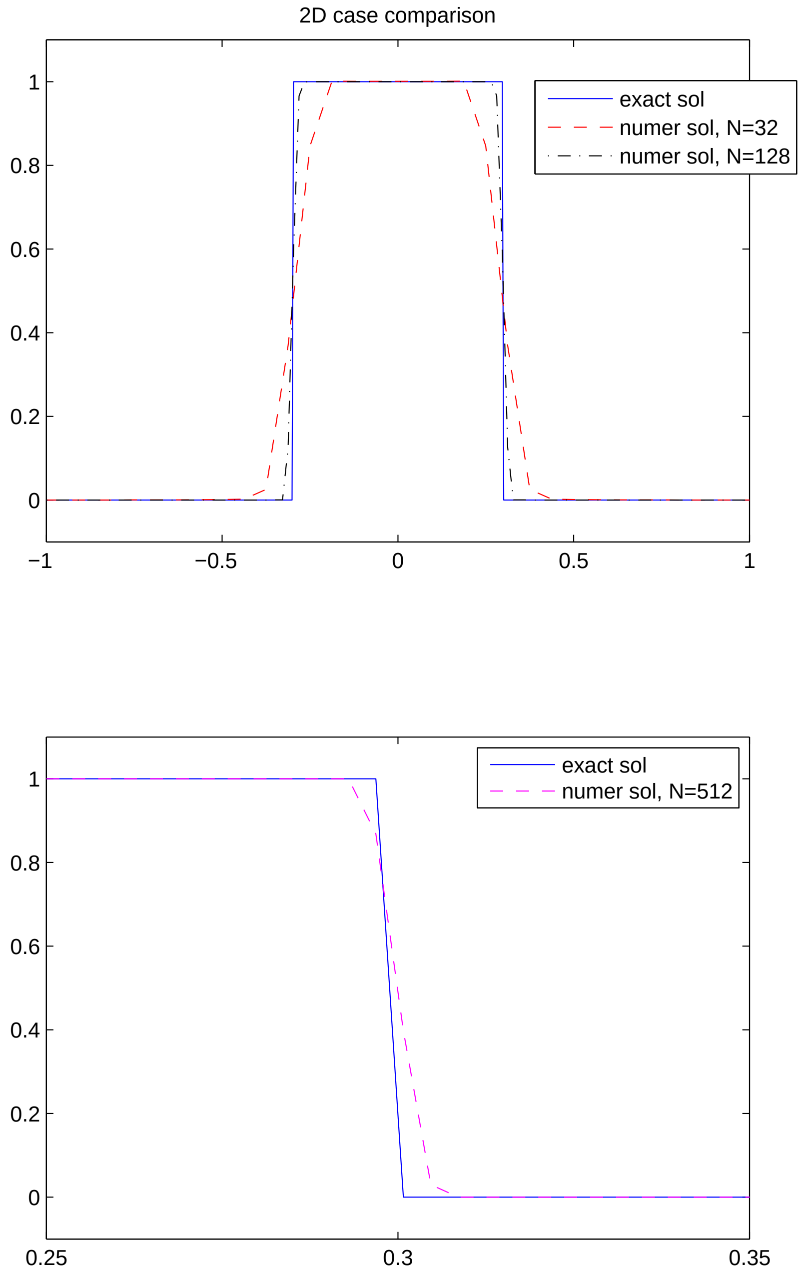

Figure 4.3: Comparison between numerical and analytic solutions for indicator function case 1 : a circle.

$M \times N$	$\|I - I_h\|_\infty$	ratio	$\|I - I_h\|_2$	ratio	$\|I - I_h\|_1$	ratio
32×32	5.9802E-01	–	2.5211E-01	–	2.0901E-01	–
64×64	5.5251E-01	0.1141	1.8301E-01	0.4620	1.0829E-01	0.9486
128×128	5.2782E-01	0.0658	1.2940E-01	0.5000	5.4356E-02	0.9942
256×256	5.1434E-01	0.0371	9.0733E-02	0.5120	2.7025E-02	1.0081
512×512	5.1359E-01	0.0020	6.4375E-02	0.4950	1.3529E-02	0.9982

Table 4.8: Convergent test using $\delta_h^{\surd}$ for indicator function case 3 : a simple closed curve.

Table 4.9 shows the convergence tests for this case with using $\delta_h^{\cos}$, and table 4.10 presents the computation results with using $\delta_h^{\surd}$, respectively. Figure 4.6 shows the comparison of numerical and analytic solution along the cross section $x = 0$. One can see that the maximum error of pressure occurs at the interface.

$M \times N$	$\|p - P_h\|_\infty$	ratio	$\|p - P_h\|_2$	ratio	$\|p - P_h\|_1$	ratio
32×32	1.5643E-00	–	9.5960E-01	–	2.0421E-00	–
64×64	1.7182E-00	-.1354	6.9177E-01	0.4720	1.1867E-00	0.7831
128×128	1.8342E-00	-.0943	4.9447E-01	0.4843	6.4868E-01	0.8712
256×256	1.9086E-00	-.0573	3.4999E-01	0.4985	3.4044E-01	0.9300
512×512	1.9284E-00	-.0149	2.4775E-01	0.4983	1.7495E-01	0.9604

Table 4.9: Convergent test using $\delta_h^{\cos}$ for Example 4.1.2.2.

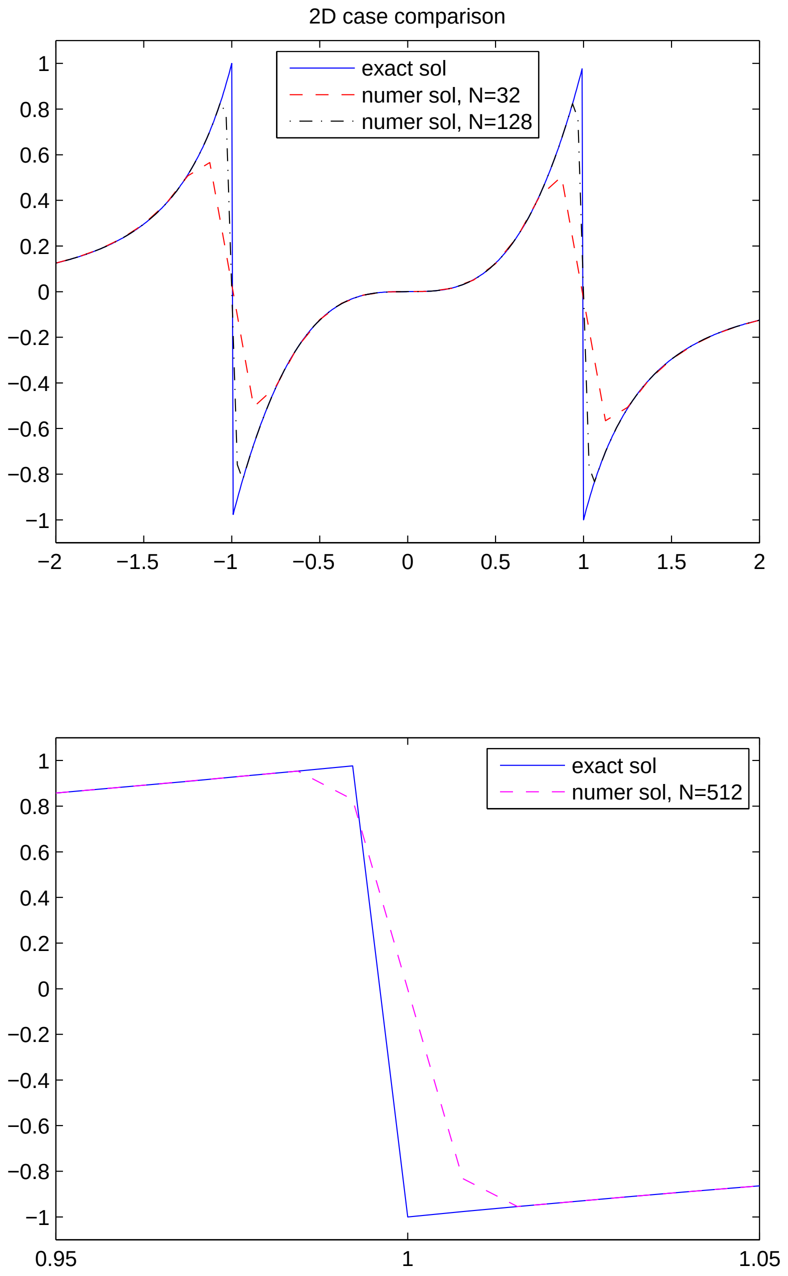

Figure 4.4: Comparison between numerical and analytic solutions for Example 4.1.2.2.

$M \times N$	$\|p - P_h\|_\infty$	ratio	$\|p - P_h\|_2$	ratio	$\|p - P_h\|_1$	ratio
32×32	1.5054E-00	–	8.4134E-01	–	1.5983E-00	–
64×64	1.6069E-00	-.1676	6.4567E-01	0.3818	9.4537E-01	0.7576
128×128	1.8046E-00	-.0938	4.7711E-01	0.4364	5.2107E-01	0.8594
256×256	1.8913E-00	-.0676	3.4350E-01	0.4740	2.7398E-01	0.9274
512×512	1.9219E-00	-.0231	2.4531E-01	0.4857	1.4085E-01	0.9599

Table 4.10: Convergent test using $\delta_h^{\surd}$ for Example 4.1.2.2.

Example 4.1.2.3: As a last example, we consider Eq. (48) in the square domain $\Omega = [-1, 1] \times [-1, 1]$ with analytic solutions. The interface Σ dividing Ω into inner part Ω_0 and outer part Ω_1, which is a simple closed curve written in polar coordinates $r = 0.5 + 0.25\cos(5\theta)$. The solution u is given by

$$u = \begin{cases} (x^2-1)(y^2-1)+1 & \text{if } (x,y) \in \Omega_0 \\ (x^2-1)(y^2-1) & \text{if } (x,y) \in \Omega_1 \end{cases}, \tag{55}$$

thus the boundary force $\mathbf{F}$ is simply the normal vector $\boldsymbol{n}$ along the interface Σ. The external source g can be easily computed from the solution u as $g = 2(x^2 + y^2 - 2)$.

The convergence tests based on $\delta_h^{\cos}$ are shown in table 4.11, while table 4.12 lists the corresponding order of accuracy with using $\delta_h^{\surd}$. Figure 4.7 shows the numerical and analytic solution along the line $y = 0$. It indicates that refining mesh could not improve the maximum error.

One can observe that the convergent results from example 2 and 3 are consistent with our conclusion, i.e. first-order accurate in L_1 norm, half-order accurate in L_2 norm, but have $O(1)$ errors in L_∞ norm.

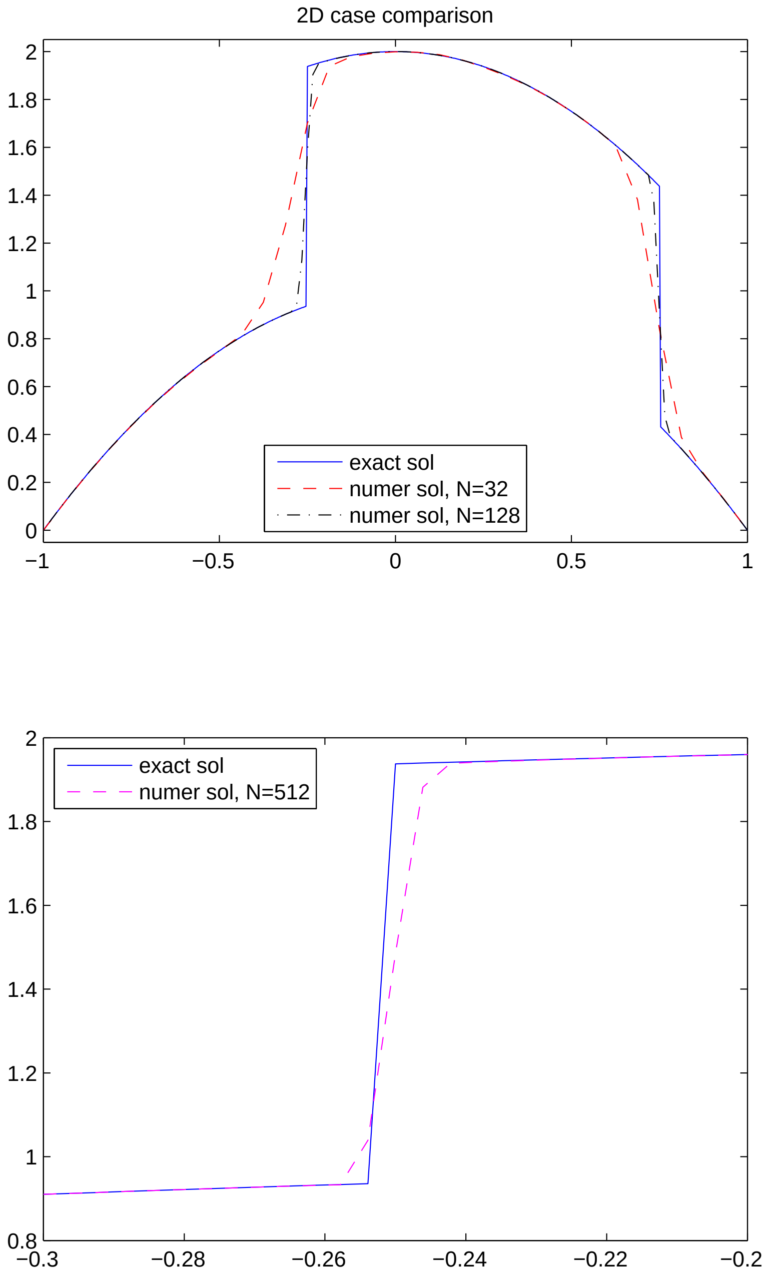

Figure 4.5: Comparison between numerical and analytic solutions for Example 4.1.2.3.

$M \times N$	$\|u - U_h\|_\infty$	ratio	$\|u - U_h\|_2$	ratio	$\|u - U_h\|_1$	ratio
32×32	9.7976E-01	–	4.6428E-01	–	3.6083E-01	–
64×64	9.8231E-01	-.0037	3.4142E-01	0.4434	1.9150E-01	0.9140
128×128	9.8129E-01	0.0015	2.4376E-01	0.4860	9.7187E-02	0.9784
256×256	9.8105E-01	0.0003	1.7146E-01	0.5075	4.8266E-02	1.0097
512×512	9.8169E-01	-.0009	1.2165E-01	0.4951	2.4217E-02	0.9950

Table 4.11: Convergent test using $\delta_h^{\cos}$ for Example 4.1.2.3.

$M \times N$	$\|u - U_h\|_\infty$	ratio	$\|u - U_h\|_2$	ratio	$\|u - U_h\|_1$	ratio
32×32	9.8024E-01	–	4.6421E-01	–	3.6094E-01	–
64×64	9.8190E-01	-.0024	3.4141E-01	0.4432	1.9136E-01	0.9155
128×128	9.8141E-01	0.0007	2.4374E-01	0.4861	9.7017E-02	0.9799
256×256	9.8090E-01	0.0007	1.7145E-01	0.5075	4.8187E-02	1.0095
512×512	9.8150E-01	-.0008	1.2164E-01	0.4952	2.4179E-02	0.9948

Table 4.12: Convergent test using $\delta_h^{\sqrt{}}$ for Example 4.1.2.3.

4.2 Convergent test for source terms as delta functions

In this section, we will show the convergent results of solving Poisson problems with source terms as delta functions. Since the conclusion we obtained depends on the moment condition of discrete delta functions, we pick up $\delta_h^{\cos}$ and $\delta_h^{\sqrt{}}$ from [4, 44] for comparison. The ratio in all tables of this section is the same as previous section, which means the orders of accuracy.

4.2.1 One-dimensional problem 2

In this subsection, we consider the following one-dimensional problem to verify the proof in section 3.2. The equation is

$$\frac{d^2u}{dx^2} = c\delta(x-\alpha) + g, \qquad 0 < x < 1. \tag{56}$$

Here, the interface is fixed at the point $\alpha = \pi/4 - 0.15$. The exact solution is given as

$$u(x) = \begin{cases} (x-\alpha)^3 & \text{if } x \le \alpha \\ (x-\alpha)^3 + cx + d & \text{if } x > \alpha \end{cases} \tag{57}$$

where the jump of derivative of solution u at the interface c is set as $c = -1$ and the constant d for keeping the continuity of u is $d = -c\alpha$ The regular source term g can be derived from the analytic solution, which is represented by $g(x) = 6(x-\alpha)$.

By using $\delta_h^{\cos}$, table 4.13 shows the order of accuracy for our test. Since this type of discrete delta function does not have the moment condition, the convergent rate is nearly of first order. In Table 4.14 we use $\delta_h^{\surd}$ to verify the conclusion we mention. In this case, the discrete delta function holds the moment condition, thus we can obtain the same result as we proved in previous subsection. Figure 4.8 shows that the maximum error is improving as the mesh is refining.

mesh	$\|u-U_h\|_\infty$	ratio	$\|u-U_h\|_2$	ratio	$\|u-U_h\|_1$	ratio
32	3.5924E-03	–	6.8746E-04	–	2.7290E-04	–
64	1.8555E-03	0.9531	2.5911E-04	1.4077	1.0378E-04	1.3948
128	9.0120E-04	1.0419	9.3268E-05	1.4740	4.3089E-05	1.2681
256	4.5930E-04	0.9724	3.6476E-05	1.3544	1.8986E-05	1.1823
512	2.2936E-04	1.0018	1.4989E-05	1.2830	9.4484E-06	1.0068

Table 4.13: Order of accuracy for one-dimensional test with $\delta_h^{\cos}$.

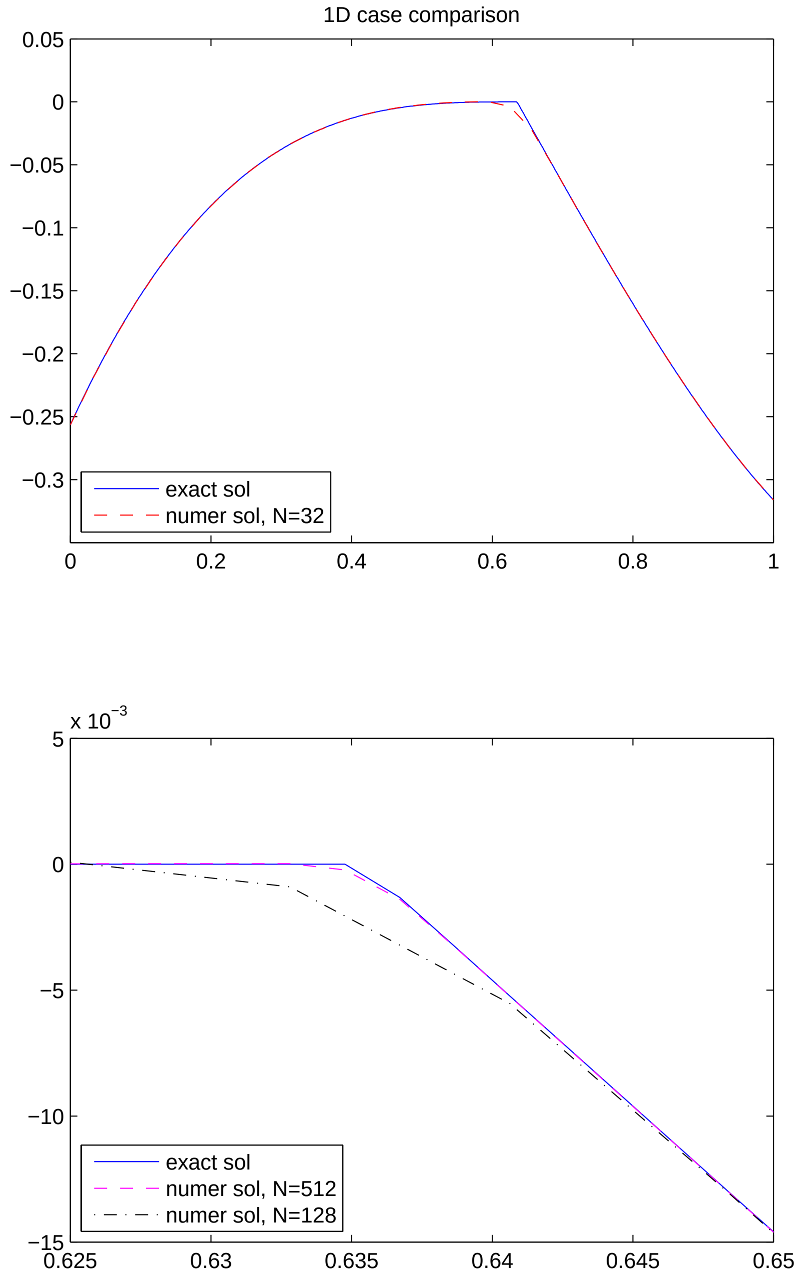

Figure 4.6: Comparison between numerical and analytic solutions for 1D case

mesh	$\|u-U_h\|_\infty$	ratio	$\|u-U_h\|_2$	ratio	$\|u-U_h\|_1$	ratio
32	3.7517E-03	–	6.9307E-04	–	1.5281E-04	–
64	1.8672E-03	1.0066	2.4420E-04	1.5049	3.8151E-05	2.0019
128	9.4225E-04	0.9867	8.6932E-05	1.4900	9.5640E-06	1.9960
256	4.6251E-04	1.0266	3.0318E-05	1.5197	2.3780E-06	2.0078
512	2.3990E-04	0.9470	1.1019E-05	1.4602	6.0116E-07	1.9838

Table 4.14: Order of accuracy for one-dimensional test with $\delta_h^{\sqrt{}}$.

4.2.2 Two-dimensional problems 2

In this subsection, the problems we need to solve can be written generally in the following formulation :

$$\Delta u = \int_\Gamma f(s)\,\delta^2(x-\mathbf{X}(s))\,ds + g \tag{58}$$

in the computational domain $\Omega = [a,b]\times[c,d]$ with an interface Σ inside, while the boundary conditions are still Dirichlet type. We use the same mesh structure as it was stated in previous section. Here, we use regular centered difference scheme to discrete Eq. (58) as

$$\frac{U_{i+1,j}-2U_{i,j}+U_{i-1,j}}{h^2}+\frac{U_{i,j+1}-2U_{i,j}+U_{i,j-1}}{h^2}=f_{i,j}+g_{i,j} \tag{59}$$

where

$$f_{i,j}=\sum_k f(s_k)\,\delta_h(x_i-X(s_k))\delta_h(y_j-Y(s_k))\,\Delta s. \tag{60}$$

Example 4.2.2.1: The first example is coming from LeVeque and Li's work [22]. The computational domain is $\Omega=[-1,1]\times[-1,1]$, and the interface Σ inside Ω is a circle centered at $(0,0)$ with radius 0.5. The analytic solution u is written in polar coordinates as

$$u(r)=\begin{cases}1 & \text{if } r\le 0.5\\ 1+\log(Cr) & \text{if } r>0.5\end{cases}, \tag{61}$$

where the jump on the interface $f=C$. Here, C is set to be 2, and the external source term g is zero, which can be verified easily.

The convergence tests based on $\delta_h^{\cos}$ are shown in table 4.15, while table 4.16 lists the corresponding order of accuracy with using $\delta_h^{\sqrt{\ }}$. Figure 4.9 shows the difference between numerical and analytic solutions near the interface. The maximum error is decreasing after the mesh refined.

$M \times N$	$\|u - U_h\|_\infty$	ratio	$\|u - U_h\|_2$	ratio	$\|u - U_h\|_1$	ratio
32×32	5.6933E-02	–	2.7227E-02	–	3.8063E-02	–
64×64	2.8740E-02	0.9862	1.3437E-02	1.0187	1.8874E-02	1.0120
128×128	1.4463E-02	0.9907	6.7304E-03	0.9974	9.4448E-03	0.9987
256×256	7.2452E-03	0.9972	3.3629E-03	1.0009	4.7169E-03	1.0016
512×512	3.6247E-03	0.9991	1.6816E-03	0.9998	2.3582E-03	1.0001

Table 4.15: Convergent test using $\delta_h^{\cos}$ for Example 4.2.2.1.

$M \times N$	$\|u - U_h\|_\infty$	ratio	$\|u - U_h\|_2$	ratio	$\|u - U_h\|_1$	ratio
32×32	3.2541E-02	–	1.0381E-02	–	5.6095E-03	–
64×64	1.6039E-02	1.0206	3.4241E-03	1.6000	1.3934E-03	2.0092
128×128	8.0821E-03	0.9887	1.2542E-03	1.4489	3.6329E-04	1.9393
256×256	4.0789E-03	0.9865	4.3528E-04	1.5267	9.1119E-05	1.9952
512×512	2.0854E-03	0.9678	1.5457E-04	1.4936	2.3011E-05	1.9854

Table 4.16: Convergent test using $\delta_h^{\sqrt{\ }}$ for Example 4.2.2.1.

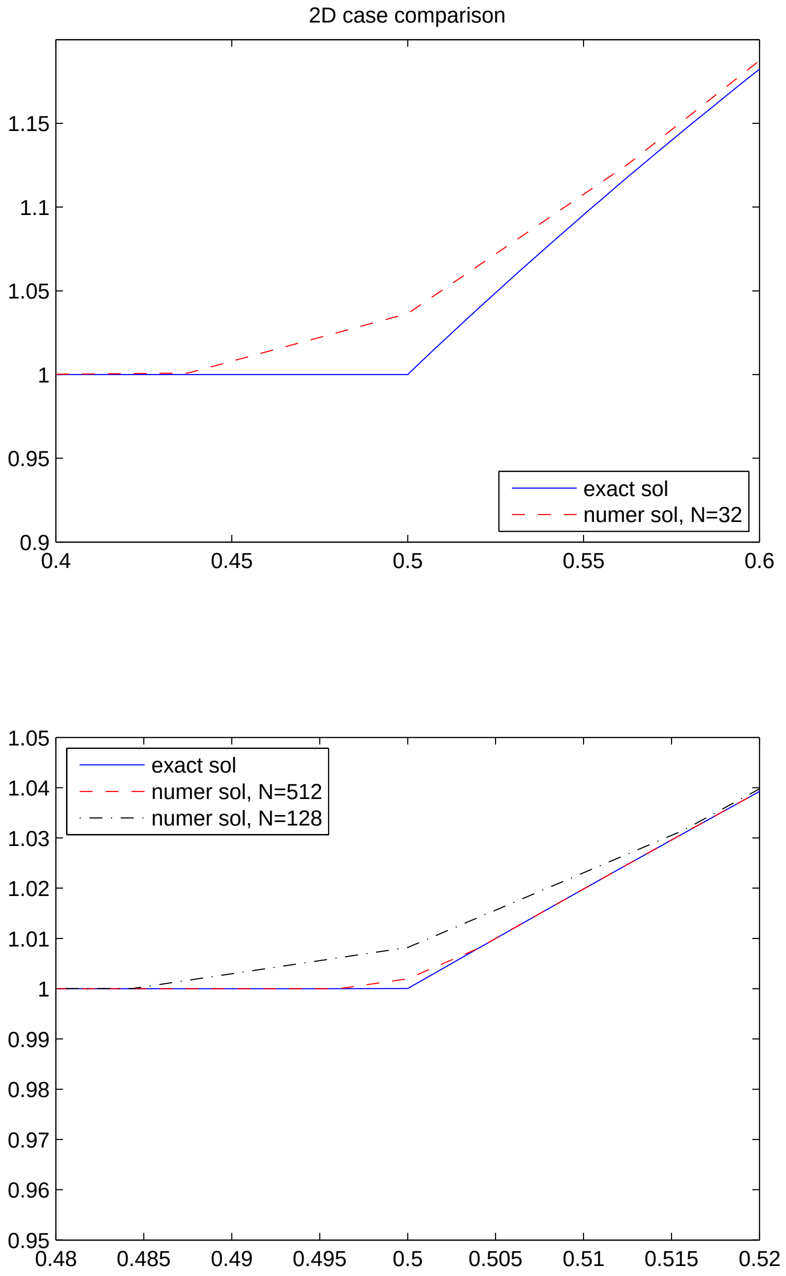

Figure 4.7: Comparison between numerical and analytic solutions for 2D case 4.2.2.1

Example 4.2.2.2: The next example is a modification from Zhou and his collaborators' work [47]. The domain Ω of the problem is $[-1,1]\times[-1,1]$, which contains an circular interface Σ centered at $(0,0)$ with radius 0.5. For convenience, the problem is described in the polar coordinates. The exact solution u is written as

$$u(r) = \begin{cases} r^2 & \text{if } r \leq 0.5 \\ 7/64 + r^4/4 + r^2/2 & \text{if } r > 0.5 \end{cases}. \tag{62}$$

The right hand side f is given by

$$g(r) = \begin{cases} 4 & \text{if } r \leq 0.5 \\ 4r^2 + 2 & \text{if } r > 0.5 \end{cases}, \tag{63}$$

with the source term on the interface $f = -0.375$.

The table 4.17 provides the convergence results based on $\delta_h^{\cos}$, while the corresponding order of accuracy with using $\delta_h^{\surd}$ is listed in table 4.18. Figure 4.10 shows the maximum error at the interface improves as the mesh number N increases.

$M\times N$	$\|u-U_h\|_\infty$	ratio	$\|u-U_h\|_2$	ratio	$\|u-U_h\|_1$	ratio
32×32	1.0692E-02	–	6.8852E-03	–	9.8518E-03	–
64×64	5.3116E-03	1.0092	2.9823E-03	1.2070	4.3218E-03	1.1887
128×128	2.6178E-03	1.0207	1.3325E-03	1.1622	1.9038E-03	1.1827
256×256	1.3075E-03	1.0015	6.5268E-04	1.0297	9.2571E-04	1.0402
512×512	6.7053E-04	0.9634	3.2934E-04	0.9867	4.6689E-04	0.9874

Table 4.17: Convergent test using $\delta_h^{\cos}$ for Example 4.2.2.2.

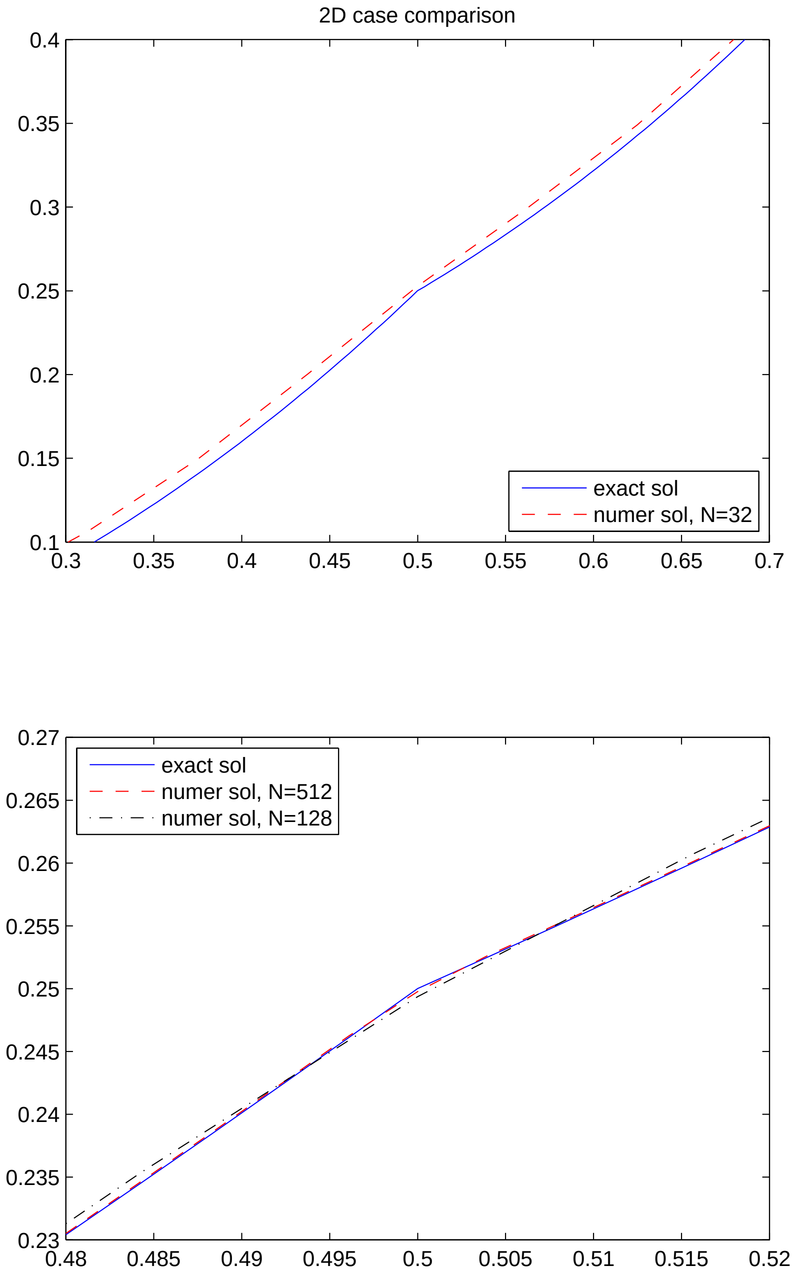

Figure 4.8: Comparison between numerical and analytic solutions for 2D case 4.2.2.2

$M \times N$	$\|u - U_h\|_\infty$	ratio	$\|u - U_h\|_2$	ratio	$\|u - U_h\|_1$	ratio
32×32	5.2739E-03	–	5.2757E-03	–	8.4898E-03	–
64×64	1.8829E-03	1.4858	1.7842E-03	1.5641	2.8787E-03	1.5603
128×128	1.1681E-03	0.6887	5.0356E-04	1.8250	7.9509E-04	1.8562
256×256	6.2013E-04	0.9135	1.9113E-04	1.3976	2.9956E-04	1.4082
512×512	3.1040E-04	0.9984	1.0044E-04	0.9282	1.5913E-04	0.9126

Table 4.18: Convergent test using $\delta_h^{\sqrt{}}$ for Example 4.2.2.2.

Example 4.2.2.3: The computational domain Ω of the final example is $[-1,1] \times [-1,1]$. There is an interface Σ inside the domain Ω, which is a circle centered at $(0,0)$ with radius 0.5. The analytic solution of u is given in the polar coordinates as

$$u(r) = \begin{cases} \exp(-r^2) & \text{if } r \le 0.5 \\ 1/(er^2) - 4/e + \exp(-1/4) & \text{if } r > 0.5 \end{cases} . \tag{64}$$

The source term on the interface $f = -16/e + \exp(-1/4)$, while the right hand side g could be derived as

$$g(r) = \begin{cases} 4(r^2 - 1)\exp(-r^2) & \text{if } r \le 0.5 \\ 4/(er^4) & \text{if } r > 0.5 \end{cases} . \tag{65}$$

The convergence tests based on $\delta_h^{\cos}$ are shown in table 4.19, while table 4.20 lists the corresponding order of accuracy with using $\delta_h^{\sqrt{}}$. Figure 4.11 shows the numerical solution converges to the analytic solution as we refine the grid.

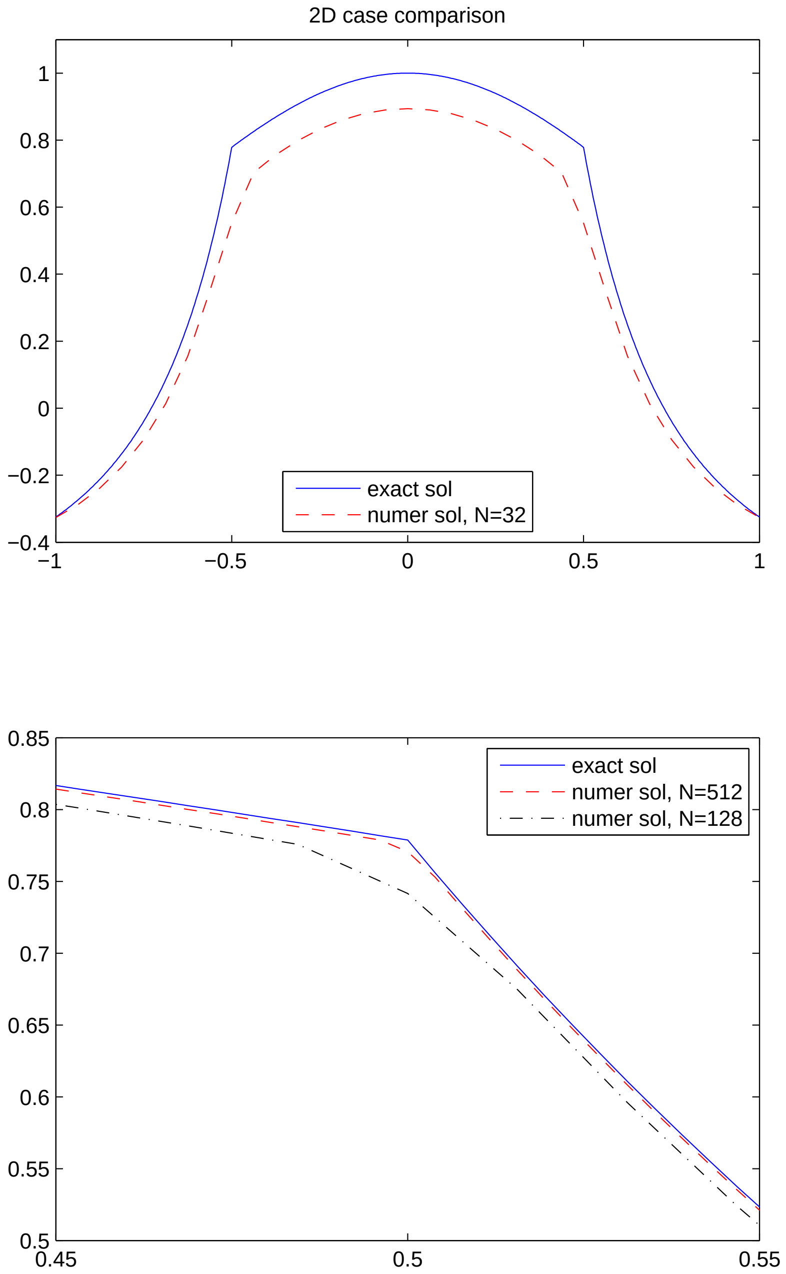

Figure 4.9: Comparison between numerical and analytic solutions for 2D case 4.2.2.3

$M \times N$	$\|u - U_h\|_\infty$	ratio	$\|u - U_h\|_2$	ratio	$\|u - U_h\|_1$	ratio
32×32	3.7152E-01	–	1.9625E-01	–	2.8326E-01	–
64×64	1.7040E-01	1.1245	8.1905E-02	1.2606	1.1891E-01	1.2522
128×128	7.7697E-02	1.1330	3.6186E-02	1.1785	5.1663E-02	1.2026
256×256	3.7131E-02	1.0652	1.7712E-02	1.0306	2.5111E-02	1.0408
512×512	1.8568E-02	0.9997	8.9366E-03	0.9869	1.2662E-02	0.9878

Table 4.19: Convergent test using $\delta_h^{\cos}$ for Example 4.2.2.3.

$M \times N$	$\|u - U_h\|_\infty$	ratio	$\|u - U_h\|_2$	ratio	$\|u - U_h\|_1$	ratio
32×32	2.1936E-01	–	1.3733E-01	–	2.0976E-01	–
64×64	9.0241E-02	1.2815	4.5147E-02	1.6049	6.9359E-02	1.5965
128×128	3.6605E-02	1.3017	1.2348E-02	1.8703	1.8486E-02	1.9076
256×256	1.6330E-02	1.1645	4.6871E-03	1.3974	7.1454E-03	1.3713
512×512	8.1021E-03	1.0111	2.5386E-03	0.8846	3.9730E-03	0.8467

Table 4.20: Convergent test using $\delta_h^{\surd}$ for Example 4.2.2.3.

4.3 Applications to indicator functions and pressure

The indicator function is not only providing a method to determine whether the position is in the inside region or the outside part of the closed interface, but also a useful tool to solve other kinds of partial differential equations. For example, this function can be applied when solving the following second-order variable-coefficient elliptic equation:

$$\nabla \cdot (\mathbf{b} \nabla \Psi) = f + \int_\Sigma g\, \delta^2(\mathbf{x} - \mathbf{X}(s))\, ds. \tag{66}$$

Here $\mathbf{b}$ is a piecewise constant coefficient matrix, i.e. $\mathbf{b} = \mathbf{b_0}$ inside Σ (in Ω_0), and $\mathbf{b} = \mathbf{b_1}$ outside Σ (in Ω_1). We may use the indicator function to represent $\mathbf{b}$ by

$$\mathbf{b} = \mathbf{b_1} + I(\mathbf{x})(\mathbf{b_0} - \mathbf{b_1}). \tag{67}$$

The source term on the surface g can be computed by

$$g = (\mathbf{b_1}\nabla\Psi_1 - \mathbf{b_0}\nabla\Psi_0)\cdot \boldsymbol{n}, \tag{68}$$

which is the jump of the normal derivative of the solution across the interface.

By using the indicator function, one can solve this type of equations without dealing with complex domain or complicated conditions on the boundary (interface). For convenience, we only use $\delta_h^{\sqrt{}}$ in the following computation.

4.3.1 One-dimensional problem 3

The equation (66) in one dimension could be rewrite as

$$\frac{d}{dx}\left(b\frac{d\Psi}{dx}\right) = f + g\delta(x - I_p)\ , \tag{69}$$

where I_p is the point that the interface lies in the domain.

To calculate the solution of equation (69), we adapt the simple discretization

$$\frac{b_{j+1/2}\frac{\Psi_{j+1}-\Psi_j}{\Delta x} - b_{j-1/2}\frac{\Psi_j-\Psi_{j-1}}{\Delta x}}{\Delta x} = f_{i,j} + g_{i,j} \tag{70}$$

Here $b_{j+1/2} = (b_{j+1}+b_j)/2$, $b_{j-1/2} = (b_j+b_{j-1})/2$. Let b be a piecewise constant coefficient in the compuational domain, where $b = b_L$ if the position $x < I_p$, and $b = b_R$ for the case $x > I_p$. By using the indicator function I(x) under the definition

$$I(x) = \begin{cases} 1 & \text{if } x > I_p \\ 0 & \text{if } x < I_p \end{cases}, \tag{71}$$

which can be calculated by solving the following equation

$$\frac{d^2 I}{dx^2} = \frac{d}{dx}\delta(x - I_p). \tag{72}$$

We can write the coefficient b_j as $b_j = b_L + I(x_j)(b_R - b_L)$.

Example 4.3.1: In the first example, we consider the equation (69) in the domain $[0, 4]$ with the exact solution

$$\Psi(x) = \begin{cases} (x+1)^2/b_L & \text{if } x < I_p \\ ((x+1)^2 + cx + d)/b_R & \text{if } x > I_p \end{cases}. \tag{73}$$

Here the interface point $I_p = 2\pi/3$, the right hand side function $f = 2$, and the jump condition $g = c = 1$. The coefficients $b_L = 1$ and $b_R = 10000$, while the constant d in the exact solution can be derived as

$$d = (I_p + 1)^2 \left(\frac{b_R}{b_L} - 1 \right) - cI_p \tag{74}$$

Table 4.21 shows the accuracy analysis of our scheme. One can find about first-order convergence obviously. Figure 4.12 provides the comparison between analytic and numerical solutions. The maximum error of numerical solution comes from the neighborhood of the interface point, but it will be improved after we refine the mesh.

mesh	$\|\Psi - \Psi_h\|_\infty$	ratio	$\|\Psi - \Psi_h\|_2$	ratio	$\|\Psi - \Psi_h\|_1$	ratio
32	1.3088E-00	–	1.1052E-00	–	1.3808E-00	–
64	5.7502E-01	1.1865	4.8300E-01	1.1942	6.0531E-01	1.1897
128	3.8643E-01	0.5733	3.2351E-01	0.5781	4.0480E-01	0.5804
256	1.9618E-01	0.9780	1.6407E-01	0.9795	2.0549E-01	0.9781
512	1.0032E-01	0.9676	8.3856E-02	0.9683	1.0508E-01	0.9676

Table 4.21: Order of accuracy for one-dimensional test with $\delta_h^{\surd}$.

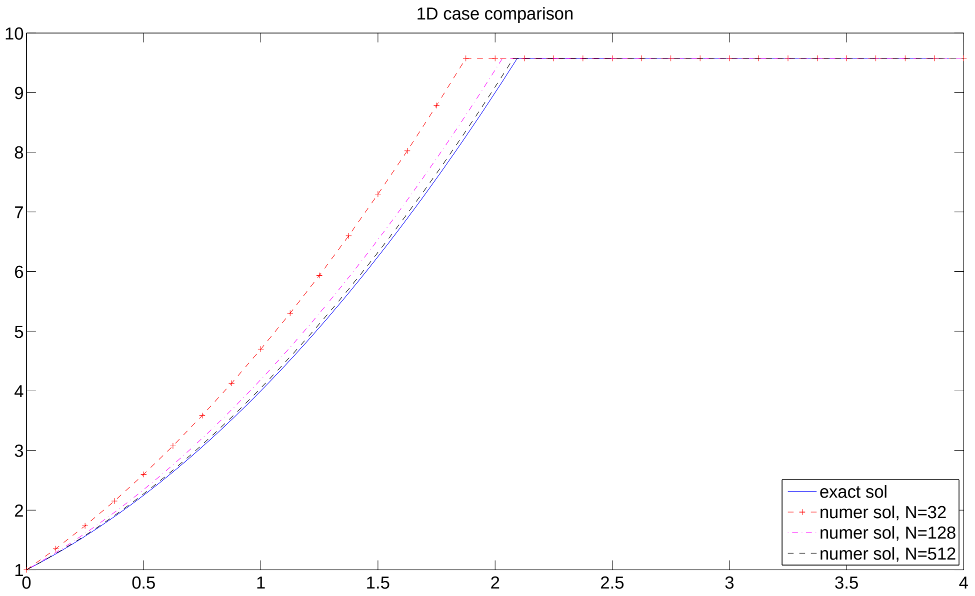

Figure 4.10: Comparison between numerical and analytic solutions for 1D case

4.3.2 Two-dimensional problems 3

In order to solve equation (66) in two-dimensional domain, we extend previous discretization in one-dimensional case as

$$\frac{b_{i+1/2,j}\frac{\Psi_{i+1,j}-\Psi_{i,j}}{\Delta x}-b_{i-1/2,j}\frac{\Psi_{i,j}-\Psi_{i-1,j}}{\Delta x}}{\Delta x} + \frac{b_{i,j+1/2}\frac{\Psi_{i,j+1}-\Psi_{i,j}}{\Delta y}-b_{i,j-1/2}\frac{\Psi_{i,j}-\Psi_{i,j-1}}{\Delta y}}{\Delta y} = f_{i,j}+g_{i,j}, \tag{75}$$

where

$$g_{i,j}=\sum_k g(s_k)\,\delta_h(x_i-X(s_k))\delta_h(y_j-Y(s_k))\,\Delta s. \tag{76}$$

Here we approximate the coefficients without integer index by taking averages of nearby values on the grid

$$\begin{aligned} b_{i+1/2,j} &= (b_{i+1,j}+b_{i,j})/2 \\ b_{i-1/2,j} &= (b_{i,j}+b_{i-1,j})/2 \\ b_{i,j+1/2} &= (b_{i,j+1}+b_{i,j})/2 \\ b_{i,j-1/2} &= (b_{i,j}+b_{i,j-1})/2 \end{aligned} \tag{77}$$

Example 4.3.2.1: The following example can be found in Beale and Layton's work [4]. The computational domain is $[-1.3, 1.3] \times [-1.31.3]$. There is an interface Γ, which is an ellipse, inside the domain with major radius $r_a = 0.9$ and minor radius $r_b = 0.7$. The whole problem is written in elliptic coordinates, which could defined by a conformal mapping $x + iy = a_0 \cosh(\rho + i\Theta)$, i.e. $x = a_0 \cosh\rho\cos\Theta$ and $y = a_0 \sinh\rho\sin\Theta$. Here $a_0 = \sqrt{r_a^2 - r_b^2} \approx 0.565685$ is the focus length of the ellipse. The interface Γ can be represented by $\Gamma = \{\rho = \rho_0 \approx 1.039721, 0 \leq \Theta \leq 2\pi\}$ in elliptic coordinates, which divides the domain into inner region Ω_0 and outer part Ω_1. The exact solution Ψ is

$$\Psi(\rho, \Theta) = \begin{cases} a_0^3(\cosh^2\rho\sinh\rho\cos^2\Theta\sin\Theta + \sinh^3\rho\sin^3\Theta) & \text{if } \rho < \rho_0 \\ c\exp(-3\rho)\sin(3\Theta) + d\exp(-\rho)\sin\Theta & \text{if } \rho > \rho_0 \end{cases}, \tag{78}$$

where $c \approx 1.267135$ and $d \approx 1.128542$ are given to provide the continuity of solution across interface. The constant coefficient inside the interface b_0 is set as $b_0 = 0.2$, while the one of outer region b_1 is equal to 100. Thus, the piecewise constant coefficient b can be defined as $b = b_1 + I(\boldsymbol{x})(b_0 - b_1)$. The right hand side function f to this problem is

$$f(\rho, \Theta) = \begin{cases} 8b_0a_0\sinh\rho\sin\Theta & \text{if } \rho < \rho_0 \\ 0 & \text{if } \rho > \rho_0 \end{cases}, \tag{79}$$

and the source term on the interface g can be derived by $g = (b_1\nabla\Psi_1 - b_0\nabla\Psi_0)\cdot\boldsymbol{n}$, where Ψ_1 and Ψ_0 are the limit of Ψ from outer region and that from inner area along normal direction, respectively.

Figure 4.13 shows the comparison between analytic solution and numerical solution on different grids, where we use the snapshot of the values along $x = 0$. One can see the maximum error occurs inside the interface, and the scale of error is decreasing as the mesh size is getting smaller. Table 4.22 lists the convergence rates of numerical solutions in different norms, which is about first-order.

$M \times N$	$\|u-U_h\|_\infty$	ratio	$\|u-U_h\|_2$	ratio	$\|u-U_h\|_1$	ratio
32×32	2.1097E-01	–	1.6389E-01	–	2.0212E-01	–
64×64	1.2118E-01	0.7999	9.5354E-02	0.7813	1.1720E-01	0.7863
128×128	6.4839E-02	0.9021	5.1056E-02	0.9012	6.2913E-02	0.8974
256×256	3.3470E-02	0.9539	2.6293E-02	0.9574	3.2434E-02	0.9558
512×512	1.7063E-02	0.9719	1.3393E-02	0.9731	1.6537E-02	0.9718

Table 4.22: Convergent test for Example 4.3.2.1.

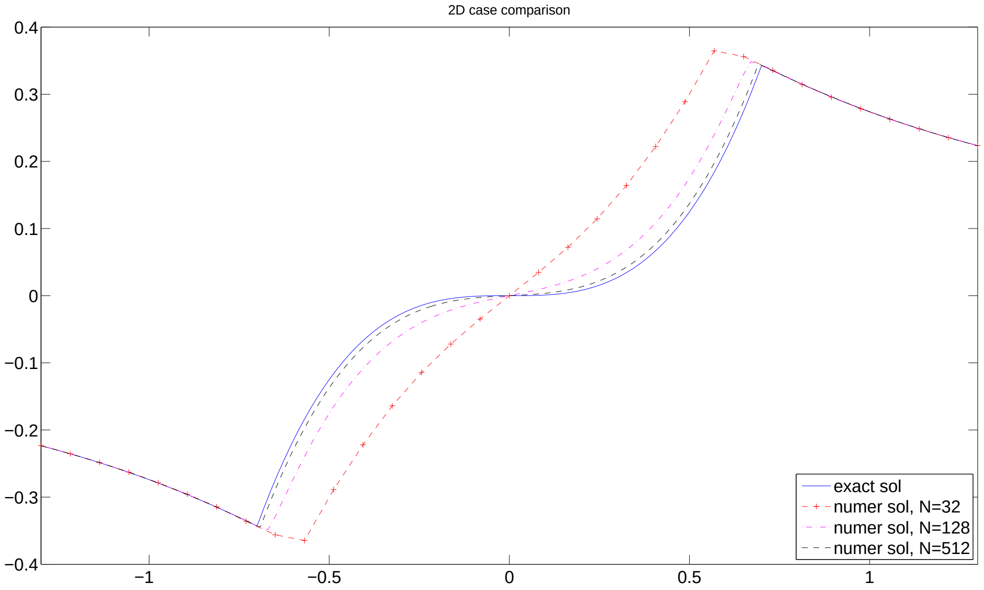

Figure 4.11: Comparison between numerical and analytic solutions for 2D case 4.3.2.1.

Example 4.3.2.2: The final example of this section is modified from Stokes problem in [14] and [23]. By using the pressure we have solved in example 4.1.2.2, we try to solve the velocity field by Eq. (1). The domain to the problem is $\Omega = [-2,2] \times [-2,2]$ with an interface inside, which is a unit circle centered at $(0,0)$, i.e. $\mathbf{X}(\theta) = (\cos\theta, \sin\theta)$. For convenience, the exact solution is written in polar coordinates as

$$u(r,\theta) = \begin{cases} 3r^2\sin(2\theta)/8 + r^4\sin(4\theta)/16 - r^4\sin(2\theta)/4 & \text{if } r \le 1 \\ r^{-2}\sin(2\theta)/8 - 3r^{-4}\sin(4\theta)/16 + r^{-2}\sin(4\theta)/4 & \text{if } r > 1 \end{cases}, \tag{80}$$

$$v(r,\theta) = \begin{cases} 3r^2\cos(2\theta)/8 - r^4\cos(4\theta)/16 - r^4\cos(2\theta)/4 & \text{if } r \le 1 \\ r^{-2}\cos(2\theta)/8 + 3r^{-4}\cos(4\theta)/16 - r^{-2}\cos(4\theta)/4 & \text{if } r > 1 \end{cases} \tag{81}$$

where u, v are the velocity in x direction and in y direction, respectively. The right hand side function is ∇p, which can be computed in component-wise direction by

$$\left(\frac{\partial p}{\partial x}\right)_{i,j} = \frac{p_{i+1,j} - p_{i-1,j}}{2\Delta x}, \qquad \left(\frac{\partial p}{\partial y}\right)_{i,j} = \frac{p_{i,j+1} - p_{i,j-1}}{2\Delta x}, \tag{82}$$

where $p_{i,j}$ is obtained in example 4.1.2.2. Again, the boundary force is $\boldsymbol{F}(\theta) = 2\,\sin(3\theta)\,\boldsymbol{X}(\theta)$.

Table 4.23-4.24 presents the computation results of velocity field in x-direction u and that in y-direction v, respectively. One can see first-order convergence in each component. Figure 4.14 shows the cross section of numerical solution of u along $x = y$, where we use x as horizontal index rather than exact distance from the origin. The interface and the line $x = y$ meets at $(\pm 1/\sqrt{2}, \pm 1/\sqrt{2}) \approx (\pm 0.7071, \pm 0.7071)$, one can observe that the maximum error occurs at the neighborhood of the interface. Figure 4.15 plots the cross section of numerical solution of v along x-axis. We can find similar behavior as that of u.

Moreover, we have to check if our numerical solutions satisfy Eq. (2) since we use it to derive our scheme. Table 4.25 shows the calculations of divergence of velocity field. The behavior of convergence is similar to numerical solution of pressure with first-order convergence in L_1 norm and half-order convergence in L_2 norm, but there is an $O(1)$ error in maximum norm. Figure 4.16 shows the divergence of velocity field of our numerical solutions. One can see most of the error lies near the interface.

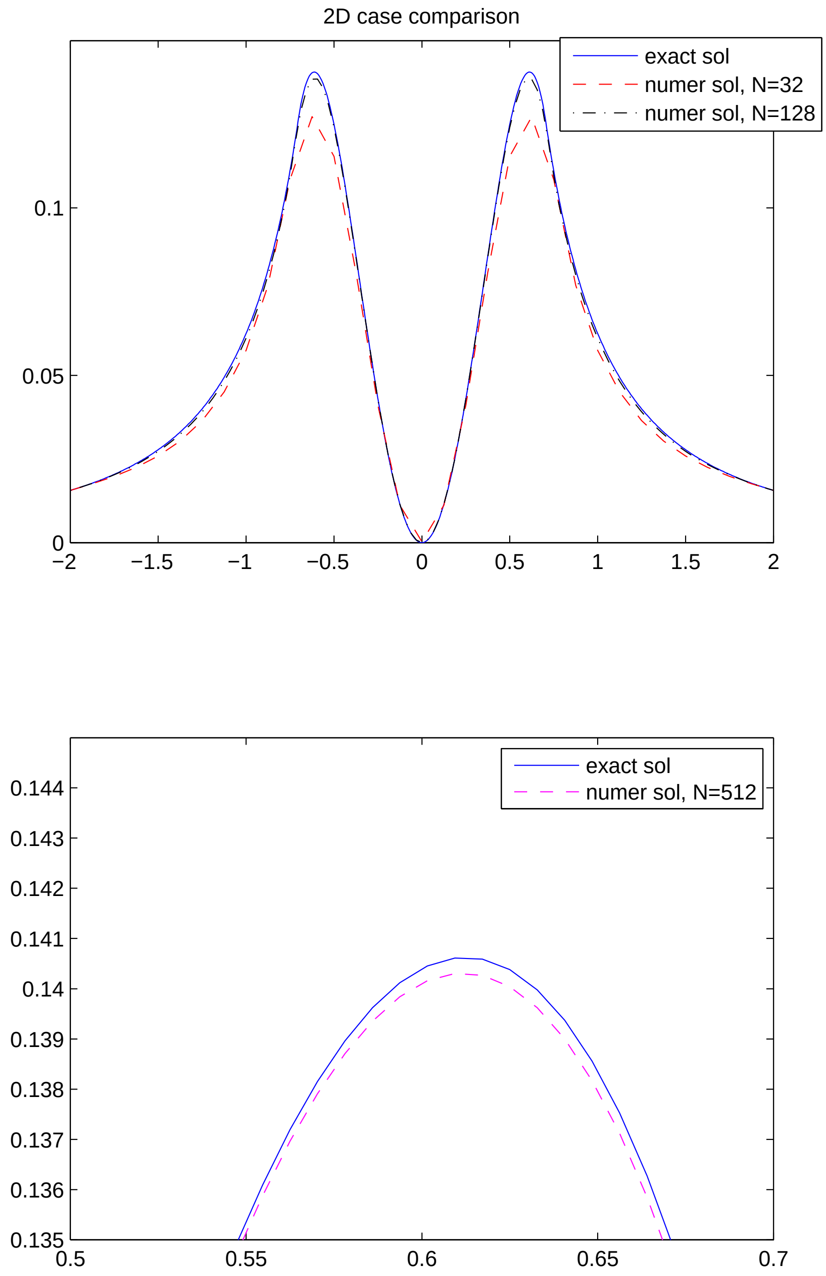

Figure 4.12: Comparison between numerical and analytic solutions for u in case 4.3.2.2.

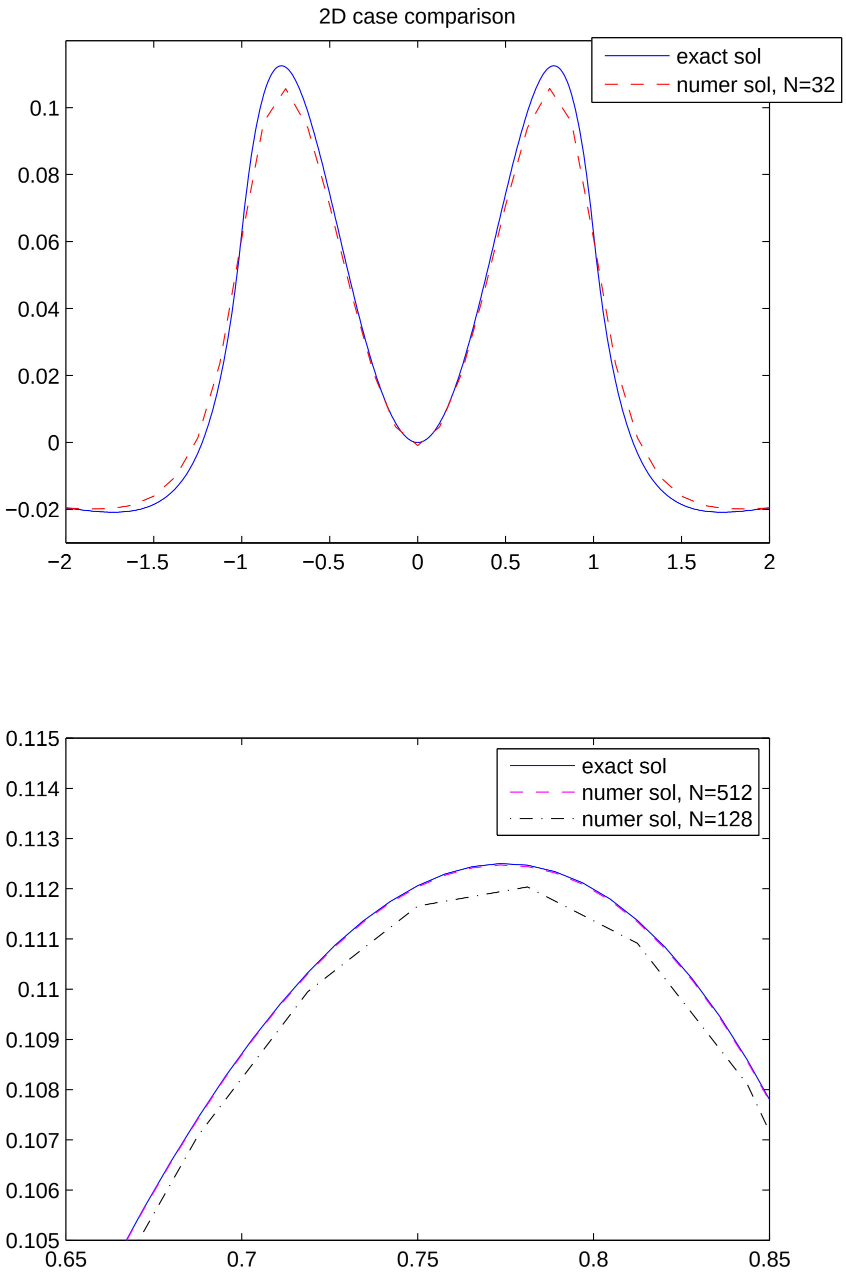

Figure 4.13: Comparison between numerical and analytic solutions for v in case 4.3.2.2.

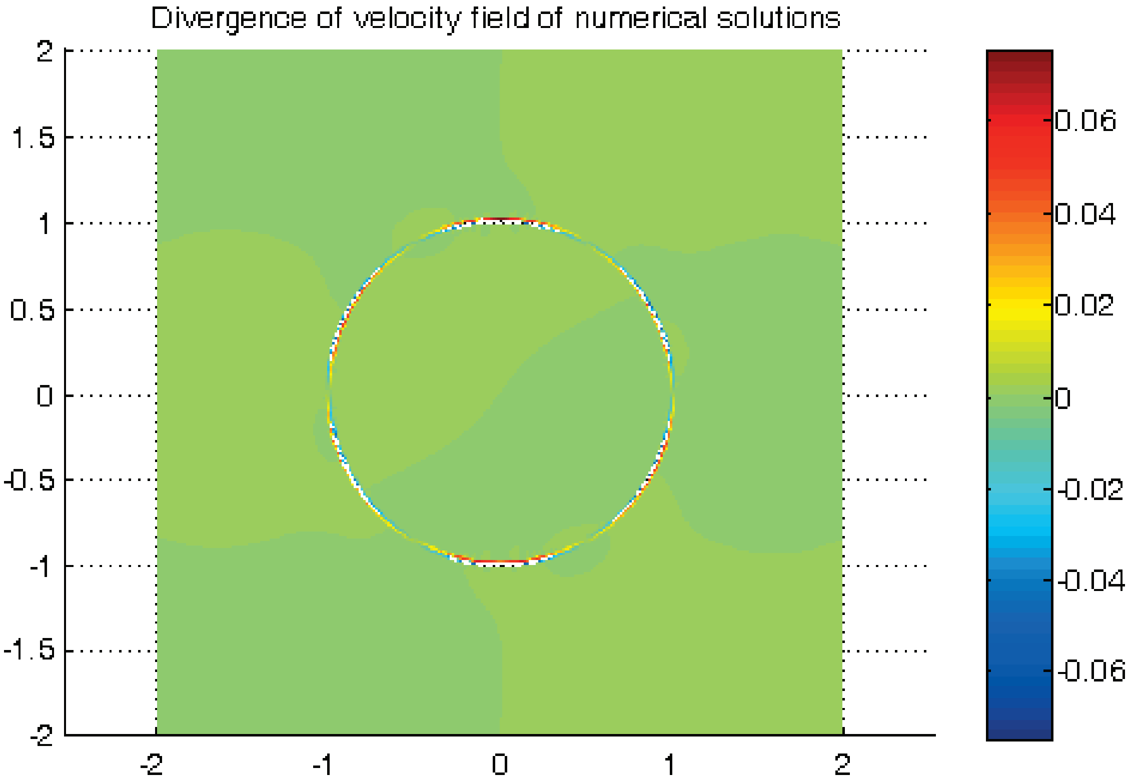

Figure 4.14: Divergence of velocity field of numerical solution in case 4.3.2.2.

$M \times N$	$\|u - U_h\|_\infty$	ratio	$\|u - U_h\|_2$	ratio	$\|u - U_h\|_1$	ratio
32×32	1.5926E-02	–	1.9452E-02	–	5.2813E-02	–
64×64	8.1197E-03	0.9719	9.2765E-03	1.0682	2.5472E-02	1.0519
128×128	4.7473E-03	0.7743	4.5961E-03	1.0131	1.2788E-02	0.9941
256×256	2.5170E-03	0.9154	2.2974E-03	1.0003	6.4287E-03	0.9921
512×512	1.3052E-03	0.9473	1.1499E-03	0.9985	3.2258E-03	0.9948

Table 4.23: Convergent test of u for Example 4.3.2.2.

$M \times N$	$\|v - V_h\|_\infty$	ratio	$\|v - V_h\|_2$	ratio	$\|v - V_h\|_1$	ratio
32×32	1.8223E-02	–	1.9585E-02	–	5.3126E-02	–
64×64	8.5764E-03	1.0873	9.5074E-03	1.0426	2.5785E-02	1.0429
128×128	4.6931E-03	0.8698	4.7328E-03	1.0063	1.2865E-02	1.0030
256×256	2.5314E-03	0.8906	2.3682E-03	0.9989	6.4465E-03	0.9968
512×512	1.3107E-03	0.9495	1.1855E-03	0.9982	3.2308E-03	0.9966

Table 4.24: Convergent test of v for Example 4.3.2.2.

$M \times N$	$\|\nabla \cdot \boldsymbol{u}_h\|_\infty$	ratio	$\|\nabla \cdot \boldsymbol{u}_h\|_2$	ratio	$\|\nabla \cdot \boldsymbol{u}_h\|_1$	ratio
32×32	6.2054E-02	–	5.4389E-02	–	1.2858E-01	–
64×64	6.7047E-02	-.1116	3.9285E-02	0.4693	7.0513E-02	0.8667
128×128	6.9974E-02	-.0616	2.7684E-02	0.5049	3.5625E-02	0.9849
256×256	7.2527E-02	-.0516	1.9457E-02	0.5087	1.7657E-02	1.0126
512×512	7.3314E-02	-.0155	1.3699E-02	0.5062	8.7447E-03	1.0137

Table 4.25: Convergent test of $\nabla \cdot \boldsymbol{u}_h$ for Example 4.3.2.2.

Part II

Computational methods on interfacial flows with soluble surfactant

Chapter 5

Introduction 2

There are many problems in physical, biological and material sciences needing to solve partial differential equations in complex domains or deformable interfaces. Especially, the material quantities which we interest on the interface may interact with the one in the bulk domain through desorption and adsorption processes. At the same time, the concentration of quantities on the surface may change the interfacial forces, which lead to the modification of the physical behavior of the interface. For instance, The structure of the surfactant molecules typically consists of a hydrophilic head, which tends to lie in the water, and a hydrophobic tail, which likes to stay in the oil or other liquid rather than in the water.

The interaction such as adsorption and desorption between the interface and the bulk fluids would change the concentration of surfactant on the surface, thus the surface tension could be reduced. Meanwhile, the dynamics is also affected by the Marangoni force along the tangential direction of the surface, which is produced by the non-uniform distribution of surfactant molecules. In practice, the surfactant might be soluble into only some portion of the bulk domain. This region is enclosed by the interface, where the soluble area and the interface are evolving at the same time. In order to simulate this problem, the following two surfactant concentrations are introduced in this system: one is the volume concentration in the bulk domain, and the other is the surface concentration along the interface. Thus, we need to solve a coupled system of surface-bulk convection-diffusion

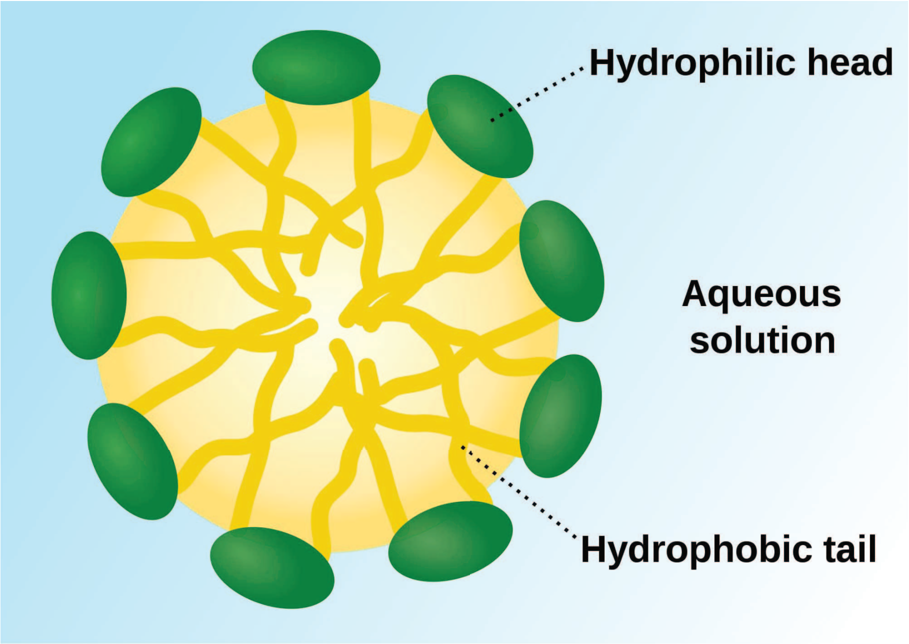

Figure 5.1: Schematic diagram of surfactant particles with hydrophilic heads and hydrophobic tails, cited from "http://en.wikipedia.org/wiki/Surfactant".

equations [28, 46, 40].

In cell biology applications [30], some kinds of mobile proteins exists both in the cytosol and cell membrane. They could diffuse both inside the cell and on the membrane. The process that the proteins bind to the membrane correlates with initiation of downstream signaling. To simulate this type of problems, we have to solve a coupled system of interface-volume reaction-diffusion equations. There are many examples in material science, physics, or biologies that have the similar mechanisms such as absorption or desorption in the dynamics, one can found those in the reference [40].

It is a well-known challenging problem to solve differential equations in complex domains or deformable interface in numerical methods, especially when the surface, or the interior boundary of domains is moving. To deal with a coupled system of surface-bulk equations is more complicated. Even in the case of solving surface quantities only, i.e. without coupling those in the bulk region, it is still a major issue in scientific computing community that to develop better numerical methods for convection-diffusion equations on an evolving interface.

It is known that solving a coupled system of surface-bulk equations in complex domains or deformable interfaces numerically is quite challenging especially when the interface (or the interior boundary of domains) is moving. Even in the case of only surface material (without bulk coupling), developing numerical methods for convection-diffusion equations on an evolving interface is still of major interest in scientific computing community. These methods include phase field method [35, 40, 17], level set method [2, 9, 43, 36, 27], surface element method [7, 8, 15, 16], and much more to follow. In one-dimensional case, front tracking method is typically more accurate for interface problem, since it only deals with a curve in 2D space. But the complexity for two-dimensional surface is more difficult to use this type of methods, especially the implementation involves surface mesh distortion or even topological changes.

In[24], we have successfully developed a mass conservative scheme for convection-diffusion equation on moving interface and applied to simulate the interfacial flows with insoluble surfactant [24, 25, 26]. A recent work of Khatri and Tornberg [20] used segment projection method to represent the interface and solve the surfactant equation. More up-to-dated numerical methods for solving Navier-Stokes flows with insoluble surfactant can be found in [20] as well.

In this part, we shall extend our previous work of insoluble surfactant to soluble case. However, as a very first step, we need to develop a numerical scheme for solving coupled surface-bulk convection-diffusion equations. From our point of view, there are several major numerical issues to deal with. The first problem is how to handle the flux between the interface and the bulk from the adsorption and desorption accurately? The second question is how to maintain the mass conservation of total surfactant during the evolution? The third issue is how to avoid the surfactant being present in other bulk regions via either convection or diffusion mechanism if the surfactant might be soluble to only one of buck fluid? Here, we formulate the coupled surface-bulk convection-diffusion equations in the immersed boundary framework so that the adsorption and desorption processes can be termed as a singular source in the bulk equation. Moreover, by using the indicator function, we can embed the bulk equation into the whole computational domain so that regular Eulerian finite difference scheme can be applied without handling the complicated moving irregular domain. We develop a new conservative scheme for solving the coupled bulk-surface concentration equations which the total surfactant mass can be conserved exactly in discrete sense. By introducing the indicator function and solving the bulk equation in the regular computational domain, one can avoid evaluating the surfactant flux across the interface due to adsorption and desorption processes.

The present formulation is similar to other front tracking approaches such as in [46, 28] but differs from their numerical computations. For instance, in order to let the surfactant be depleted from only one bulk phase, some one-sided discretized delta functions were used in [46] which results the numerical integration of the discrete function does not yield the exact value of unity. The authors have tried different forms of one-sided delta function and the mass error is within 1%. Here, we use the traditional discrete delta function for the spreading and interpolating operators in the immersed boundary method so that the surfactant mass leaking error is much smaller compared with [46]. There are other numerical methods in literature for interfacial flows with soluble surfactant dynamics such as in [1, 6, 41, 45].

The rest of this part is organized as follows. In Chapter 6, we present a coupled surface-bulk concentration model for surfactant and show their property about conservation of mass. By applying the indicator function, we then embed the bulk equation from irregular region into a regular Cartesian computational domain. Based on our immersed boundary formulation, we develop a conservative scheme for solving the coupled surface-bulk equations in Chapter 7. As an application, we apply the present scheme to solve Navier-Stokes flow with soluble surfactant in Chapter 8. In Chapter 9, a detailed numerical tests have been conducted to validate our present scheme and study the effect of soluble surfactant on drop deformations in a quiescent and shear flow.

Chapter 6

A coupled surface-bulk concentration model

As in [40], we consider the same coupled bulk-surface material (or surfactant) concentration model in which the adsorption and desorption can be occurred on the moving deformable interface. Consider a domain Ω in R^2 and there is an interface Σ, which is a simple closed curve immersed in Ω. The interior of the interface is Ω_0, and the exterior is Ω_1 so that $\Omega = \Omega_0 \cup \Omega_1$, see the illustration of these domains in Figure 1. The interface is represented by a Lagrangian form $\boldsymbol{X}(\alpha, t), 0 \leq \alpha \leq L_b$, where α is the Lagrangian material coordinate attached to the interface which is not necessarily to be the arc-length parameter. The unit tangent vector of the interface can be written as $\boldsymbol{\tau} = \frac{\partial \boldsymbol{X}}{\partial \alpha} / \left| \frac{\partial \boldsymbol{X}}{\partial \alpha} \right|$; thus, the unit outward normal vector $\boldsymbol{n}$ pointing into Ω_1 can be defined accordingly. In addition, the interface Σ is moving with a given velocity field $\boldsymbol{u} = (u, v)$ in Ω; that is,

$$\frac{\partial \boldsymbol{X}(\alpha, t)}{\partial t} = \boldsymbol{U}(\alpha, t) = \int_{\Omega} \boldsymbol{u}(\boldsymbol{x}, t) \delta^2(\boldsymbol{x} - \boldsymbol{X}(\alpha, t))\, d\boldsymbol{x}, \tag{83}$$

where $\delta^2(\boldsymbol{x}) = \delta(x)\,\delta(y)$ is the two-dimensional Dirac delta function. We use the above usual delta function formulation in the immersed boundary method [32] to represent the interpolation of the velocity field into the interface. Here we assume the velocity field is incompressible ($\nabla \cdot \boldsymbol{u} = 0$) in Ω and no flow boundary condition ($\boldsymbol{u} \cdot \boldsymbol{n}_1 = 0$) is imposed on $\partial\Omega = \partial\Omega_1$. Notice that, in later section, the velocity field can be obtained by solving the Navier-Stokes equations.

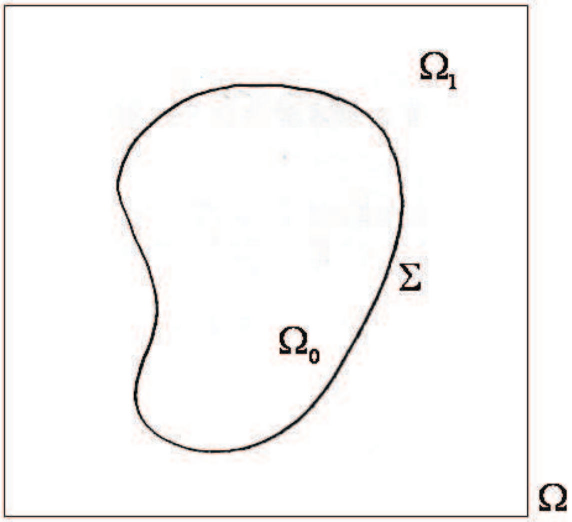

Figure 6.1: Illustration of domains.

It is assumed that the surfactant exists on the interface as a monolayer and is adsorbed from or desorbed into the bulk fluid in Ω_1; that is, the surfactant is soluble in the exterior bulk Ω_1 but not in the interior one Ω_0. Therefore, we have to introduce two surfactant concentrations in the system; namely, the surface concentration $\Gamma(\alpha, t)$ along the interface Σ, and the bulk concentration $C(x, y, t)$ in the region Ω_1.

Assume the surfactant concentration $\Gamma(s, t)$ on an interfacial segment $L(t)$ is defined as the mass of the surfactant per unit length. Since there is no absorption or desorption between the surface and the surrounding bulk fluids, the surfactant would remain on the surface element, i.e. the total mass is conserved.

$$\frac{d}{dt}\int_{L(t)} \Gamma(s,t)\, ds \;= 0, \tag{84}$$

where s is arc-length parameter and ds is the arc-length element. In order to adapt our parameterization mentioned before, we rewrite the above equation in terms of Lagrangian material coordinate α as

$$\frac{d}{dt}\int_{L(0)} \Gamma(\alpha,t)\left|\frac{\partial \boldsymbol{X}}{\partial \alpha}\right| d\alpha = 0. \tag{85}$$

By taking the time derivative inside the integral, we get

$$\int_{L(0)} \frac{\partial \Gamma(\alpha,t)}{\partial t}\left|\frac{\partial \boldsymbol{X}}{\partial \alpha}\right| + \Gamma(\alpha,t)\frac{\partial}{\partial t}\left|\frac{\partial \boldsymbol{X}}{\partial \alpha}\right| \, d\alpha = 0. \tag{86}$$

Note that we use Lagrangian structure to track the interface and the surfactant. Therefore, the time derivative of the first term in Eq. (86) is exactly the material derivative of Stone's derivation [18]. The time derivative of the second term is due to interface stretching. Let $\boldsymbol{X}(\alpha,t) = (X(\alpha,t), Y(\alpha,t))$, and $\boldsymbol{U}(\alpha,t) = (U(\boldsymbol{X},t), V(\boldsymbol{X},t))$ be the Lagrangian representation of the position and the velocity of interface, respectively. Since

$$\left|\frac{\partial \boldsymbol{X}}{\partial \alpha}\right| = \sqrt{\left(\frac{\partial X}{\partial \alpha}\right)^2 + \left(\frac{\partial Y}{\partial \alpha}\right)^2}\,, \tag{87}$$

by using the fact that

$$\frac{\partial \boldsymbol{X}(\alpha,t)}{\partial t} = \boldsymbol{U}(\alpha,t), \tag{88}$$

We obtain

$$\begin{aligned}
\frac{\partial}{\partial t}\left|\frac{\partial \boldsymbol{X}}{\partial \alpha}\right| &= \frac{\frac{\partial X}{\partial \alpha}\frac{\partial}{\partial \alpha}\frac{\partial X}{\partial t} + \frac{\partial Y}{\partial \alpha}\frac{\partial}{\partial \alpha}\frac{\partial Y}{\partial t}}{\left|\frac{\partial \boldsymbol{X}}{\partial \alpha}\right|} = \frac{\frac{\partial X}{\partial \alpha}\frac{\partial U}{\partial \alpha} + \frac{\partial Y}{\partial \alpha}\frac{\partial V}{\partial \alpha}}{\left|\frac{\partial \boldsymbol{X}}{\partial \alpha}\right|} \\
&= \frac{\frac{\partial X}{\partial \alpha}\left(\nabla U \cdot \frac{\partial \boldsymbol{X}}{\partial \alpha}\right) + \frac{\partial Y}{\partial \alpha}\left(\nabla V \cdot \frac{\partial \boldsymbol{X}}{\partial \alpha}\right)}{\left|\frac{\partial \boldsymbol{X}}{\partial \alpha}\right|} = \left(\frac{\partial \boldsymbol{U}}{\partial \boldsymbol{\tau}} \cdot \boldsymbol{\tau}\right)\left|\frac{\partial \boldsymbol{X}}{\partial \alpha}\right| \\
&= (\nabla_s \cdot \boldsymbol{U})\left|\frac{\partial \boldsymbol{X}}{\partial \alpha}\right|
\end{aligned} \tag{89}$$

Here, the notation $\nabla_s \cdot \boldsymbol{U}$ means the surface divergence of velocity, which is widely used in the literature. Since the interface segment is chosen arbitrary, we have

$$\frac{\partial \Gamma}{\partial t} + (\nabla_s \cdot \boldsymbol{U})\Gamma = 0. \tag{90}$$

By taking the adsorption and desorption of bulk surfactant into account, the dimensionless surface concentration equation can be modified as

$$\frac{\partial \Gamma}{\partial t} + (\nabla_s \cdot \boldsymbol{u})\,\Gamma = \frac{1}{Pe_s}\,\nabla_s^2 \Gamma + (S_a/\lambda)C_s(1-\Gamma) - S_d\Gamma, \tag{91}$$

where $\nabla_s = (\boldsymbol{I} - \boldsymbol{n} \otimes \boldsymbol{n})\nabla$ and $\nabla_s^2 = \nabla_s \cdot \nabla_s$ are the surface gradient and surface Laplacian operators, respectively. The dimensionless number Pe_s is the surface Peclet number, S_a

and S_d are the absorption and desorption Stanton number, respectively, and λ is the dimensionless adsorption depth. Those parameters are defined as

$$Pe_s = U_\infty R/D_s, \quad S_a = k_a/U_\infty, \quad S_d = k_d R/U_\infty, \quad \lambda = \Gamma_\infty/(C_\infty R)$$

where $R, U_\infty, \Gamma_\infty, C_\infty$ are the reference values for the length, flow velocity, the surface and bulk concentration, and k_a, k_d are the absorption and desorption coefficients. C_s is the bulk surfactant concentration adjacent to the interface which can be defined later. The above non-dimensionalization process can be found in [46, 28, 24]. Notice that, as in [24], the interface is tracked in Lagrangian manner and the surface concentration is defined at the material point, so the time derivative in Eq. (91) has the meaning of the material derivative naturally.

The dimensionless bulk concentration in the exterior region Ω_1 [28, 40, 41, 46] can be written as

$$\frac{\partial C}{\partial t} + \boldsymbol{u} \cdot \nabla C = \frac{1}{Pe} \nabla^2 C \tag{92}$$

$$\frac{1}{\lambda Pe} \frac{\partial C}{\partial \boldsymbol{n}}|_\Sigma = (S_a/\lambda) C_s (1 - \Gamma) - S_d \Gamma \qquad \frac{\partial C}{\partial \boldsymbol{n}_1}|_{\partial \Omega_1} = 0, \tag{93}$$

where Pe is the Peclet number, $\boldsymbol{n}$ is the unit normal vector on Σ pointing into Ω_1 and $\boldsymbol{n}_1$ is the unit outward normal to the boundary $\partial\Omega_1 = \partial\Omega$.

Eqs. (91)-(93) describe the present coupled surface-bulk concentration equations. Since the fluid is incompressible and no flow velocity boundary condition is imposed on $\partial\Omega_1$, one can conclude that the total surfactant mass (the surfactant mass on the interface Σ and the mass in the bulk region Ω_1) must be conserved. The conservation property can be proved easily as follows.

By first taking the integration of Γ over the interface, then applying the time derivative and using Eq. (91), the rate of change of surfactant mass in the interface Σ can be written as

$$\begin{aligned} \frac{d}{dt} \int_\Sigma \Gamma dl &= \int_\Sigma \left(\frac{\partial \Gamma}{\partial t} + (\nabla_s \cdot \boldsymbol{u}) \Gamma \right) dl \\ &= \int_\Sigma \left(\frac{1}{Pe_s} \nabla_s^2 \Gamma + (S_a/\lambda) C_s (1 - \Gamma) - S_d \Gamma \right) dl \\ &= \int_\Sigma ((S_a/\lambda) C_s (1 - \Gamma) - S_d \Gamma) dl, \end{aligned} \tag{94}$$

where $dl = \left|\frac{\partial \boldsymbol{X}}{\partial \alpha}\right| d\alpha$ is the arc-length element. The last equality is obtained by using the fact that Σ is a closed interface. Similarly, the rate of change of surfactant mass in the bulk region Ω_1 can be obtained by taking the integration of C over the region Ω_1, applying the time derivative, and then using Eq. (92) as

$$\begin{aligned} \frac{d}{dt}\int_{\Omega_1} C d\boldsymbol{x} &= \int_{\Omega_1} \frac{DC}{Dt} d\boldsymbol{x} = \int_{\Omega_1} \frac{1}{Pe}\nabla^2 C d\boldsymbol{x} = \int_{\partial\Omega_1} \frac{1}{Pe}\frac{\partial C}{\partial \boldsymbol{n}_1} dl - \int_{\Sigma} \frac{1}{Pe}\frac{\partial C}{\partial \boldsymbol{n}} dl \\ &= -\int_{\Sigma} (S_a C_s(1-\Gamma) - S_d \lambda \Gamma) dl, \end{aligned} \tag{95}$$

where the last equality is obtained by using the boundary conditions of Eq. (93). One can immediately lead to the total surfactant mass conservation by summing Eq. (94) and Eq. (95) so we have

$$\frac{d}{dt}\left(\int_{\Omega_1} C d\boldsymbol{x} + \lambda \int_{\Sigma} \Gamma dl\right) = 0. \tag{96}$$

6.1 An embedding bulk concentration equation in a regular Cartesian domain

As mentioned before, solving the bulk concentration equation involves solving a convection-diffusion equation in an evolving irregular domain Ω_1. In order to describe the solution in a regular Cartesian domain $\Omega = \Omega_0 \cup \Omega_1$, we introduce the indicator function H defined as

$$H(\boldsymbol{x}, t) = 1 - \int_{\Omega_0} \delta^2(\boldsymbol{x} - \tilde{\boldsymbol{x}})\, d\tilde{\boldsymbol{x}} = \begin{cases} 1 & \text{if} \quad \boldsymbol{x} \in \Omega_1 \\ 0 & \text{if} \quad \boldsymbol{x} \in \Omega_0 \end{cases} \tag{97}$$

In the previous part, we use the indicator function I to point out the inner subdomain Ω_0. Here, instead of using I, we use the opposite function H to indicate the outer region. The above indicator function is nothing but the Heaviside function across the interface. By taking the gradient and then divergence operators on both sides, we have

$$\begin{aligned} \nabla H(\boldsymbol{x}, t) &= \int_{\Sigma} \boldsymbol{n}\, \delta^2(\boldsymbol{x} - \boldsymbol{X})\, dl, \\ \nabla^2 H(\boldsymbol{x}, t) &= \nabla \cdot \int_{\Sigma} \boldsymbol{n}\, \delta^2(\boldsymbol{x} - \boldsymbol{X})\, dl. \end{aligned} \tag{98}$$

Thus, the indicator function can be obtained by solving Poisson equation with a singular source term [42].

By introducing the indicator function, one can rewrite the bulk concentration equation (92) in Ω_1 with the absorption and desorption on the interface described in Eq. (93) into one equation in the whole domain Ω as

$$\frac{\partial}{\partial t}(H\,C)+\nabla\cdot(\boldsymbol{u}\,H\,C)=\frac{1}{Pe}\nabla\cdot(H\nabla C)-\int_{\Sigma}(S_aC_s(1-\Gamma)-S_d\lambda\Gamma)\delta^2(\boldsymbol{x}-\boldsymbol{X})dl. \tag{99}$$

Here, we rewrite the convection term in a divergence form since the velocity is incompressible. Notice that, in the domain Ω_1 where the indicator function $H=1$ so the above equation recovers to the original bulk surfactant equation (92). Moreover, since $H=0$ in the domain Ω_0, we have $HC=0$ no matter what are the values of C which restricts that the surfactant is insoluble in Ω_0. One should mention that the above bulk concentration equation (99) has the similar form as the diffuse-interface approach proposed by Teigen et. al. [40] except the expression of last term.

By taking the integration of Eq. (99) over the domain Ω, we have

$$\begin{aligned}
\frac{d}{dt}\int_{\Omega} HC d\boldsymbol{x} &= \int_{\Omega}\frac{\partial}{\partial t}(HC)d\boldsymbol{x}\\
&= -\int_{\Omega}\nabla\cdot(\boldsymbol{u}H\,C)d\boldsymbol{x}+\int_{\Omega}\frac{1}{Pe}\nabla\cdot(H\nabla C)d\boldsymbol{x}\\
&\quad -\int_{\Omega}\int_{\Sigma}(S_aC_s(1-\Gamma)-S_d\lambda\Gamma)\delta^2(\boldsymbol{x}-\boldsymbol{X})dld\boldsymbol{x}\\
&= -\int_{\Sigma}(S_aC_s(1-\Gamma)-S_d\lambda\Gamma)dl,
\end{aligned}$$

where the last equality is obtained by using the no flow velocity boundary condition $\boldsymbol{u}\cdot\boldsymbol{n}_1=0$, the zero surfactant flux $\frac{\partial C}{\partial \boldsymbol{n}_1}|_{\partial\Omega_1}=0$, and the integral identity of the Dirac delta function

$$\int_{\Omega}\delta^2(\boldsymbol{x}-\boldsymbol{X})d\boldsymbol{x}=1. \tag{100}$$

One can immediately see that the above rate of change of bulk surfactant mass in the domain Ω is exactly the same as the one in the domain Ω_1 as shown in Eq. (95). Based on our new formulation, the bulk surfactant adjacent to the interface can be simply evaluated as

$$C_s(\alpha,t)=\int_{\Omega}H\,C\delta^2(\boldsymbol{x}-\boldsymbol{X}(\alpha,t))d\boldsymbol{x}. \tag{101}$$

Chapter 7

A conservative scheme for solving the coupled surface-bulk concentration equations

In this chapter, we give the details of our numerical scheme to solve the coupled surface-bulk concentration equations (91) and (99). For simplicity, assume our computational domain to be a rectangular domain $\Omega = [a, b] \times [c, d]$. Within this domain, we use a uniform lattice grid with mesh width h and adapt the usual staggered grid structure [19] where the given velocity components u and v are defined at usual at $(x_{i-1/2}, y_j) = (a + (i-1)h, c + (j-1/2)h)$ and $(x_i, y_{j-1/2}) = (a + (i-1/2)h, c + (j-1)h)$, respectively.

However, the bulk surfactant concentration $C_{i,j}$ and the discrete indicator function $H_{i,j}$, are both defined at the cell center labelled as $\boldsymbol{x} = (x_i, y_j) = (a + (i-1/2)h, c + (j-1/2)h)$. For the immersed interface, we use a collection of discrete points $\alpha_k = k\Delta\alpha, k = 0, 1, \ldots M$ such that the Lagrangian markers are denoted by $\boldsymbol{X}_k = \boldsymbol{X}(\alpha_k) = (X_k, Y_k)$. The unit tangent vector $\boldsymbol{\tau}_k$ and the discrete stretching factor $|D_\alpha \boldsymbol{X}_k|$ are defined at the "half-integer" points $\alpha_{k+1/2} = (k + 1/2)\Delta\alpha$, where the unit tangent can be approximated by

$$\boldsymbol{\tau}_k = D_\alpha \boldsymbol{X}_k / |D_\alpha \boldsymbol{X}_k| = \frac{\boldsymbol{X}_{k+1} - \boldsymbol{X}_k}{\Delta\alpha} \Big/ \left| \frac{\boldsymbol{X}_{k+1} - \boldsymbol{X}_k}{\Delta\alpha} \right|. \tag{102}$$

Once we have defined the unit tangent vector on the interface, the unit outward normal

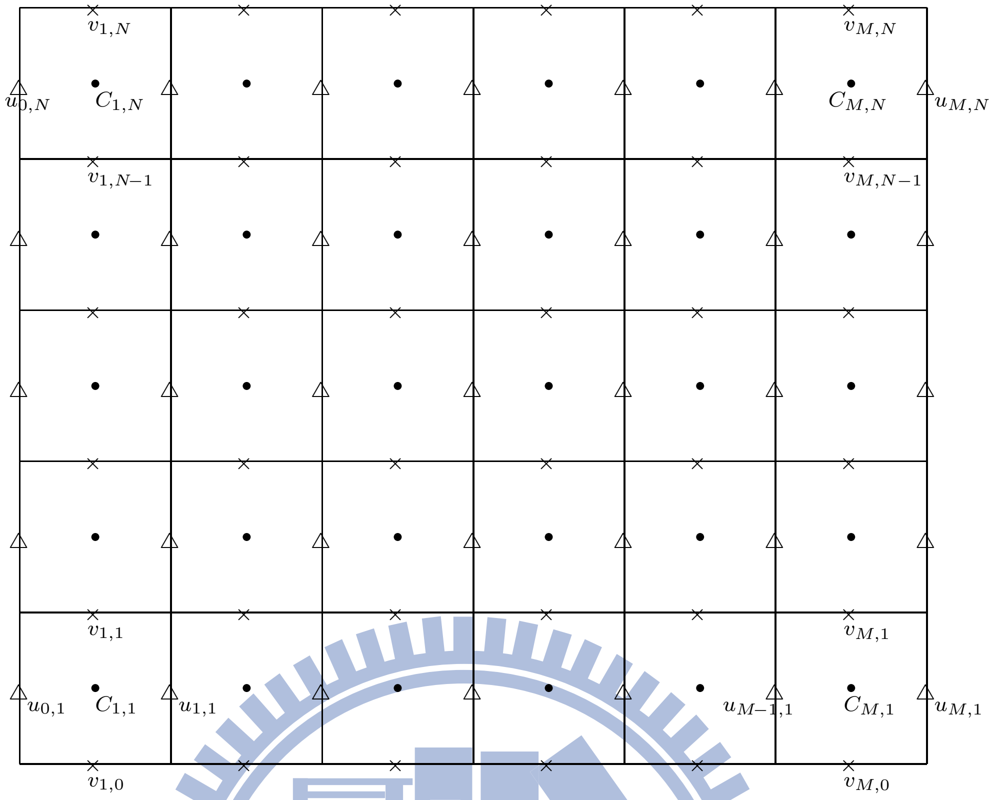

Figure 7.1: The computational domain Ω using staggered grid with mesh size h.

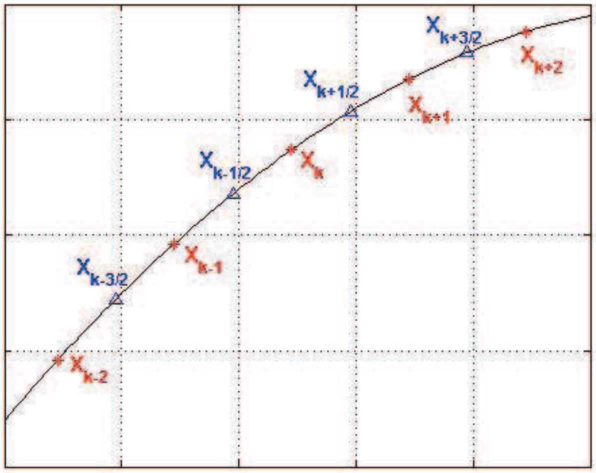

Figure 7.2: Illustration of Lagrangian markers.

vector $\boldsymbol{n}_k$ can be calculated straightforwardly, i.e. $\boldsymbol{n}_k = (n_{k_1}, n_{k_2}) = (\tau_{k_2}, -\tau_{k_1})$ where $\boldsymbol{\tau}_k = (\tau_{k_1}, \tau_{k_2})$ The surface concentration Γ_k is also defined at the "half-integer" points.

Let Δt be the time step size, and n be the superscript time step index. At the beginning of each time step, e.g., step n, the variables $\boldsymbol{X}^n, \Gamma^n$ and C^n are all given.

Step 1: Compute the new interface position. Since the velocity field $\boldsymbol{u}$ is given through the computation, the first step is to get the velocity on the marker points and to move the marker points to new positions. The velocity on the Lagrangian markers can be interpolated from the new velocity at the fluid lattice points surrounding the marker points, i.e.

$$\begin{aligned} \boldsymbol{U}_k^{n+1} &= \sum_{i,j} \boldsymbol{u}_{i,j}^{n+1} \delta_h^2(\boldsymbol{x}_{i,j} - \boldsymbol{X}_k^n) h^2 \\ \boldsymbol{X}_k^{n+1} &= \boldsymbol{X}_k^n + \Delta t \boldsymbol{U}_k^{n+1}, \end{aligned} \tag{103}$$

where δ_h^2 is a two-dimensional discrete delta function used in the immersed boundary method such as the one we use in previous part, which can be found in [32, 44].

Step 2: Compute the indicator function. Based on the new interface position $\boldsymbol{X}_k^{n+1}$ calculated in previous step, we can compute the corresponding indicator function H^{n+1} by numerically solving Eq. (98) as

$$\nabla_h^2 H_{i,j}^{n+1} = \nabla_h \cdot \left(\sum_k \boldsymbol{n}_k^{n+1} \, \delta_h^2(\boldsymbol{x}_{i,j} - \boldsymbol{X}_{k+1/2}^{n+1}) \left| D_\alpha \boldsymbol{X}_k^{n+1} \right| \Delta\alpha \right), \tag{104}$$

where $\boldsymbol{X}_{k+1/2}^{n+1} = (\boldsymbol{X}_{k+1}^{n+1} + \boldsymbol{X}_k^{n+1})/2$. We use the general five-point stencil discretization to approximate the Laplacian, i.e.

$$\nabla_h^2 H_{i,j}^{n+1} = \frac{H_{i+1,j}^{n+1} + H_{i,j+1}^{n+1} - 4H_{i,j}^{n+1} + H_{i-1,j}^{n+1} + H_{i,j-1}^{n+1}}{h^2} \tag{105}$$

Fast direct solvers to the Poisson problems can be found in the popular software package FISHPACK [3], We just use the subroutines in FISHPACK to solve the above discrete Poisson equation efficiently. The detailed accuracy issue about solving Eq. (104) can be found in previous part.

Step 3: Compute the surface concentration. As the same procedures written in [24], by multiply the interface stretching factor to Eq. (91), we rewrite the equation in terms of the material coordinate explicitly to obtain

$$\frac{\partial \Gamma}{\partial t}\left|\frac{\partial \boldsymbol{X}}{\partial \alpha}\right| + (\nabla_s \cdot \boldsymbol{u})\left|\frac{\partial \boldsymbol{X}}{\partial \alpha}\right| \Gamma = \frac{1}{Pe_s}\frac{\partial}{\partial \alpha}\left(\frac{\partial \Gamma}{\partial \alpha} \Big/ \left|\frac{\partial \boldsymbol{X}}{\partial \alpha}\right|\right) + q_s\left|\frac{\partial \boldsymbol{X}}{\partial \alpha}\right|$$

where $q_s = (S_a/\lambda)C_s(1-\Gamma) - S_d\Gamma$ represents the flux between surface and bulk concentration. Using the identity of $\frac{\partial}{\partial t}\left|\frac{\partial \boldsymbol{X}}{\partial \alpha}\right| = (\nabla_s \cdot \boldsymbol{u})\left|\frac{\partial \boldsymbol{X}}{\partial \alpha}\right|$, the above equation becomes

$$\frac{\partial \Gamma}{\partial t}\left|\frac{\partial \boldsymbol{X}}{\partial \alpha}\right| + \frac{\partial}{\partial t}\left|\frac{\partial \boldsymbol{X}}{\partial \alpha}\right| \Gamma = \frac{1}{Pe_s}\frac{\partial}{\partial \alpha}\left(\frac{\partial \Gamma}{\partial \alpha} \Big/ \left|\frac{\partial \boldsymbol{X}}{\partial \alpha}\right|\right) + q_s\left|\frac{\partial \boldsymbol{X}}{\partial \alpha}\right| \tag{106}$$

We then discretize the above equation by the following Crank-Nicholson scheme.

$$\begin{aligned}
&\frac{\Gamma_k^{n+1}-\Gamma_k^n}{\Delta t}\,\frac{\left|D_\alpha \boldsymbol{X}_k^{n+1}\right| + \left|D_\alpha \boldsymbol{X}_k^n\right|}{2} + \frac{\left|D_\alpha \boldsymbol{X}_k^{n+1}\right| - \left|D_\alpha \boldsymbol{X}_k^n\right|}{\Delta t}\,\frac{\Gamma_k^{n+1}+\Gamma_k^n}{2} \qquad (107)\\
&= \frac{1}{2\,Pe_s}\,\frac{1}{\Delta\alpha}\left(\frac{(\Gamma_{k+1}^{n+1}-\Gamma_k^{n+1})/\Delta\alpha}{(\left|D_\alpha \boldsymbol{X}_{k+1}^{n+1}\right| + \left|D_\alpha \boldsymbol{X}_k^{n+1}\right|)/2} - \frac{(\Gamma_k^{n+1}-\Gamma_{k-1}^{n+1})/\Delta\alpha}{(\left|D_\alpha \boldsymbol{X}_k^{n+1}\right| + \left|D_\alpha \boldsymbol{X}_{k-1}^{n+1}\right|)/2}\right)\\
&+\frac{1}{2\,Pe_s}\,\frac{1}{\Delta\alpha}\left(\frac{(\Gamma_{k+1}^{n}-\Gamma_k^{n})/\Delta\alpha}{(\left|D_\alpha \boldsymbol{X}_{k+1}^{n}\right| + \left|D_\alpha \boldsymbol{X}_k^{n}\right|)/2} - \frac{(\Gamma_k^{n}-\Gamma_{k-1}^{n})/\Delta\alpha}{(\left|D_\alpha \boldsymbol{X}_k^{n}\right| + \left|D_\alpha \boldsymbol{X}_{k-1}^{n}\right|)/2}\right)\\
&+\frac{((S_a/\lambda)C_k^*(1-\Gamma_k^{n+1}) - S_d\Gamma_k^{n+1})\left|D_\alpha \boldsymbol{X}_k^{n+1}\right| + ((S_a/\lambda)C_k^n(1-\Gamma_k^n) - S_d\Gamma_k^n)\left|D_\alpha \boldsymbol{X}_k^n\right|}{2}.
\end{aligned}$$

The adjacent bulk concentration C_k^* and C_k^n in last term can be obtained through Eq. (101) as

$$\begin{aligned}
C_k^* &= \sum_{i,j} H_{i,j}^{n+1} C_{i,j}^n \delta_h^2(\boldsymbol{x}_{i,j} - \boldsymbol{X}_{k+1/2}^{n+1})h^2\\
C_k^n &= \sum_{i,j} H_{i,j}^{n} C_{ij}^n \delta_h^2(\boldsymbol{x}_{i,j} - \boldsymbol{X}_{k+1/2}^{n})h^2,
\end{aligned} \tag{108}$$

where $\boldsymbol{X}_{k+1/2}^{n+1} = (\boldsymbol{X}_{k+1}^{n+1} + \boldsymbol{X}_k^{n+1})/2$ since the surface concentration is defined at the "half integer" material coordinate $\alpha_{k+1/2}$. Since the new interface marker location $\boldsymbol{X}_k^{n+1}$ and the corresponding indicator function H^{n+1} are both obtained in previous steps, the above discretization results in a symmetric tri-diagonal linear system which can be solved easily. For instance, we can use the tri-diagonal matrix algorithm, also known as the Thomas algorithm. One should notice that if the Lagrangian markers are required to be equally distributed for some applications, the above surface concentration equation (106) and its numerical scheme (107) can be modified accordingly. The detail of an equi-distributed technique for Lagrangian markers, which is related to adding an artificial tangential velocity, can be found in our recent work [25].

Step 4: Compute the bulk concentration. The last step is to update the bulk concentration C. We discretize the bulk concentration equation (99) by the following Crank-Nicholson scheme

$$\begin{aligned} & \frac{(HC)^{n+1}_{i,j}-(HC)^{n}_{i,j}}{\Delta t}+\nabla_h\cdot(\frac{(\mathbf{u}HC)^{n+1}_{i,j}+(\mathbf{u}HC)^{n}_{i,j}}{2}) \\ = \; & \frac{1}{Pe}(\frac{\nabla_h\cdot(H\nabla_h C)^{n+1}_{i,j}+\nabla_h\cdot(H\nabla_h C)^{n}_{i,j}}{2})-Q_{i,j} \end{aligned} \tag{109}$$

where $Q_{i,j}$ is the discrete version of the singular integral in Eq. (99) as

$$\begin{aligned} Q_{i,j} &= \frac{1}{2}\sum_k (S_a C^*_k(1-\Gamma^{n+1}_k)-S_d\lambda\Gamma^{n+1}_k)\left|D_\alpha \mathbf{X}^{n+1}_k\right|\,\delta^2_h(\boldsymbol{x}_{i,j}-\boldsymbol{X}^{n+1}_{k+1/2})\,\Delta\alpha \\ &+ \frac{1}{2}\sum_k (S_a C^n_k(1-\Gamma^{n}_k)-S_d\lambda\Gamma^{n}_k)\left|D_\alpha \mathbf{X}^{n}_k\right|\,\delta^2_h(\boldsymbol{x}_{i,j}-\boldsymbol{X}^{n}_{k+1/2})\,\Delta\alpha. \end{aligned} \tag{110}$$

The difference operator $\nabla_h=(D^x_h,D^y_h)$ is the regular centered difference approximation on the staggered grid to the gradient operator.

$$\begin{aligned} D^x_h(uHC)_{i,j} &= \frac{u_{i+1/2,j}H_{i+1/2,j}C_{i+1/2,j}-u_{i-1/2,j}H_{i-1/2,j}C_{i-1/2,j}}{h}, \\ D^y_h(vHC)_{i,j} &= \frac{v_{i,j+1/2}H_{i,j+1/2}C_{i,j+1/2}-v_{i,j-1/2}H_{i,j-1/2}C_{i,j-1/2}}{h}, \\ D^x_h(HD^x_hC)_{i,j} &= \frac{H_{i+1/2,j}(C_{i+1,j}-C_{i,j})/h-H_{i-1/2,j}(C_{i,j}-C_{i-1,j})/h}{h}, \\ D^y_h(HD^y_hC)_{i,j} &= \frac{H_{i,j+1/2}(C_{i,j+1}-C_{i,j})/h-H_{i,j-1/2}(C_{i,j}-C_{i,j-1})/h}{h}, \end{aligned} \tag{111}$$

where the approximate values defined at the cell edges are evaluated as the average of two neighboring values. For instance,

$$\begin{aligned} H_{i+1/2,j} &= (H_{i+1,j}+H_{i,j})/2 \\ H_{i-1/2,j} &= (H_{i,j}+H_{i-1,j})/2 \\ H_{i,j+1/2} &= (H_{i,j+1}+H_{i,j})/2 \\ H_{i,j-1/2} &= (H_{i,j}+H_{i,j-1})/2. \end{aligned} \tag{112}$$

The same manner can be applied to the bulk concentration terms, such as $C_{i+1/2,j}$.

One should notice that, since $H=0$ in Ω_0, to avoid the division by zero in above scheme causing singularities in the linear systems, we regularize the indicator function H

by using $\sqrt{H^2+\epsilon^2}$ instead of H itself where ϵ is chosen about 10^{-6}. This regularization is commonly adopted in literature such as in [40].

Furthermore, we need to check if our proposed method is preserving the mass conservation of surfactant. First we take the summation of Eq. (107) over the interface. The periodicity of the quantities are provided due to the fact that the interface is a simple closed curve. It leads to the following discrete rate of change of surface concentration

$$\begin{aligned}&\frac{\lambda}{\Delta t}\left(\sum_k \Gamma_k^{n+1}\left|D_\alpha \boldsymbol{X}_k^{n+1}\right|\Delta\alpha-\sum_k \Gamma_k^{n}\left|D_\alpha \boldsymbol{X}_k^{n}\right|\Delta\alpha\right)\\ =&\sum_k \frac{\left(S_a C_k^*(1-\Gamma_k^{n+1})-S_d\lambda\Gamma_k^{n+1}\right)\left|D_\alpha \boldsymbol{X}_k^{n+1}\right|+\left(S_a C_k^n(1-\Gamma_k^{n})-S_d\lambda\Gamma_k^{n}\right)\left|D_\alpha \boldsymbol{X}_k^{n}\right|}{2}\Delta\alpha\end{aligned}$$

Similarly, we take the summation of Eq. (109) over the whole computational domain, then apply the no-outgoing flow boundary conditions for velocity and no-flux boundary conditions for bulk concentration, i.e. $(\boldsymbol{u}\cdot\boldsymbol{n}_1=0, \nabla_h C\cdot\boldsymbol{n}_1=0 \text{ on } \partial\Omega)$. Thus we obtain

$$\begin{aligned}&\frac{1}{\Delta t}\left(\sum_{ij}(HC)_{ij}^{n+1}h^2-\sum_{ij}(HC)_{ij}^{n}h^2\right)\\ =&-\sum_k \frac{\left(S_a C_k^*(1-\Gamma_k^{n+1})-S_d\lambda\Gamma_k^{n+1}\right)\left|D_\alpha \boldsymbol{X}_k^{n+1}\right|+\left(S_a C_k^n(1-\Gamma_k^{n})-S_d\lambda\Gamma_k^{n}\right)\left|D_\alpha \boldsymbol{X}_k^{n}\right|}{2}\Delta\alpha\end{aligned}$$

where we use the discrete analogue of the delta function integral identity (zero moment condition)

$$\sum_{ij}\delta_h^2(\boldsymbol{x}_{ij}-\boldsymbol{X}_{k+1/2})h^2=1. \tag{113}$$

By combining the above two summations, we have proved the following discrete conservation for the total surfactant mass as

$$\sum_{ij}(HC)_{ij}^{n+1}h^2+\lambda\sum_k\Gamma_k^{n+1}\left|D_\alpha\boldsymbol{X}_k^{n+1}\right|\Delta\alpha=\sum_{ij}(HC)_{ij}^{n}h^2+\lambda\sum_k\Gamma_k^{n}\left|D_\alpha\boldsymbol{X}_k^{n}\right|\Delta\alpha. \tag{114}$$

Chapter 8

Navier-Stokes flow with soluble surfactant

Consider an incompressible flow problem consisting of two-phase fluids in a fixed two-dimensional square domain $\Omega = \Omega_0 \cup \Omega_1$ where an interface Σ separates Ω_0 from Ω_1 as illustrated in Figure 1. As in previous section, it is assumed that the surfactant exists on the interface as a monolayer and is adsorbed from or desorbed to the bulk fluid in Ω_1; that is, the surfactant is soluble in the exterior bulk but not in the interior one. The interface is contaminated by the surfactant so that the distribution of the surfactant changes the surface tension accordingly. In order to formulate the problem using the immersed boundary approach, we simply treat the interface as an immersed boundary that exerts force to the fluids and moves with local fluid velocity. For simplicity, we assume equal viscosity and density for both fluids, and neglect the gravity. Certainly, the present Navier-Stokes solver can be replaced by the one with different density and viscosity ratios.

As in [24], the non-dimensional Navier-Stokes flow in the usual immersed boundary formulation can be written as

$$
\begin{aligned}
\frac{\partial \boldsymbol{u}}{\partial t} + (\boldsymbol{u}\cdot\nabla)\boldsymbol{u} + \nabla p &= \frac{1}{Re}\,\nabla^2 \boldsymbol{u} + \frac{\boldsymbol{f}}{Re\ Ca}, && (115)\\
\nabla\cdot\boldsymbol{u} &= 0, && (116)\\
\boldsymbol{f}(\boldsymbol{x},t) &= \int_\Sigma \boldsymbol{F}(\alpha,t)\,\delta(\boldsymbol{x}-\boldsymbol{X}(\alpha,t))\,d\alpha, && (117)\\
\frac{\partial \boldsymbol{X}(\alpha,t)}{\partial t} = \boldsymbol{U}(\alpha,t) &= \int_\Omega \boldsymbol{u}(\boldsymbol{x},t)\,\delta(\boldsymbol{x}-\boldsymbol{X}(\alpha,t))d\boldsymbol{x}, && (118)\\
\boldsymbol{F}(\alpha,t) &= \frac{\partial}{\partial\alpha}(\sigma(\alpha,t)\boldsymbol{\tau}(\alpha,t)), && (119)
\end{aligned}
$$

where $\boldsymbol{u}$ is the fluid velocity and p is the pressure. The dimensionless numbers are the Reynolds number ($Re = \rho U_\infty R/\mu$) describing the ratio between the inertial force and the viscous force, and the Capillary number ($Ca = \mu U_\infty/\sigma_\infty$) describing the strength of the surface tension. The presence of surfactant will reduce the surface tension of the interface by the Langmuir equation of state [34]

$$\sigma = 1 + El\ln(1-\Gamma), \qquad (120)$$

where σ is the surface tension, and El is the elasticity number measuring the sensitivity of the surface tension to the surfactant concentration. Since the surfactant is soluble in Ω_1, we need to solve the coupled surface-bulk concentration equations (91)-(93) to close the system.

8.1 Fluid solver for Navier-Stokes equations

In this section, we introduce our fluid solver which used in previous work [24]. Let $\boldsymbol{u}(\boldsymbol{x},t) = (u(\boldsymbol{x},t), v(\boldsymbol{x},t))$, $\boldsymbol{f}(\boldsymbol{x},t) = (f(\boldsymbol{x},t), g(\boldsymbol{x},t))$, and $p(\boldsymbol{x},t)$ be the fluid velocity, external forces and fluid pressure, respectively, where $\boldsymbol{x} = (x,y)$ is the Eulerian coordinates. We can write down the Navier-Stokes Equations (115) and (116) in explicit form

$$
\begin{aligned}
\frac{\partial u}{\partial t} + \frac{\partial u^2}{\partial x} + \frac{\partial uv}{\partial y} + \frac{\partial p}{\partial x} &= \frac{1}{Re}\left(\frac{\partial^2 u}{\partial x^2} + \frac{\partial^2 u}{\partial y^2}\right) + \frac{f}{ReCa} && (121)\\
\frac{\partial v}{\partial t} + \frac{\partial uv}{\partial x} + \frac{\partial v^2}{\partial y} + \frac{\partial p}{\partial y} &= \frac{1}{Re}\left(\frac{\partial^2 v}{\partial x^2} + \frac{\partial^2 v}{\partial y^2}\right) + \frac{g}{ReCa} && (122)\\
\frac{\partial u}{\partial x} + \frac{\partial v}{\partial y} &= 0 && (123)
\end{aligned}
$$

Note that we use the continuity equation (123) to express the convection term as a conservative form. That is,

$$\boldsymbol{u}\cdot\nabla\boldsymbol{u}=\begin{pmatrix} u\frac{\partial u}{\partial x}+v\frac{\partial u}{\partial y} \\ u\frac{\partial v}{\partial x}+v\frac{\partial v}{\partial y} \end{pmatrix}.$$

In x-direction we rewrite

$$\begin{aligned} & u\frac{\partial u}{\partial x}+v\frac{\partial u}{\partial y} \\ = & u\frac{\partial u}{\partial x}+v\frac{\partial u}{\partial y}+u(\frac{\partial u}{\partial x}+\frac{\partial v}{\partial y}) \\ = & \frac{\partial u^2}{\partial x}+\frac{\partial uv}{\partial y}. \end{aligned} \tag{124}$$

Then similar procedure is applied in y-direction

$$\begin{aligned} & u\frac{\partial v}{\partial x}+v\frac{\partial v}{\partial y} \\ = & u\frac{\partial v}{\partial x}+v\frac{\partial v}{\partial y}+v(\frac{\partial u}{\partial x}+\frac{\partial v}{\partial y}) \\ = & \frac{\partial uv}{\partial x}+\frac{\partial v^2}{\partial y} \end{aligned} \tag{125}$$

In order to discretize (121) to (123), the following second-order accurate finite-difference expressions for derivatives with respect to space for (i,j)-cell are used [11]

$$\begin{aligned}
\left(\frac{\partial u^2}{\partial x}\right)_{i+1/2,j} &= \frac{(u_{i+1,j})^2-(u_{i,j})^2}{\Delta x}, \\
\left(\frac{\partial uv}{\partial y}\right)_{i+1/2,j} &= \frac{(uv)_{i+1/2,j+1/2}-(uv)_{i+1/2,j-1/2}}{\Delta y}, \\
\left(\frac{\partial^2 u}{\partial x^2}\right)_{i+1/2,j} &= \frac{u_{i+3/2,j}-2u_{i+1/2,j}+u_{i-1/2,j}}{\Delta x^2}, \\
\left(\frac{\partial^2 u}{\partial y^2}\right)_{i+1/2,j} &= \frac{u_{i+1/2,j+1}-2u_{i+1/2,j}+u_{i+1/2,j-1}}{\Delta y^2}, \\
\left(\frac{\partial uv}{\partial x}\right)_{i,j+1/2} &= \frac{(uv)_{i+1/2,j+1/2}-(uv)_{i-1/2,j+1/2}}{\Delta x}, \\
\left(\frac{\partial v^2}{\partial y}\right)_{i,j+1/2} &= \frac{(v_{i,j+1})^2-(v_{i,j})^2}{\Delta y}, \\
\left(\frac{\partial^2 v}{\partial x^2}\right)_{i,j+1/2} &= \frac{v_{i+1,j+1/2}-2v_{i,j+1/2}+v_{i-1,j+1/2}}{\Delta x^2}, \\
\left(\frac{\partial^2 v}{\partial y^2}\right)_{i,j+1/2} &= \frac{v_{i,j+3/2}-2v_{i,j+1/2}+v_{i,j-1/2}}{\Delta y^2}.
\end{aligned} \tag{126}$$

In the above expression, terms like $u_{i,j}, v_{i,j}, u_{i+1/2,j+1/2}, v_{i+1/2,j+1/2}$ appear, which are not defined in Figure 7. To evaluate such terms, linear interpolation is employed, that is,

$$\begin{aligned} u_{i,j} &= \frac{u_{i+1/2,j} + u_{i-1/2,j}}{2}, \\ u_{i+1/2,j+1/2} &= \frac{u_{i+1/2,j+1} + u_{i+1/2,j}}{2}, \\ v_{i,j} &= \frac{v_{i,j+1/2} + v_{i,j-1/2}}{2}, \\ v_{i+1/2,j+1/2} &= \frac{v_{i+1,j+1/2} + u_{i,j+1/2}}{2}. \end{aligned} \tag{127}$$

We adapt Crank-Nicholson scheme to the projection method proposed by Chorin [10], which is a modification to the Marker and Cell (MAC) method proposed by Amsden and Harlow [19] where the method is characterized by the use of a staggered grid. The general procedure for a projection method is a prediction-correction approach. In the first step we use the momentum equations to compute an intermediate velocity field denoted by $\boldsymbol{u}^\star$. This velocity does not satisfy the continuity equation. In the second step we solve a Poisson equation for the pressure which is derived from the continuity equation. Finally, we project the solution $\boldsymbol{u}^\star$ to the real divergence-free velocity field by the computed pressure.

We write down the semi-discretization of momentum equations (121)

$$\begin{aligned} &\frac{u^{n+1}_{i+1/2,j} - u^{n}_{i+1/2,j}}{\Delta t} + \left(\frac{\partial u^2}{\partial x}\right)^{n+1/2}_{i+1/2,j} + \left(\frac{\partial uv}{\partial y}\right)^{n+1/2}_{i+1/2,j} + \frac{p^{n+1/2}_{i+1,j} - p^{n+1/2}_{i,j}}{\Delta x} \\ = \; &\frac{1}{Re}\left\{\left(\frac{\partial^2 u}{\partial x^2}\right)^{n+1/2}_{i+1/2,j} + \left(\frac{\partial^2 u}{\partial y^2}\right)^{n+1/2}_{i+1/2,j}\right\} + \frac{f^{n+1/2}_{i+1/2,j}}{ReCa}, \\ &\frac{v^{n+1}_{i,j+1/2} - v^{n}_{i,j+1/2}}{\Delta t} + \left(\frac{\partial uv}{\partial x}\right)^{n+1/2}_{i,j+1/2} + \left(\frac{\partial v^2}{\partial y}\right)^{n+1/2}_{i,j+1/2} + \frac{p^{n+1/2}_{i,j+1} - p^{n+1/2}_{i,j}}{\Delta y} \\ = \; &\frac{1}{Re}\left\{\left(\frac{\partial^2 v}{\partial x^2}\right)^{n+1/2}_{i,j+1/2} + \left(\frac{\partial^2 v}{\partial y^2}\right)^{n+1/2}_{i,j+1/2}\right\} + \frac{g^{n+1/2}_{i,j+1/2}}{ReCa}. \end{aligned} \tag{128}$$

In order to reduce the complexity of computation, we use Adams-Bashforth scheme to approximate the convection terms

$$
\begin{aligned}
\left(\frac{\partial u^2}{\partial x}\right)^{n+1/2}_{i+1/2,j}+\left(\frac{\partial uv}{\partial y}\right)^{n+1/2}_{i+1/2,j} &= \frac{3}{2}\left\{\left(\frac{\partial u^2}{\partial x}\right)^{n}_{i+1/2,j}+\left(\frac{\partial uv}{\partial y}\right)^{n}_{i+1/2,j}\right\}\\
&- \frac{1}{2}\left\{\left(\frac{\partial u^2}{\partial x}\right)^{n-1}_{i+1/2,j}+\left(\frac{\partial uv}{\partial y}\right)^{n-1}_{i+1/2,j}\right\},\\
\left(\frac{\partial uv}{\partial x}\right)^{n+1/2}_{i,j+1/2}+\left(\frac{\partial v^2}{\partial y}\right)^{n+1/2}_{i,j+1/2} &= \frac{3}{2}\left\{\left(\frac{\partial uv}{\partial x}\right)^{n}_{i,j+1/2}+\left(\frac{\partial v^2}{\partial y}\right)^{n}_{i,j+1/2}\right\}\\
&- \frac{1}{2}\left\{\left(\frac{\partial uv}{\partial x}\right)^{n-1}_{i,j+1/2}+\left(\frac{\partial v^2}{\partial y}\right)^{n-1}_{i,j+1/2}\right\}.
\end{aligned}
\tag{129}
$$

The external forcing terms f and g are substituted by $f^n_{i+1/2,j}$ and $g^n_{i,j+1/2}$, which are computed from the data in previous time step.

The first step is to find prediction solutions $\boldsymbol{u}^\star$ by using the pressure of previous time step

$$
\begin{aligned}
&\frac{u^\star_{i+1/2,j}}{\Delta t}-\frac{1}{2Re}\left\{\left(\frac{\partial^2 u}{\partial x^2}\right)^{\star}_{i+1/2,j}+\left(\frac{\partial^2 u}{\partial y^2}\right)^{\star}_{i+1/2,j}\right\}\\
=\;& \frac{u^n_{i+1/2,j}}{\Delta t}-\frac{p^{n-1/2}_{i+1,j}-p^{n-1/2}_{i,j}}{\Delta x}-\left(\frac{\partial u^2}{\partial x}\right)^{n+1/2}_{i+1/2,j}+\left(\frac{\partial uv}{\partial y}\right)^{n+1/2}_{i+1/2,j}\\
+\;& \frac{1}{2Re}\left\{\left(\frac{\partial^2 u}{\partial x^2}\right)^{n}_{i+1/2,j}+\left(\frac{\partial^2 u}{\partial y^2}\right)^{n}_{i+1/2,j}\right\}+\frac{f^n_{i+1/2,j}}{ReCa},\\
&\frac{v^\star_{i,j+1/2}}{\Delta t}-\frac{1}{2Re}\left\{\left(\frac{\partial^2 v}{\partial x^2}\right)^{\star}_{i,j+1/2}+\left(\frac{\partial^2 v}{\partial y^2}\right)^{\star}_{i,j+1/2}\right\}\\
=\;& \frac{u^n_{i+1/2,j}}{\Delta t}-\frac{p^{n-1/2}_{i,j+1}-p^{n-1/2}_{i,j}}{\Delta y}-\left(\frac{\partial uv}{\partial x}\right)^{n+1/2}_{i,j+1/2}+\left(\frac{\partial v^2}{\partial y}\right)^{n+1/2}_{i,j+1/2}\\
+\;& \frac{1}{2Re}\left\{\left(\frac{\partial^2 v}{\partial x^2}\right)^{n}_{i,j+1/2}+\left(\frac{\partial^2 v}{\partial y^2}\right)^{n}_{i,j+1/2}\right\}+\frac{g^n_{i,j+1/2}}{ReCa}.
\end{aligned}
\tag{130}
$$

These system of equations lead to solving two Helmholtz equations. one can use fast direct solvers such as FISHPACK to compute $u^\star$ and $v^\star$.

Compare with original semi-discretization (128), we have to solve

$$
\frac{\boldsymbol{u}^{n+1}-\boldsymbol{u}^\star}{\Delta t}=-\nabla_h(p^{n+1/2}-p^{n-1/2})+\frac{1}{2Re}\nabla^2_h(\boldsymbol{u}^{n+1}-\boldsymbol{u}^\star) \tag{131}
$$

Assume $\boldsymbol{u}^{n+1}$ is the final solution satisfying divergence-free condition. By using the Hodge decomposition, there exists a potential function ϕ such that

$$
\frac{\boldsymbol{u}^{n+1}-\boldsymbol{u}^\star}{\Delta t}=\nabla_h\phi. \tag{132}
$$

We take divergence on Eq. (132) and obtain

$$\frac{-\nabla_h \cdot \boldsymbol{u}^\star}{\Delta t} = \nabla_h^2 \phi, \tag{133}$$

which is a Poisson equation with zero Neumann boundary conditions.

By solving the Poisson equation for potential function ϕ, we can get the velocity field satisying the continuity equation by

$$\boldsymbol{u}^{n+1} = \boldsymbol{u}^\star + \Delta t \nabla_h \phi. \tag{134}$$

At the same time, the pressure is updated by

$$p^{n+1/2} = p^{n-1/2} + \phi - \frac{\nabla_h \cdot \boldsymbol{u}^\star}{2Re} \tag{135}$$

8.2 Algorithm for Navier-Stokes flow with soluble surfactant

In the following, we describe how to march one time step for the solutions. At the beginning of each time step, the interface position, the fluid velocity, the surface and bulk concentrations must be given. The numerical algorithm is as follows.

Step 1: Compute the surface tension and unit tangent on the interface.

$$\sigma_k^n = 1 + El \ln(1 - \Gamma_k^n), \tag{136}$$

$$\boldsymbol{\tau}_k^n = D_\alpha \boldsymbol{X}_k / \left| D_\alpha \boldsymbol{X}_k \right| \tag{137}$$

Note that both surface tension and unit tangent are defined on half integer points $\alpha_{k+1/2}$. Then the tension force is given by

$$\boldsymbol{F}_k^n = D_\alpha(\sigma_k^n \boldsymbol{\tau}_k^n) \tag{138}$$

Step 2: Distribute the interfacial force from the Lagrangian markers into the fluid.

$$\boldsymbol{f}^n(\boldsymbol{x}) = \sum_k \boldsymbol{F}_k^n \, \delta_h^2(\boldsymbol{x} - \mathbf{X}_k^n) \left| D_\alpha \boldsymbol{X}_k \right| \Delta\alpha. \tag{139}$$

Step 3: Solve the Navier-Stokes equations by the projection method.

By using the procedures stated in previous section, one need to solve the following system

$$\begin{aligned}
(\boldsymbol{u}\cdot\nabla_h)\boldsymbol{u}^{n+1/2} &= \frac{3}{2}(\boldsymbol{u}^n\cdot\nabla_h)\boldsymbol{u}^n - \frac{1}{2}(\boldsymbol{u}^{n-1}\cdot\nabla_h)\boldsymbol{u}^{n-1}\\
\frac{\boldsymbol{u}^*-\boldsymbol{u}^n}{\Delta t} &+ (\boldsymbol{u}\cdot\nabla_h)\boldsymbol{u}^{n+1/2} = -\nabla_h p^{n-1/2}\\
&\quad + \frac{1}{2Re}\nabla_h^2(\boldsymbol{u}^*+\boldsymbol{u}^n) + \frac{\boldsymbol{f}^n}{Re\,Ca}\\
\boldsymbol{u}^* &= \boldsymbol{u}_b, \qquad \text{on} \quad \partial\Omega\\
\nabla_h^2\phi^{n+1} &= \frac{\nabla_h\cdot\boldsymbol{u}^*}{\Delta t}, \qquad \frac{\partial\phi}{\partial n}=0, \quad \text{on} \quad \partial\Omega\\
\boldsymbol{u}^{n+1} &= \boldsymbol{u}^* - \Delta t\,\nabla_h\phi^{n+1},\\
p^{n+1/2} &= p^{n-1/2} + \phi^{n+1} - \frac{\nabla_h\cdot\boldsymbol{u}^*}{2\,Re}.
\end{aligned}$$

Basically, two Helmholtz equations and one Poisson equation are solved by FISHPACK at each time step.

Step 4: Compute the new interface position.

$$\begin{aligned}
\boldsymbol{U}_k^{n+1} &= \sum_{i,j}\boldsymbol{u}_{i,j}^{n+1}\delta_h^2(\boldsymbol{x}_{i,j}-\boldsymbol{X}_k^n)h^2\\
\boldsymbol{X}_k^{n+1} &= \boldsymbol{X}_k^n + \Delta t\boldsymbol{U}_k^{n+1},
\end{aligned} \tag{140}$$

Step 5: Compute the indicator function.

Step 6: Compute the surface concentration.

Step 7: Compute the bulk concentration.

The first four steps are the standard implementation in immersed boundary method. The last four steps are exactly the same four steps shown in previous chapter.

Chapter 9

Numerical results 2

In this chapter, in order to validate the numerical methods we proposed for solving surface-bulk coupled surfactant system, we try to do a series of tests to check if our solver is correct. Since the algorithms in our previous work [24] provided the conservation of surface concentration in numerical sense, here the numerical solution of bulk concentration is our main focus, and we also concern about the conservation of concentration when bulk part is coupling with the surface part. Throughout this chapter, the dimensionless adsorption depth λ is chosen to be 1, which refers approximately to a drop of micron in glycerol/water solutions of the polyethoxylate surfactant $C_{12}E_6$ [33]. We set the computational domain Ω as $[-1,1]\times[-1,1]$; unless stated otherwise.

9.1 Bulk diffusion with a fixed interface

For the first example, we test the diffusion of bulk surfactant in the exterior phase Ω_1. We fix the inner boundary of Ω_1, or the interface, and choose it as a circle centered at $(x_0, y_0) = (0,0)$ with radius $r_0 = 0.3$. In order to consider the diffusion of the bulk concentration only, the velocity is set to be zero, and the bulk-surface coupling is turned off, that is, we solve Eqs. (92)-(93) with $\boldsymbol{u} = 0$ and $S_a = S_d = 0$. The Peclet number is set as $Pe = 100$.

The initial bulk concentration is set as

$$C(x,y,0)=\begin{cases}0.5+0.4\cos(\pi x)\cos(\pi y) & \text{if } r>2.5r_0\\ \bar{C}+(0.4\cos(\pi x)\cos(\pi y)+0.5-\bar{C})w(r) & \text{if } r_0\le r\le 2.5r_0\\ 0 & \text{otherwise}\end{cases}\tag{141}$$

where the function

$$w(r)=\frac{1}{2}\left(1-\cos\left(\frac{(r-r_0)\pi}{1.5r_0}\right)\right)\tag{142}$$

with $r=\sqrt{(x-x_0)^2+(y-y_0)^2}$, and $\bar{C}$ is the concentration value at the interface. Here, $\bar{C}$ is set as the average value of the function $0.5+0.4\cos(\pi x)\cos(\pi y)$ along the interface $r=r_0$. Note that, by the choice of $w(r)$, one can immediately check that this initial condition satisfies the boundary condition Eq. (93) since $w(r_0)=w'(r_0)=0$.

We first present the convergence study of the proposed scheme. Here, the grid numbers $N\times N$ which we perform the computations vary from $N=64,128,256,512$ to $N=1024$ in the domain $\Omega=[-1,1]\times[-1,1]$ so the spatial mesh width is $h=2/N$. The Lagrangian marker width is chosen as $\Delta\alpha\approx h/2$ and the time step size is $\Delta t=h/8$. The solutions are computed at time $T=0.5$. Due to no analytic solutions in these simulations, we compute the error between two successive grids denoted by $\|(HC)_{2N}-(HC)_N\|$, so the rate of convergence can be computed as

$$rate=\log_2\frac{\|(HC)_N-(HC)_{N/2}\|}{\|(HC)_{2N}-(HC)_N\|}\tag{143}$$

Table 9.1 shows the mesh refinement analysis of the bulk concentration in L_2 and L_1 norms. The rate convergence is about first-order, which is a typical accuracy behavior using the immersed boundary method [32].

Figure 9.1 shows the bulk concentration along the horizontal line $y=0$ at different times using the grid number $N=256$. For Ω_0, the inner part of the domain, the bulk concentration is almost zero which reflects the insolubility of the inner region. Meanwhile, the surfactant in the outer region diffuses gradually as time evolves in these plots. To verify whether the total surfactant mass is conserved in the domain, we plot the relative error defined by $\frac{M_t-M_0}{M_0}$, where M_0 is the initial total surfactant mass while M_t is the total

$N \times N$	$\|(HC)_{2N} - (HC)_N\|_2$	rate	$\|(HC)_{2N} - (HC)_N\|_1$	rate
64×64	2.0344E-02	–	1.0424E-02	–
128×128	1.6218E-02	0.3270	4.7816E-03	1.1243
256×256	1.0940E-02	0.5679	2.4963E-03	0.9376
512×512	3.8809E-03	1.4951	2.9607E-04	3.0757

Table 9.1: The L_2 and L_1 errors and their convergent rates for the bulk diffusion with a fixed interface at $T = 0.5$.

mass computed at time t. The upper panel of Figure 9.2 shows the time evolutionary plot of the total mass relative error. The relative error is in the magnitude of 10^{-13}, which indicates that the present scheme has excellent conservation property.

Although in the plots of Figure 9.1, the bulk concentration is indistinct zero inside the interface; however, there is still an $O(\epsilon)$ amount of mass leaking into the region Ω_0. In the lower panel of Figure 9.2, we show the time evolutionary plot of the relative error for the leaking mass inside the interface. This relative error is defined as $\frac{M_L}{M_0}$, where the leaking mass M_L is computed by

$$M_L = \sum_{ij} (HC)_{ij} h^2 \text{ when } H_{ij} \leq 0.01. \tag{144}$$

Note that, the present relative error is within 10^{-5} which is only about 0.001%.

This mass leaking is caused by the regularization of the indicator function. In order to further understand the dependence of the regularization parameter ϵ on the effect of numerical leakage error, we test three different choice of $\epsilon = 10^{-6}, 0.1h$, and $0.1h^2$ as shown in Table 9.2. The errors are all computed up to time $T = 0.5$. One can see that all three cases show similar first-order convergence as the mesh is refined. Meanwhile, the errors of $\epsilon = 10^{-6}$ and $\epsilon = 0.1h^2$ are both comparable, and are better than the choice of $\epsilon = 0.1h$. Throughout the rest of computations, we therefore simply use $\epsilon = 10^{-6}$.

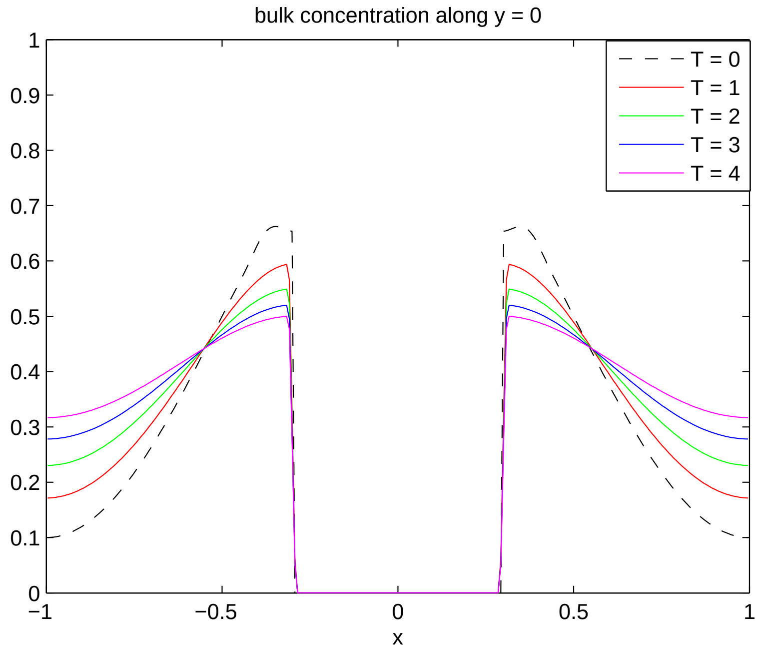

Figure 9.1: The bulk concentration along the horizontal line $y = 0$ at different times.

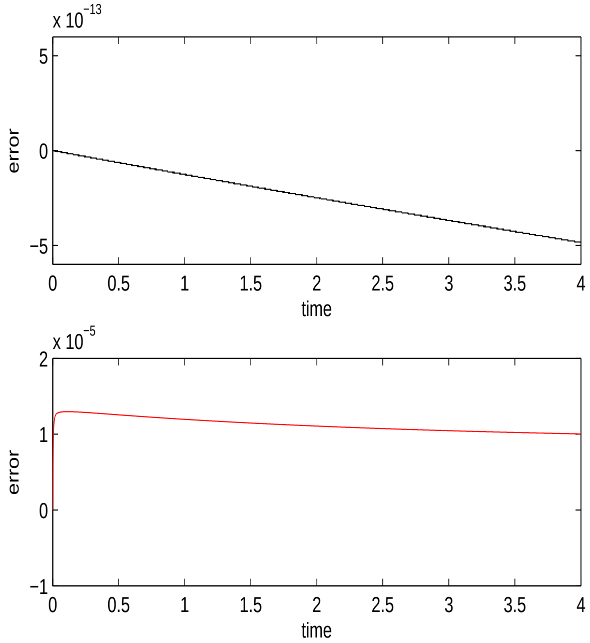

Figure 9.2: Upper panel: Time evolutionary plot of total mass relative error. Lower panel: Time evolutionary plot of leaking mass relative error inside the interface.

$N \times N$	$\epsilon = 10^{-6}$	rate	$\epsilon = 0.1h$	rate	$\epsilon = 0.1h^2$	rate
64×64	1.7175E-05	–	1.4376E-04	–	2.1261E-05	–
128×128	1.2707E-05	0.4346	8.1861E-05	0.8124	1.3810E-05	0.6225
256×256	7.0408E-06	0.8518	4.3141E-05	0.9241	7.3280E-06	0.9142
512×512	3.3182E-06	1.0853	2.1641E-05	0.9953	3.3904E-06	1.1119

Table 9.2: The convergent study of numerical leakage relative error $\frac{M_L}{M_0}$ at $T = 0.5$ for three different regularization parameter ϵ.

9.2 Bulk convection-diffusion with a moving interface

In the following test, we the same initial setup as the previous test but the convection effect is added into the equation. The flow and the interface are now moving with a prescribed incompressible velocity field $\boldsymbol{u} = (u, v)$ as

$$\begin{aligned} u &= -\frac{1}{2}(1 + \cos(\pi x))\sin(\pi y), \\ v &= \frac{1}{2}(1 + \cos(\pi y))\sin(\pi x). \end{aligned} \tag{145}$$

The center of the circular interface is shifted to the point of $(x_0, y_0) = (0.1, 0)$ initially so that the asymmetric flow can be developed.

Table 9.3 shows the convergent rate analysis of the bulk concentration in Ω as we refine the mesh. Again, one can see that the rate of convergence is first-order even with a moving interface.

Figure 9.4 shows the snapshots of the the bulk concentration at different times. The plots at left hand side are the contour plots of the concentration of bulk surfactant and the position of the interface in the same time. The figures at right hand side are the cross section of the concentration along the horizontal line $y = 0$. The asymmetric flow could be found among the plots, and the effects of both convection and diffusion are shown obviously on the distribution of bulk concentration. Figure 9.3 shows the relative errors

$N \times N$	$\|(HC)_{2N} - (HC)_N\|_2$	rate	$\|(HC)_{2N} - (HC)_N\|_1$	rate
64×64	2.3101E-02	–	1.1570E-02	–
128×128	1.5788E-02	0.5491	5.3424E-03	1.1149
256×256	1.1002E-02	0.5210	2.7364E-03	0.9652
512×512	3.9145E-03	1.4909	3.2451E-04	3.0759

Table 9.3: The L_2 and L_1 errors and their convergent rates for the bulk convection-diffusion with a moving interface at $T = 0.5$.

for total mass in Ω and leaking mass into Ω_0. Again, the total surfactant mass (upper panel) is conserved almost as well as the first test and the leaking mass error is still controlled within 0.002%. Note that, the oscillatory behavior of the latter error is due to the convection of the flow.

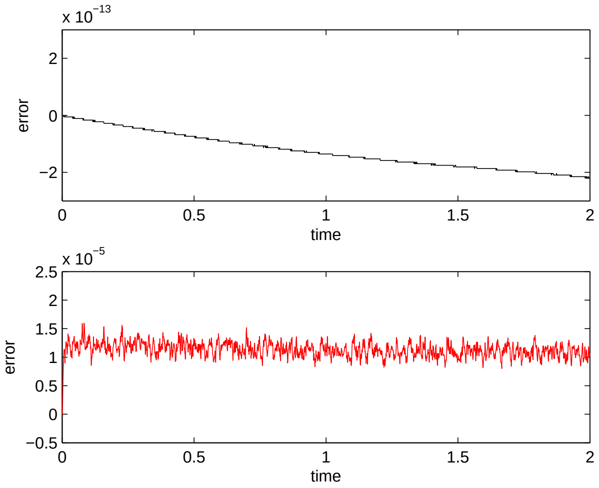

Figure 9.3: Upper panel: Time evolutionary plot of total mass relative error. Lower panel: Time evolutionary plot of leaking mass relative error inside the interface.

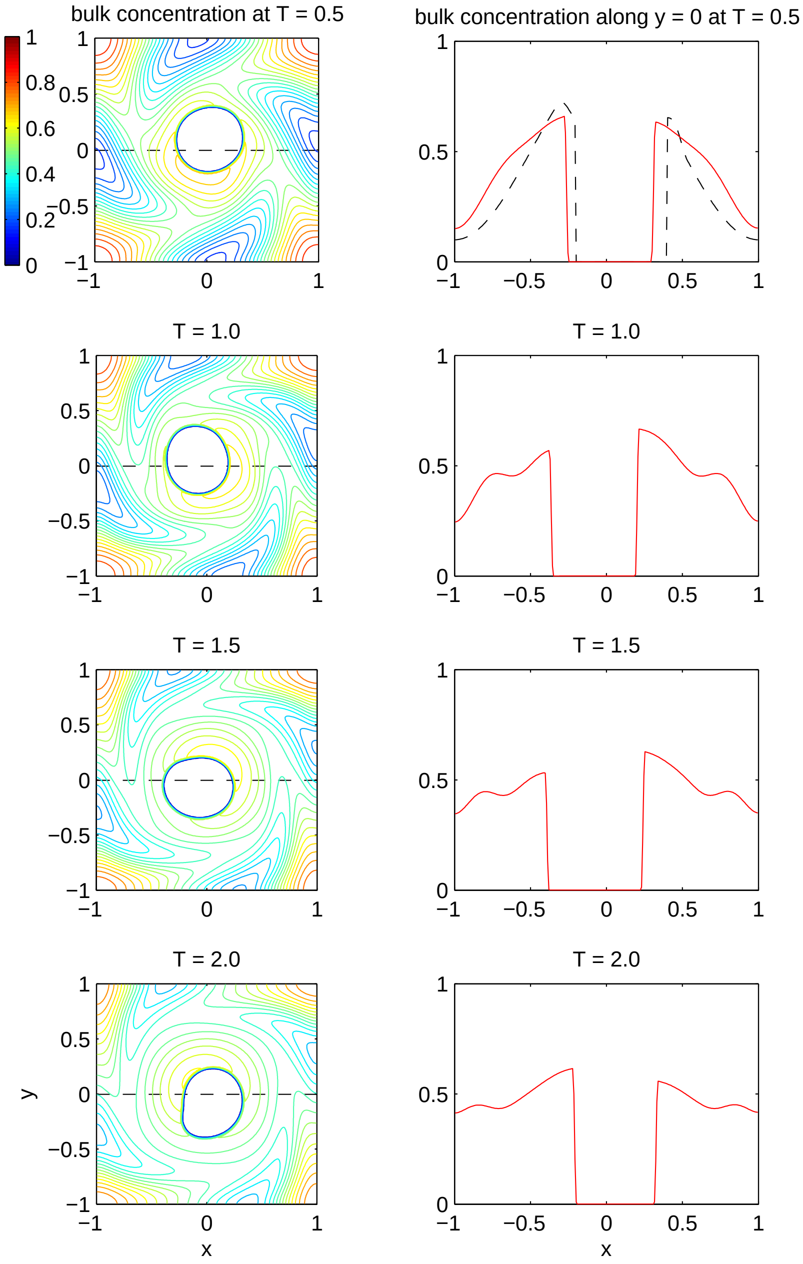

Figure 9.4: The bulk concentration at different times. Left column: The bulk concentration contour plots and the interface positions. Right column: The bulk concentration plots along the horizontal line $y = 0$. The dashed line in the first right plot denotes the initial bulk concentration along $y = 0$.

9.3 Surface-bulk coupling with a moving interface

In the third test, we take the surface-bulk coupling of the system with a moving interface into consideration; that is, we need to solve the coupling equations (91)-(93) with the prescribed velocity $\boldsymbol{u}$ defined in Eq. (146). The bulk Peclet number Pe and the surface Peclet number Pe_s are chosen as $Pe = Pe_s = 100$, and we set the adsorption and desorption Stanton numbers as $S_a = S_d = 1.0$. As previously, the initial interface is a circle with the center located at $(x_0, y_0) = (0.1, 0)$ and the radius $r_0 = 0.3$. The initial bulk concentration is defined as

$$C(x,y,0) = \begin{cases} 0.5(1-x^2)^2 & \text{if } r > 2.5r_0 \\ 0.5(1-x^2)^2 w(r) & \text{if } r_0 \le r \le 2.5r_0 \\ 0 & \text{otherwise} \end{cases}$$

where the function $w(r)$ is defined as same as Eq. (142). We also set the initial surface concentration to be identically zero (i.e. $\Gamma(\alpha, 0) = 0$) so that one can observe the significant surface absorption near the interface.

As before, by the choice of $w(r)$, the initial bulk and surface concentrations satisfy the boundary condition Eq. (93). Table 9.4 shows the mesh refinement analysis of the bulk and surface concentrations in L_2 norm. One can see that the rate of convergence is roughly first-order for the bulk while it is better than first-order for the surface concentration.

$N \times N$	$\|(HC)_{2N} - (HC)_N\|_2$	rate	$\|\Gamma_{2N} - \Gamma_N\|_2$	rate
64×64	1.9479E-03	–	1.9494E-04	–
128×128	8.5982E-04	1.1798	5.2554E-05	1.8911
256×256	4.3928E-04	0.9689	1.5999E-05	1.7158
512×512	1.2794E-04	1.7796	5.2204E-06	1.6157

Table 9.4: The L_2 errors and their convergent rates for the bulk and surface concentrations at $T = 0.5$.

Figure 9.6 shows the bulk concentration at different times. The upper panel shows the contour plots of bulk concentration and the instantaneous interface positions. The lower left column of the figure shows the plots of cross section of the bulk concentration along the horizontal line $y = 0$, while the lower right column shows the surface concentration along the interface. Since the total mass is conserved, the surface concentration increases while the bulk concentration decreases significantly due to the surface adsorption process. The relative errors for total mass in Ω and leaking mass into Ω_0 are shown in Figure 9.5. Again, the total surfactant mass is conserved as well as before and the leaking mass error is controlled within 0.0005%.

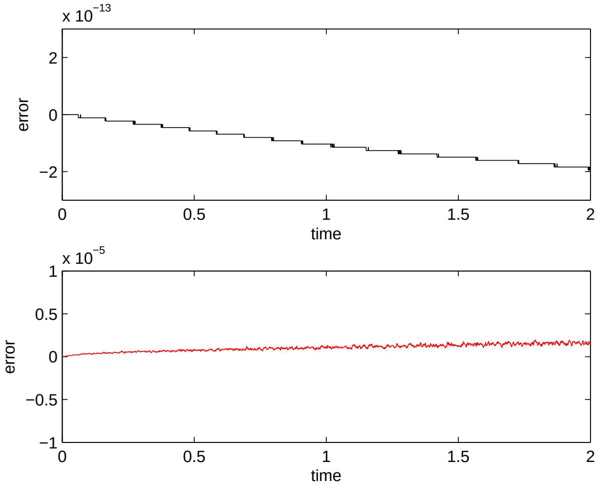

Figure 9.5: Upper panel: Time evolutionary plot of total mass relative error. Lower panel: Time evolutionary plot of leaking mass relative error inside the interface.

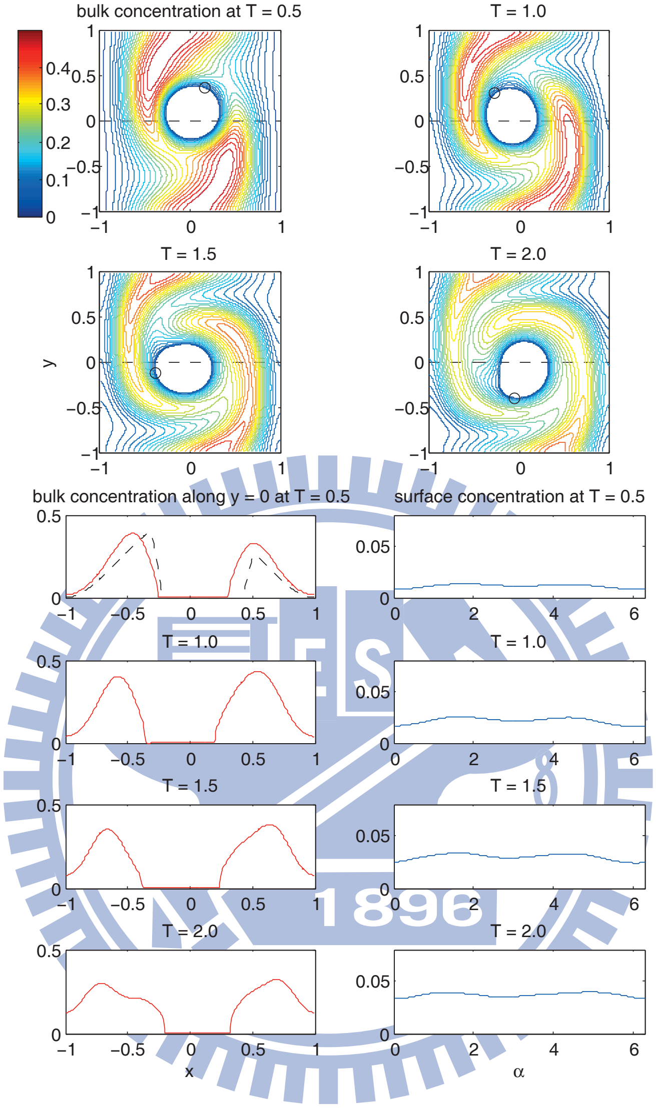

Figure 9.6: Upper panel: the bulk concentration contour plots and the interface positions. Lower left: the bulk concentration plots along the horizontal line $y = 0$. The dashed line in the first plot denotes the initial bulk concentration. Lower right: the surface concentration along the interface in counter-clockwise way starting from the point marked by ”o”.

9.4 A freely oscillating drop

In the following section, we consider a freely oscillating drop immersed in a quiescent flow as our first numerical test for Navier-Stokes flow with soluble surfactant. The initial drop interface is an ellipse centered at the origin with major and minor radius 0.6 and 0.15, respectively. That is, the initial interface configuration is defined as

$$\boldsymbol{X}(\alpha, 0) = (0.6\cos\alpha, 0.15\sin\alpha), 0 \leq \alpha \leq 2\pi \tag{146}$$

. Unlike the previous tests, we now set the initial bulk concentration in Ω_1 (outside of the ellipse) to be a constant $\bar{C}_s$, i.e. $C(x, y, 0) = \bar{C}_s$ in Ω_1. The bulk surfactant adjacent to the interface $C_s(\alpha)$ is naturally equal to C_s which leads to zero Neumann condition

$$\frac{\partial C}{\partial \boldsymbol{n}} = 0 \tag{147}$$

along the interface. We then choose the initial surface concentration $\Gamma(\alpha, 0)$ to be another constant $\bar{\Gamma}$ such that

$$\frac{S_a}{\lambda}\bar{C}_s(1 - \bar{\Gamma}) = S_d\bar{\Gamma}. \tag{148}$$

Based on the above choices of the initial bulk and surface concentrations, one can immediately see those initial conditions satisfy the boundary conditions in Eq (93). Since the flow is quiescent initially, the initial velocity of Navier-Stokes is zero everywhere and the no-slip boundary conditions are imposed on the computational boundary. The other parameters are set to be fixed as the bulk and surface Peclet numbers $Pe = Pe_s = 100$, the adsorption and desorption Stanton numbers $S_a = S_d = 1.0$, the Reynolds number $Re = 10$, the Capillary number $Ca = 2$, and the surfactant elasticity number $El = 0.5$, respectively.

As before, we first provides a convergence analysis of the present numerical scheme described in Chapter 8. Here, we perform four different computations with varying grid numbers $N = 64, 128, 256, 512$. The Lagrangian marker width is chosen as $\Delta\alpha \approx h/2$ and the time step size is $\Delta t = h/8$. The solutions are computed at time $T = 0.5$. Again, since the analytic solutions to these simulations are not available, we compute the L_2 error between two successive grids and the rate of convergence is computed as in previous examples. Table 9.5 shows the mesh refinement analysis of the bulk and surface concentration, and the velocity field at $T = 0.5$. One can see that the rate of convergence still behaves like first-order. The time evolutionary plots of relative errors for the total mass and the leaking mass inside the interface are similar to those in previous tests so we omit here.

$N \times N$	$\|(HC)_{2N} - (HC)_N\|_2$	rate	$\|\Gamma_{2N} - \Gamma_N\|_2$	rate
64×64	1.9723E-02	–	1.4433E-03	–
128×128	1.2555E-02	0.6516	4.7029E-04	1.6178
256×256	9.2176E-03	0.4457	1.9054E-04	1.3034

$N \times N$	$\|u_{2N} - u_N\|_2$	rate	$\|v_{2N} - v_N\|_2$	rate
64×64	4.3642E-03	–	4.0541E-03	–
128×128	1.2665E-03	1.7848	1.2908E-03	1.6511
256×256	4.0467E-04	1.6460	4.3488E-04	1.5695

Table 9.5: The L_2 errors and their convergent rates for the bulk and surface surfactant concentrations, and the fluid velocity field at $T = 0.5$.

We then make the comparison of a freely oscillating drop in a quiescent flow with a soluble or an insoluble surfactant. Note that, for the insoluble surfactant case, there is no surface-bulk coupling thus no need to solve the bulk concentration equation (92). Figure 9.8 shows the comparison between insoluble (denoted by dash-dotted line) and soluble (denoted by solid line) cases for a freely oscillating drop. The upper panel shows the interface positions at different times, while the lower left and right show the bulk concentration along $y = 0$ (soluble case only) and surface concentrations, respectively.

Due to the surface tension force, the drop tends to oscillate until it reaches to a stationary circular shape. For the soluble case, since the surface surfactant will be desorbed into the neighboring bulk region (see the lower left panel), the surface concentration is less than the one of the insoluble case (see the lower right panel). Therefore, the surface tension will not be reduced as much as in the insoluble case so the drop with soluble surfactant tends to oscillate faster than the insoluble case. Our numerical simulation confirms the above drop behaviors qualitatively.

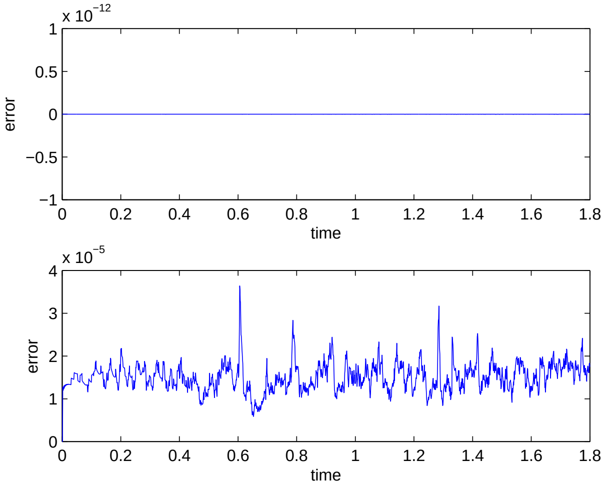

Figure 9.7: Upper panel: Time evolutionary plot of total mass relative error. Lower panel: Time evolutionary plot of leaking mass relative error inside the interface.

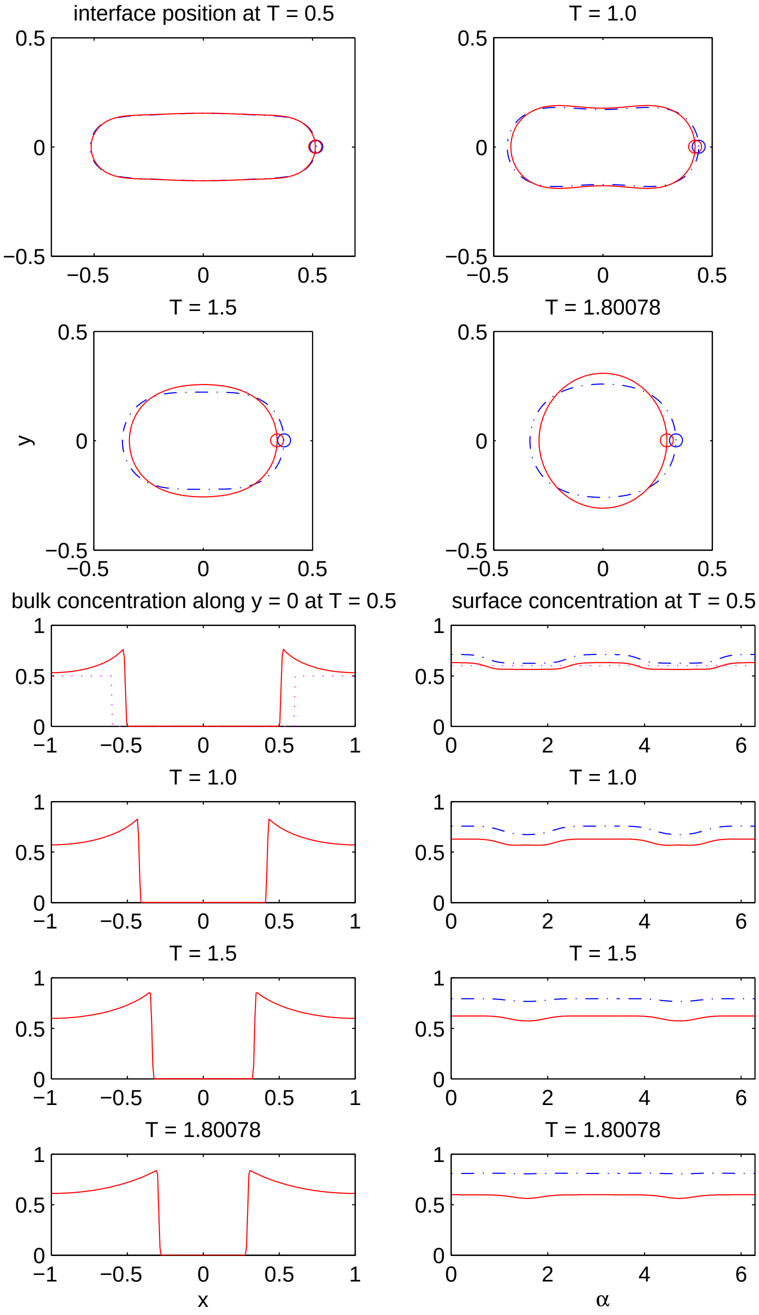

Figure 9.8: The comparison of insoluble (denoted by "-.") and soluble (denoted by "-") interfacial flows for a freely oscillating drop.

9.5 A drop under shear flow

In the last test, we consider a circular drop centered at the origin with radius $r_0 = 0.3$ is put initially in the domain $\Omega = [-1, 1] \times [-1, 1]$ under the shear flow. The initial and boundary conditions for the velocity used in this simulations are based on the setup of Tornberg et al. in [39]. That is, the velocity boundary conditions are

$$\begin{aligned} u = 1,\ v = 0 \qquad & \text{at } y = 1 \\ u = -1,\ v = 0 \qquad & \text{at } y = -1, \end{aligned} \tag{149}$$

respectively and u, v are both periodic at $x = \pm 1$. As also suggested in [39], we set the initial velocity as the quiescent flow to avoid unrealistic flow interior to the drop during the transition caused by using the linear velocity initially. That is, the flow is set to motion simply by the boundary shear. The boundary conditions for the bulk concentration equation are chosen as

$$\frac{\partial C}{\partial \boldsymbol{n}} = 0 \text{ at } y = \pm 1 \tag{150}$$

and are periodic at $x = \pm 1$ to be consistent with the flow conditions. Therefore, the total surfactant mass is still conserved in this case. The initial bulk concentration is defined as

$$C(x, y, 0) = \begin{cases} \sin^2(\pi x) & \text{if } r > 2.5 r_0 \\ \sin^2(\pi x) w(r) & \text{if } r_0 \leq r \leq 2.5 r_0 \\ 0 & \text{otherwise} \end{cases}$$

where the function $w(r)$ is defined as same as Eq. (142). We also set the initial surface concentration to be identically zero (i.e. $\Gamma(\alpha, 0) = 0$) so that significant surface absorption can be expected naer the interface. As before, by the choice of $w(r)$, the initial bulk and surface concentrations satisfy the boundary condition Eq. (93) at the interface $r = r_0$ because of $w(r_0) = w'(r_0) = 0$. Other dimensionless numbers are $\lambda = 1, S_a = 3, S_d = 1, Pe = 10, Pe_s = 100, Re = 10, Ca = 4/3$, and $El = 0.5$.

As in previous test, we first perform four different computations by varying grid number $N = 64, 128, 256, 512$ with the associated mesh width $h = 2/N$. The Lagrangian

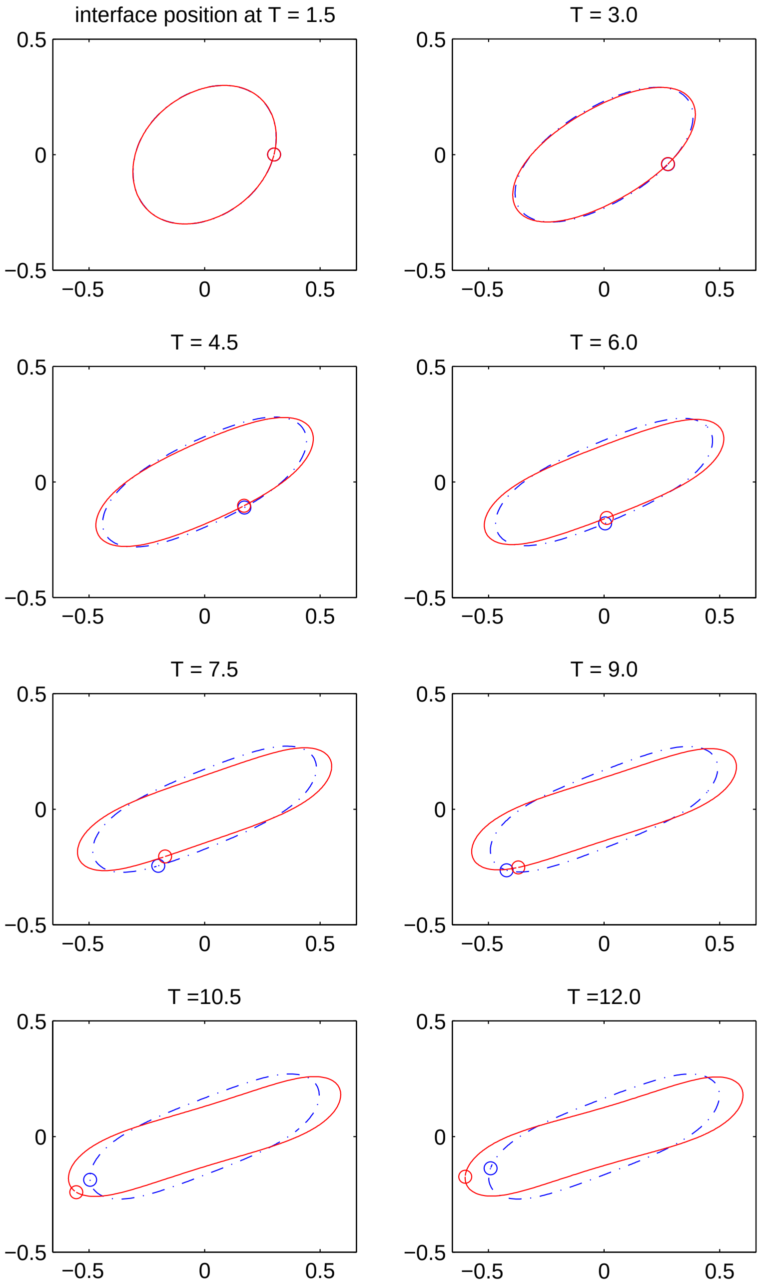

Figure 9.9: The comparison of clean (denoted by ”-.”) and soluble (denoted by ”-”) interfacial flows for a drop under shear flow.

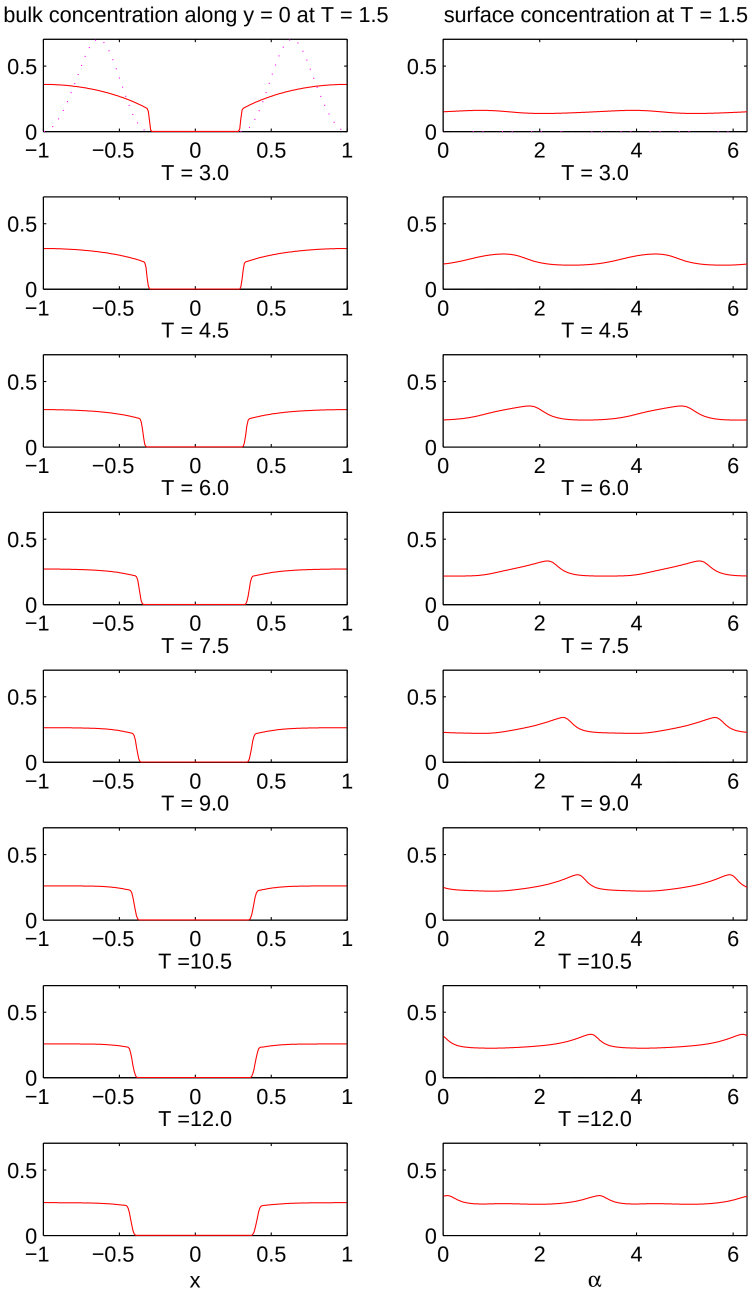

Figure 9.10: Left: the bulk concentration plots along the horizontal line $y = 0$. The dashed line in the first plot denotes the initial bulk concentration. Right: the surface concentration along the interface in counter-clockwise way starting from the point marked by ”o”.

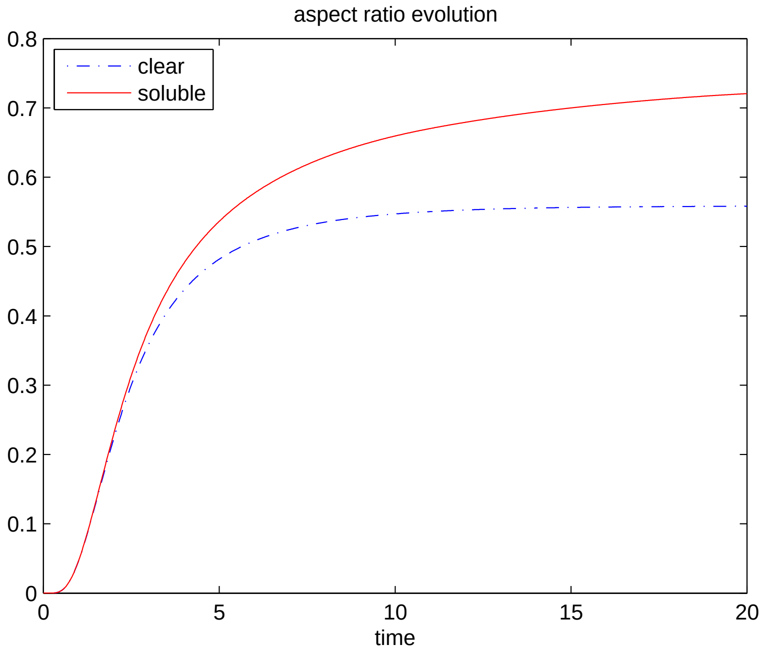

Figure 9.11: The comparison of aspect ratio between clean (denoted by ”-.”) and soluble (denoted by ”-”) cases.

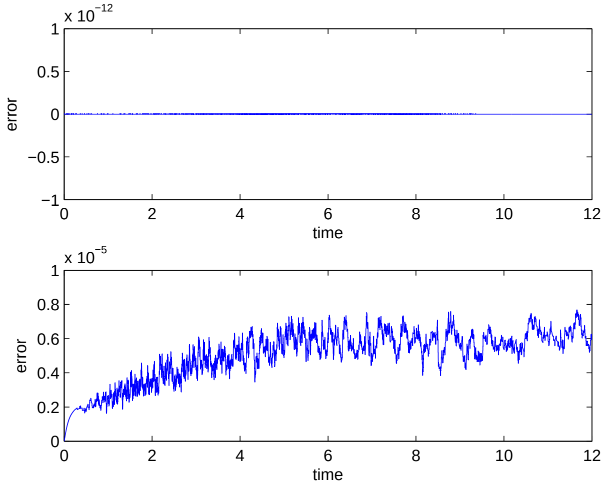

Figure 9.12: Upper panel: Time evolutionary plot of total mass relative error. Lower panel: Time evolutionary plot of leaking mass relative error inside the interface.

$N \times N$	$\|(HC)_{2N} - (HC)_N\|_2$	rate	$\|\Gamma_{2N} - \Gamma_N\|_2$	rate
64×64	6.2645E-03	–	1.1654E-03	–
128×128	3.8501E-03	0.7022	3.9683E-04	1.5542
256×256	2.3775E-03	0.6954	1.2670E-04	1.6471

$N \times N$	$\|u_{2N} - u_N\|_2$	rate	$\|v_{2N} - v_N\|_2$	rate
64×64	5.8396E-04	–	3.7335E-04	–
128×128	2.7426E-04	1.0903	1.8524E-04	1.0111
256×256	1.4308E-04	0.9386	9.1926E-05	1.0109

Table 9.6: The L_2 errors and their convergent rates for the bulk and surface surfactant concentrations, and the fluid velocity field at $T = 0.5$.

marker width is chosen as $\Delta\alpha \approx h/2$ and the time step size is $dt = h/8$. Table 9.6 shows the mesh refinement analysis of the bulk and surface concentrations, and the velocity field at $T = 0.5$. One can see that again the rate of convergence behaves like first-order in general.

Figure 9.9 shows the evolutionary interface positions of clean (denoted by dash-dotted line) and soluble surfactant (denoted by solid line) cases for a drop under shear flow based on the results of grid number $N = 256$. The clean drop bears no surfactant along the interface throughout the evolution so no bulk and surface surfactant equations are needed to be solved and the surface tension remains to be a constant $\sigma = 1$. (Note that, we use the clean drop as a comparison simply because of zero initial surface concentration is chosen in present setting.)

Due to shear stresses, both drops will be elongated and gradually aligned with the flow directions. For the soluble case, the interface will start to absorb the bulk surfactant so the bulk concentration decreases while the surface concentration increases in the beginning, see Fig. 9.10 in detail. Later, both absorption and desorption processes become more balanced so the bulk and surface concentrations become quite steady. As expected, the largest surface concentration appears to occur at the drop tips after the drop aligned with the flow. The drop with soluble surfactant has smaller surface tension than the clean drop so the deformation tends to be larger. One can see from Fig. 9.9 that the clean drop approaches to a steady state shape after $T = 9.0$ while the soluble surfactant drop continues to deform slightly afterwards.

By using the aspect ratio, we can verify if the deformation of drops attends to a steady state more seriously. Figure 9.11 shows the aspect ratio comparison between the soluble case and the clean one, where the ratio is defined as

$$\frac{L_M - L_m}{L_M + L_m}, \tag{151}$$

which L_M is the major radius (about the furthest distance of the interface to the origin), and L_m is the minor radius (about the shortest distance of the interface to the origin). One can see the aspect ratio of the clean drop is almost fixed as time large enough, while that in the soluble case is still deforming.

Figure 9.12 shows the total mass error and the mass leaking of the soluble case under the shear flow. The conservation of the mass of the surfactant is good, while the mass leaking is less than 0.001%. Our numerical results are physically reasonable and qualitatively consistent with those obtained in other literature such as in [41].

Chapter 10

Conclusion and future work

In the first part of this thesis, we discuss the convergence of Poisson equations with source terms defined on embedded interface in the computational domain. We provide one-dimensional proof and two-dimensional numerical tests to judge the results. For the source terms as derivatives of delta functions, such as pressure problem in Stokes equations, or indicator function in front tracking methods, the overall accuracy is first-order accurate in L^1 norm, half-order accurate in L^2 norm, but has $O(1)$ error in L^∞ norm. For the singular source as delta functions, the overall convergent rate is second-order accurate in L^1 norm, one and half-order accurate in L^2 norm, and first-order accurate in L^∞ norm. We also give some applications to solve second-order elliptic equations with piecewise-constant coefficients or Stokes problems by using the solution of Poisson equations we obtained.

In the second part of this thesis, we consider the surfactant, an amphiphilic molecular, in the multi-phase fluids. Due to the particle structure, it usually favor the presence in the fluid interface. We take solubility of the surfactant in one subdivision of the domain into account, and discuss the interactions between bulk domain and interface such as adsorption and desorption. These form a coupled surface-bulk interaction system of convection-diffusion equations. In order to reduce difficulties in the calculations, we rewrite the bulk concentration equation into a regular domain by using the indicator function introduced in first part. The concentration flux across the interface is treated as a singular source term in the equation. Based on immersed boundary formulation, we propose a numerical scheme to solve this coupled surface-bulk concentration equations with providing the conservation of total surfactant mass. We use a series of examples to validate the proposed scheme, and combine with Navier-Stokes solver to extend our previous works.

In the present thesis, all studies are done in one-dimension or two-dimension, we will try to expand our work into three-dimensional cases in the future. The challenges are much harder, for instance, how to set a good grid on the complex surface? how to modify the grid when it has large deformation, especially under the flow? how to solve convection-diffusion equations on this grid? and how to maintain the mass conservation property in the computation? Such problems are the major issues that we need to conquer.

Bibliography

[1] S. Adami, X. Y. Hu, N. A. Adams, A conservative SPH method for surfactant dynamics, J. Comput. Phys., 229 (2010), 1909–1926.

[2] D. Adalsteinsson, J. Sethian, Transport and diffusion of material quantities on propagating interfaces via level set methods, J. Comput. Phys., 185 (2003), 271–288.

[3] J. Adams, P. Swarztrauber, R. Sweet, Fishpack - A package of Fortran subprograms for the solution of separable elliptic partial differential equations, 1980. Available in http://www.netlib.org/fishpack.

[4] R. P. Beyer, R. J. LeVeque, Analysis of a one-dimensional model for the immersed boundary method, SIAM J. Numer. Anal., 29 (1992), 332–364.

[5] J. T. Beale, A. T. Layton, On the accuracy of finite difference methods for elliptic problems with interfaces, Commun. Appl. Math. Comput. Sci., 1 (2006) 91–119

[6] M. R. Booty, M. Siegel, A hybrid numerical method for interfacial fluid flow with soluble surfactant, J. Comput. Phys., 229 (2010), 3864–3883.

[7] M. Burger, Numerical simulation of anisotropic surface diffusion with curvature-dependent energy, J. Comput. Phys., 203 (2005), 602–625.

[8] E. Bänsch, P. Morin, R. H. Nochetto, A finite element method for surface diffusion: the parametric case, J. Comput. Phys., 203 (2005), 321–343.

[9] M. Bertalmio, L.-T. Cheng, S. J. Osher, G. Sapiro, Variational problems and partial differential equations on implicit surfaces, J. Comput. Phys., 174 (2001), 759–780.

[10] A. J. Chorin, Numerical Solution of the Navier-Stokes Equations, Math. Comp., 22 (1968), 745–762.

[11] C. A. J. Fletcher, Computational techniques for fluid dynamics: fundamental and general techniques, Springer-Verlag, 1991.

[12] K.-Y. Chen, K.-A. Feng, Y. Kim, M.-C. Lai, A note on pressure accuracy in immersed boundary method for Stokes flow, J. Comput. Phys., 230 (2011), 4377–4383.

[13] K.-Y. Chen, M.-C. Lai, A conservative scheme for solving coupled surface-bulk convection-diffusion equations with an application to interfacial flows with soluble surfactant, J. Comput. Phys., 257 (2014), 1–18.

[14] R. Cortez, The method of regularized Stokeslets, SIAM J. Sci. Comput., 23 (2001), 1204–1225.

[15] G. Dziuk, C. M. Elliott, Finite element on evolving surfaces, IMA J. Numer. Anal., 27 (2007), 262–292.

[16] G. Dziuk, C. M. Elliott, Surface finite elements for parabolic equations, J. Comput. Math., 25 (2007), 385–407.

[17] C. M. Elliott, B. Stinner, V. Styles, R. Welford, Numerical computation of advection and diffusion on evolving diffuse interfaces, IMA J. Numer. Anal., 31 (2011), 786–812.

[18] H. A. Stone, A simple derivation of the time-dependent convective-diffusion equation for surfactant transport along a deforming interface, Phys. Fluids A, 2, (1990), 111–112.

[19] F. H. Harlow, J. E. Welsh, Numerical calculation of time-dependent viscous incompressible flow of fluid with a free surface, Phys. Fluids, 8 (1965), 2181–2189.

[20] S. Khatri, A.-K. Tornberg, A numerical method for two phase flows with insoluble surfactant, Computers & Fluids, 49 (2011), 150–165.

[21] Z. Li, K. Ito, The Immersed Interface Method, SIAM, 2006.

[22] R. J. LeVeque, Z. Li, The immersed interface method for elliptic equations with discontinuous coefficients and singular sources, SIAM J. Numer. Anal., 31 (1994), 1019–1044.

[23] M.-C. Lai, H.-C. Tseng, A simple implementation of the immersed interface methods for Stokes flows with singular forces, Computers & Fluids, 37 (2008), 99–106.

[24] M.-C. Lai, Y.-H. Tseng, H. Huang, An immersed boundary method for interfacial flows with insoluble surfactant, J. Comput. Phys., 227 (2008), 7279–7293.

[25] M.-C. Lai, Y.-H. Tseng, H. Huang, Numerical simulation of moving contact lines with surfactant by immersed boundary method, Commun. Comput. Phys., 8 (2010), 735–757.

[26] M.-C. Lai, C.-Y. Huang, Y.-M. Huang, Simulating the axisymmetric interfacial flows with insoluble surfactant by immersed boundary method, International Journal of Numerical Analysis and Modeling, 8 (2011), 105-117.

[27] S. Leung, J. S. Lowengrub, H.-K. Zhao, A grid based particle method for high order geometrical motions and local inextensible flows, J. Comput. Phys., 230 (2011), 2540–2561.

[28] M. Muradoglu, G. Tryggvason, A front-tracking method for computation of interfacial flows with soluble surfactants, J. Comput. Phys., 227 (2008), 2238–2262.

[29] Y. Mori, Convergence proof of the velocity field for a Stokes flow immersed boundary method, Communications on Pure and Applied Mathematics, 61 (2008), 1213-1263.

[30] I. L. Novak, E. Gao, Y.-S. Choi, D. Resasco, J. C. Schaff, B. M. Slepchenko, Diffusion on a curved surface coupled to diffusion in the volume: Application to cell biology, J. Comput. Phys., 226 (2007), 1271–1290.

[31] C. S. Peskin, Numerical analysis of blood flow in the heart, J. Comput. Phys., 25 (1977), 220–252.

[32] C. S. Peskin, The immersed boundary method, Acta Numerica, 11 (2002), 479–517.

[33] R. Palaparthi, D. T. Papageorgiou, C. Maldarelli, Theory and experiments on the stagnant cap regime in the motion of spherical surfactant-laden bubbles, J. Fluid Mech., 559 (2006), 1–44.

[34] Y. Pawar, K. J. Stebe, Marangoni effects on drop deformation in an extensional flow: the role of surfactant physical chemistry, I. Insoluble surfactants, Phys. Fluids, 8 (1996), 1738–1751.

[35] A. Rätz, A. Voigt, PDE's on surfaces - A diffuse interface approach, Commun. Math. Sci., 4 (2006), 575–590.

[36] P. Schwartz, D. Adalsteinsson, P. Colella, A. P. Arkin, M. Onsum, Numerical computation of diffusion on a surface, PNAS, 102 (2005), 11151–11156.

[37] G. Tryggvason, B. Bunner, A. Esmaeeli, D. Juric, N. Al-Rawahi, W. Tauber, J. Han, S. Nas, Y.-J. Jan, A front-tracking method for the computations of multiphase flow, J. Comput. Phys., 169 (2001), 708–759.

[38] A.-K. Tornberg, B. Engquist, Numerical approximations of singular source terms in differential equations, J. Comput. Phys., 200 (2004), 462-V488.

[39] A.-K. Tornberg, R.W. Metcalfe, L.R. Scott, B. Bagheri, A front-tracking method for simulating fluid particle motion using high-order finite element methods, ASME Fluids Engineering Division Summer Meeting FEDSM97-3493, 1997.

[40] K. E. Teigen, X. Li, J. Lowengrub, F. Wang, A. Voigt, A diffuse-interface approach for modeling transport, diffusion and adsorption/desorption of material quantities on a deformation interface, Commun. Math. Sci. 7 (2009), 1009-1037.

[41] K. E. Teigen, P. Song, J. Lowengrub, A. Voigt, A diffuse-interface method for two-phase flows with soluble surfactants, J. Comput. Phys., 230 (2011), 375–393.

[42] S. O. Unverdi and G. Tryggvason, A front-tracking method for viscous incompressible multi-fluid flows, J. Comput. Phys., 100 (1992), 25–37.

[43] J.-J. Xu, H.-K. Zhao, An Eulerian formulation for solving partial differential equations along a moving interface, J. Sci. Comput., 19 (2003), 573–594.

[44] X. Yang, X. Zhang, Z. Li, G.-W. He, A Smoothing technique for discrete delta functions with application to immersed boundary method in moving boundary simulations, J. Comput. Phys., 228 (2009), 7821–7836.

[45] Y. N. Young, M. R. Booty, M. Sigel, J. Li, Influence of surfactant solubility on the deformation and breakup of a bubble or capillary jet in a viscous fluid, Phys. Fluids, 21 (2009), 072105.

[46] J. Zhang, D. M. Eckmann, P. S. Ayyaswany, A front tracking method for a deformable intravascular bubble in a tube with soluble surfactant transport, J. Comput. Phys., 214 (2006), 366–396.

[47] Y. C. Zhou, S. Zhao, M. Feig, G. W. Wei, High order matched interface and boundary method for elliptic equations with discontinuous coefficients and singular sources, J. Comput. Phys., 213 (2006), 1–30.